A STUDY ON SUSY SEARCH STRATEGIES IN THE CMS, HPD NOISE SPECTRUM AND ELECTRON RECONSTRUCTION EFFICIENCY

by

Mehmet Deliömeroğlu

B.S., Physics, Yildiz Technical University, 2001

M.S., Physics, Bogazici University, 2006

Submitted to the Institute for Graduate Studies in
Science and Engineering in partial fulfillment of
the requirements for the degree of
Doctor of Philosophy

Graduate Program in Physics

Boğaziçi University

2010

ACKNOWLEDGEMENTS

I would like to express my gratitude thanks to my thesis supervisor Professor Dr. Erhan Gülmez for his support during my research and for his great patience and valuable time he devoted to evaluate and read the drafts of my thesis. I would like to thank Professor Dr. Metin Arık, Serkant Çetin, Osman Teoman Turgut and Assistant Professor Dr. Özgül Kurtuluş their kindly reading and evaluating my thesis.

My deepest appreciation to my beloved wife, and my family for their support.

I also thank Anwar Bhatti, Kalanand Mishra, Shuichi Kunori, and Sarah Eno for their kind and supportive guidance through out the analyses. I also would like to thank Fermilab LPC coordinators and Fermilab in general for their financial support during my stay at Fermilab.

This work was partially supported by Turkish Atomic Energy Authority (TAEK) and Boğaziçi University Scientific and Technological Research Fund (09B302P).

ABSTRACT

A STUDY ON SUSY SEARCH STRATEGIES IN THE CMS, HPD NOISE SPECTRUM AND ELECTRON RECONSTRUCTION EFFICIENCY

The hybrid photo diodes in the HCAL will play an important role in detection of the jets and missing energy. It is very important to understand and monitor their charge spectrum. The charge spectrum of the HPD detectors in the HB and HE with high statistics and their *noise* rate have been studied. In this study a method to monitor the HPD charge spectrum was developed.

The relation between jets and electron reconstruction efficiency is quite important. The jets in the events may effect the reconstruction efficiency and quality of the electron reconstruction. The analysis showed that for each increase in the number of jets the efficiency of electrons decrease by about 1-7%.

SUSY is a symmetry relating the standard model particles to their superpartners. It must be a broken symmetry since no supersymmetric particle has been observed yet. A constrained model of SUSY breaking, mSUGRA predicts experimental signals in the CMS detector for detecting the evidence for SUSY. One of these, dielectron with large missing energy and jets is studied with MC simulation. It is shown that SUSY can be discovered with 1 fb^{-1} data at $\sqrt{s} = 10$ TeV. Different clustering algorithms for the jets and missing energy are used and compared for the best result.

ÖZET

CMS DEDEKTÖRÜNDE SUSY ARAŞTIRMA STRATEJİSİ, HPD YÜK SPEKTRUMU VE ELEKTRONLARIN TESBİT EDİLME VERİMLİLİĞİ ÜZERİNE BİR ÇALIŞMA

Hadronik kalorimetredeki hibrid foto diyotlar (HPD) jetlerin ve kayıp enerjinin tesbit edilmesinde önemli rol oynayacaklardır. Yük spektrumlarının incelenmesi ve izlenmesi önemlidir. HPD'lerin yük spektrumlari ve gürültü oranları incelenmiştir. Bu çalışma sonucunda HPD yük spektrumunu yüksek sayıda istatistik ile izlemek için kullanılabilecek bir yöntem geliştirilmiştir.

Elektronların jetlerle birlikte tesbit edilmesinin verimliliği oldukça önemlidir. Özellikle demet çarpışmalarının enerjileri arttıkca üretilen jet sayısı ve aradaki bağlantı artmaktadır. Kaydedilen fizik olaylarındaki jetler elektronların tesbit edilme verimliliğini ve kalitesini olumsuz yönde etkiler. Bu konuda yapılan çözümlemeler sonucunda jet sayısındaki her bir artışın elektronların tesbit edilme verimliliğinde %1-7 arasında azaldiği gözlemlenmiştir.

"Süpersimetri" standart model parçacıklarına simetrik olan yeni parçacıklar öngören bir teoridir. Ancak şimdiye dek süpersimetrik parçaçıklar gözlemlenemediği için süpersimetri kırık bir simetri olmalıdır. Süpersimetri kırılmasının kısıtlı bir modeli olan "mimimal süper kütle çekimi" (mSUGRA) süpersimetri varlığının tesbiti için CMS dedektörü içinde deneysel gözlenebilir sinyaller öngörmektedir. Bu deneysel sinyallerden bir tanesi, iki-elektron ile birlikte büyük miktarda kayıp enerji ve jetlerden oluşmaktadır. Bu sinyal MC simülasyonu kullanılarak incelenmiştir. Bu çalışma süpersimetrinin $\sqrt{s} = 10$ TeV ve 1 fb^{-1} koşullarında gözlenebileceğini göstermiştir. Ayrıca bu çalışmada farklı jet ve kayıp enerji bulma algoritmaları karşılaştırılmıştır.

TABLE OF CONTENTS

LIST OF FIGURES

LIST OF TABLES

LIST OF SYMBOLS/ABBREVIATIONS

E_T	Energy in the transverse plane
E_{had}	Energy in the hadronic calorimeter
E_{em}	Energy in the electromagnetic calorimeter
E_T	Energy in the transverse plane
P	Momentum in the transverse plane
η	Pseudorapidity
ϕ	Azimuthal angle
θ	Horizontal angle
σ	Cross section
ϵ	Efficiency
$\mathcal{L}$	Integrated luminosity
$\sqrt{s}$	Center of mass energy
ADC	Analog to digital converter
ALCT	Anode local charged track
APD	Avalanche photodiodes
ASIC	Application-specific integrated circuit
ATLAS	A Toroidal LHC apparatus
BSM	Beyond the standard model
BTI	Bunch crossing and track identifier
CALOMET	Calorimeter missing transverse energy
CCA	channel control application-specific integrated circuit
CDB	Condition database
CLCT	Cathode local charged track
CMS	Compact Muon Solenoid
CMSSW	Compact muon solenoid software
CRAFT	Cosmic run At four tesla
CSCTF	Cathode strip chamber track finder

DAQ	Data acquisition
DCC	Data connector card
DCS	Detector control system
DTTF	Drift tube trigger track finder
EB	Electromagnetic barrel calorimeter
ECAL	Electromagnetic calorimeter
EE	Electromagnetic endcap calorimeter
ESS	Electromagnetic calorimeter safety system
FDL	Final decision logic
FE	Front end board
FED	Front end drivers
FPGA	Field-programmable gate array
FRL	Front end read-out link
GCT	Global calorimeter trigger
GOH	Gigabit optical hybrid
GSF	Gaussian-sum filter
GTL	Global trigger logic
GUT	Grand unification theory
HB	Hadron barrel calorimeter
HBM	Hadron barrel minus calorimeter
HBP	Hadron barrel plus calorimeter
HCAL	Hadron calorimeter
HE	Hadron endcap calorimeter
HF	Hadron forward calorimeter
HLT	High level trigger
HM	Higgs mass, High mass
HO	Hadron outer calorimeter
HPD	Hybrid photodiodes
HTR	Hadron calorimeter trigger read-out
HV	High voltage
ICONE	Iterative cone

ID	Identity
JES	Jet energy scale
L1	Level 1 trigger
L1A	Level 1 trigger accept
LED	Light-emitting diode
LHC	Large hadron collider
LM	Low mass
LSP	Lightest supersymmetric particle
LVR	Low voltage regulator
MC	Monte Carlo simulation
MET	Missing transverse energy
MHT	Missing HT
MIP	Minimum ionizing particle
MPGA	Multi gain pre-amplifier
MSSM	Minimal supersymmetric standard model
mSUGRA	Minimal super gravity
ODU	Optical decoder unit
PAT	Physics analysis toolkit
PMT	Photo multiplier unit
PTM	Precision temperature monitoring
PYTHIA	Particle generator
QCD	Quantum chromodynamics
QIE	Charge-integrator and encoder
RBX	Read-out box
RCT	Regional calorimeter trigger
ROOT	Data analysis framework
RPC	Resistive plate chambers
R-parity	Matter parity
SC	Super cluster
SiPM	Silicon photo multiplier
SISCone	Seedless interfaced-safe cone

SL	Super layer
SM	Standard model
Sparticle	Supersymmetric particle
SRP	Selective read-out processor
SUSY	Supersymmetry
TCC	Trigger concentrator card
TCS	Trigger control system
TPG	Trigger primitive generator
TRACO	Track correlator
TRB	Trigger board
TS	Time slice
TTS	Trigger throttle system
VFE	Very front end
VPT	Vacuum phototriodes
WLS	Wavelength shifting

1. INTRODUCTION

It has been about six months since the Large Hadron Collider (LHC) started to collide proton-proton beams with a center of mass energy of $\sqrt{s} = 7$ TeV. However, it is still too early to search for the physics beyond the Standard Model (SM) due to very low luminosity. Nevertheless, the exciting times for scientist from all around the world has started.

The compact muon solenoid is one of the biggest detectors in the LHC. It is a very large advanced detector not only technologically but also with a very large world wide collaboration. It is designed as a multi purpose detector to study the physics in and beyond the SM, e.g. supersymmetry (SUSY). Theoretical physicist started to build the theory since the beginning of the 1970s. The experimental search for the SUSY has first started with the Large Electron-Positron Collider (LEP) at CERN and continue for the last two decades with the Tevatron at Fermilab. No direct evidence of SUSY has been achieved yet but the potential is very high with the LHC.

In this thesis, there are three individual analyses, different in their own concept but related with the same ultimate goal of the "Search for SUSY". The charge-noise spectrum of the hybrid photo-diodes are studied since they are an important part of the hadronic calorimeter (HCAL) and the HCAL is very important for jets and missing energy detection. It is expected that the lepton reconstruction efficiency will be effected by the jets. Therefore, the electron reconstruction efficiency as a function of the jet multiplicity and distance to jets is studied in details. The final analysis is the SUSY search with the dielectron plus jets plus missing transverse energy in the final state.

The first chapter will cover the detailed description of the compact muon solenoid detector including its important subsystems, hardware and electronics. Algorithms for the reconstruction of the physical objects, leptons, jets, and missing energy will be covered in the second chapter. The third chapter will deal with the details and results for the HPD analysis, while the fourth chapter will cover the details of the electron

efficiency study. An introduction to the SUSY theory will be given in chapter four. This chapter will describe the theory in a limited way that is appropriate for the CMS. The final chapter will give the details and the results of the SUSY search analysis in the CMS at $\sqrt{s} = 10$ TeV.

2. COMPACT MUON SOLENOID (CMS)

2.1. Overview

The CMS [1] is a multi-purpose particle physics detector built to operate on the Large Hadron Collider (LHC) which is a proton-proton colliding machine at CERN. It is located at about 100 meters underground in Cessy, France. The LHC is constructed in the 27-km long and 50-175 meters underground LEP tunnel in Geneva, Switzerland. The total budget of LHC is around $9 billion.

The LHC is built with the aim of testing the predictions of the Standard Model (SM), as well as the physics Beyond the Standard Model (BSM) at the TeV scale, for instance, existence of Higgs mechanism, the supersymmetric partners of SM particles predicted by Supersymmetry (SUSY), or the extra dimensions (ED). The LHC will also collide heavy ions for studying heavy ions collisions.

The LHC had started to circulate the first proton beams on September 10, 2008. Unfortunately after 10 days, it was shut down due to a serious explosion in sector 3-4. After repairs were done, the first proton-proton collisions started in late November 2009. For the time being LHC operates at half the design energy, $\sqrt{s} = 7$ TeV, with low luminosity.

The LHC will provide proton beams at 7 TeV, hence $\sqrt{s} = 14$ TeV with a design luminosity of $\int \mathcal{L} = 10^{34} cm^{-2} s^{-1}$. At these design parameters, the total cross section of proton-proton collisions is $\sigma_{total} \cong 110$ mb, while the inelastic cross section is $\sigma_{inel} \cong 60$ mb. The proton bunches has 25 ns spacing but there are also gaps in LHC beam which contains a total of 3563 bunches and 2808 of them have protons. In one second a beam circulates the LHC ring 11245 times that yields an approximately 30 MHz crossing rate. Since 20 proton-proton collisions are expected per crossing, that means 6x10^8 inelastic collisions per second. However it is not possible to store such a huge number of events that would be produced in so many collisions, therefore a very good trigger

system is required to select one event of interest in every 6 million events to reduce the event rate to 100 event per second. Considering that thousands of particles coming out of interaction region every 25 ns, the pile-up effects will be very important when trying to select the particles coming from the desired interactions. It is necessary to have a detector with large number of channels and a good time resolution. The CMS detector has been designed and constructed to operate at these conditions.

The main characteristics of CMS [2] could be defined as

- A high-field (3.8 T) solenoid to provide bending for momentum measurement of energetic particles and charged particle identification.
- Muon detectors that have high momentum and mass resolution with good charge identification for muons.
- Tracker with silicon-based inner system to provide good charged particle momentum resolution and reconstruction efficiency.
- Electromagnetic calorimeter constructed from high quality scintillating crystals to ensure very good electromagnetic resolution ($\leq 1\%$).
- Hadronic calorimeter system with large hermeticity.

The coordinate system in CMS is chosen such that the beam direction is represented by z axis while y axis is pointed upward and x axis is pointed inward to the center of the LHC ring. Consequently, the energy and the momentum transverse to the beam direction can be calculated from x and y components. θ and ϕ angles are the polar and azimuthal angles, respectively. Pseudorapidity is given by

$$\eta = -\ln tan(\theta/2). \tag{2.1}$$

Figure 2.1 shows complete CMS detector layout with sub-detector systems and the size relative to an average human being. The CMS detector has the length of 2160

cm with the diameter of 1460 cm. It weighs more than 125x10^5 kg. The details for the sub-systems of the CMS will be described in the following sections.

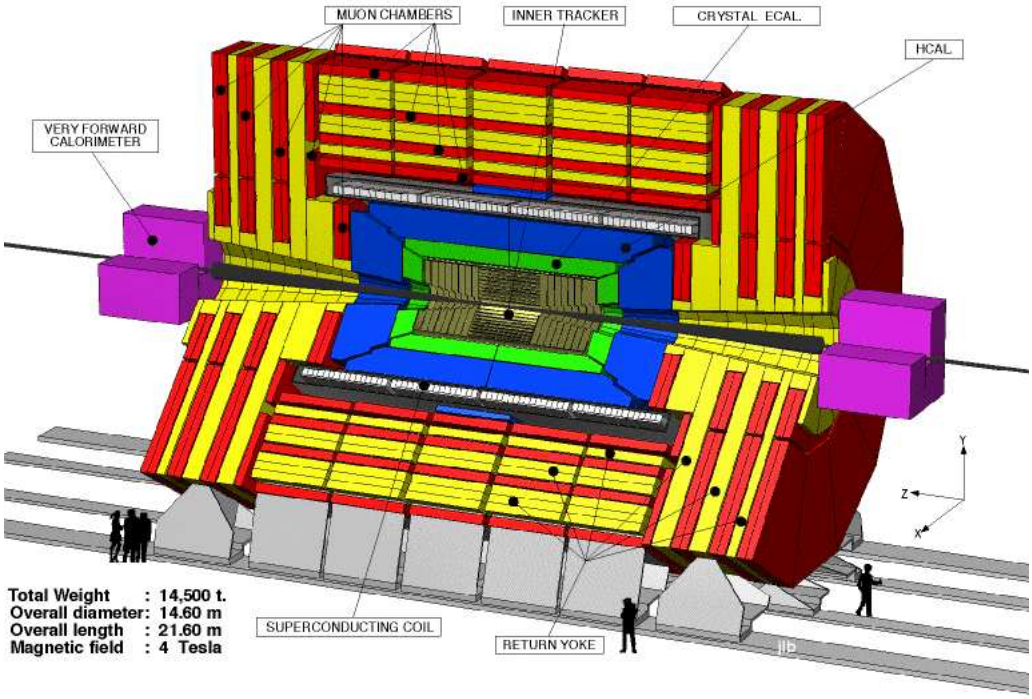

Figure 2.1. The layout of CMS detector

2.2. Tracker

The CMS tracker [3] has been designed to provide a precise measurement of trajectories of charged particles. It is entirely built with silicon sensors to operate at high-radiation environment due to high LHC design luminosity with high granularity and speed. The tracker system was built as two components; a pixel detector with radii up to 10.2 cm and a silicon-strip detector extending to 1.1 m radii. The CMS tracker is the largest silicon tracker built so far.

A requirement for the LHC physics is a very accurate reconstruction of the trajectory of the charged particles with transverse momentum, p_T, greater than 1 GeV in the region of pseudorapidity, η, up to 2.5. The tracker provides good identification and trajectory reconstruction for electrons and muons by combining the information from electromagnetic calorimeter and muon detectors, respectively. The resolution and

efficiency requirements for reconstruction of jets, which result from the fragmentation of quarks, gluons, and heavy particles, could be met with high precision particle tracks provided by the tracker. It also plays an important role to reduce the event rate from 40 MHz to 100 Hz by supplying accurate track information to trigger system.

Figure 2.2 gives a schematic cross sectional drawing of tracker system. The radial region from $\sim$ 0 mm to 200 is covered by 6.6x10^7 pixels of the pixel detector. Immediately after the pixel detector, the silicon strip detector starts and extends the radial region coverage up to 1200 mm.

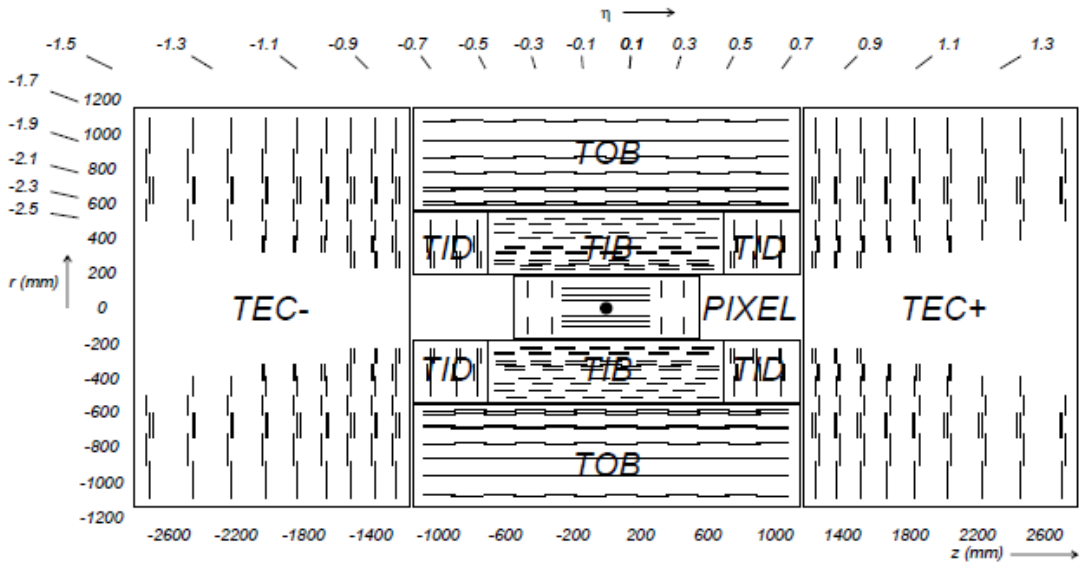

Figure 2.2. The schematic drawing of the CMS tracker. Each line corresponds to a detector cell, while double lines show back-to-back cells.

The pixel detector is the closest part of the tracking system to the interaction region. The pseudorapidity coverage of the pixel detector is up to 2.5 ($|\eta| < 2.5$), shown in Figure 2.3. The pixel tracker is essential to form seed tracks for outer track reconstruction and high level trigger. The pixel detector is constructed as two endcap disks and three barrel layers and arranged such that for the full *eta*-range it is possible to collect three tracking hits. The pixel detector is capable of providing 15-20 μm resolution.

At full LHC luminosity the innermost layer of the pixel detector is expected to be operational for 2 years.

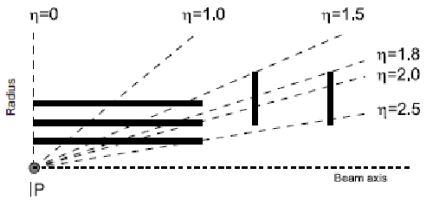

Figure 2.3. η coverage of the pixel tracker.

The CMS Silicon Strip Tracker is the largest silicon tracker ever built. It is made with four sub-systems, the inner barrel, the outer barrel, the inner disk, and end caps. The longitudinal layout of one quarter of the silicon strip detector is shown in Figure 2.4.

The inner barrel is composed of four cylinders placed at different radii from 255.0 mm to 498.0 mm and has a total length of 1400 mm. The inner disk consists of three disks. The outer disk has only one single layer. The end caps consist of nine disks on each side with two of them providing back and front hit information. The end cap disks has radii from 220 mm to 1135 mm and lengths from 124 mm to 2800 mm at each side.

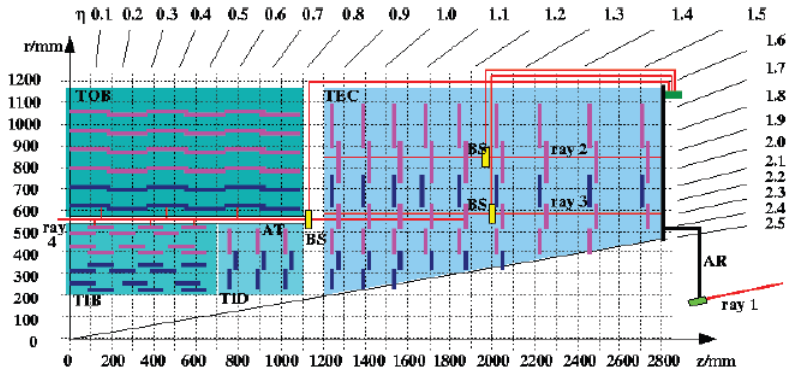

Figure 2.4. The silicon strip tracker layout.

The entire silicon strip detector is made of silicon sensors as the rest of the CMS tracker. Figure 2.5 shows a picture of the silicon sensors assembled in a layer of silicon strip tracker. The sensors are produced by two companies, Hamamatsu Photonics

K.K. (Hamamatsu-City, Japan), ST Microelectronics (Catania, Italy) and tested at five centers. 15 different sensor geometries are required to cover all regions in the CMS tracker.

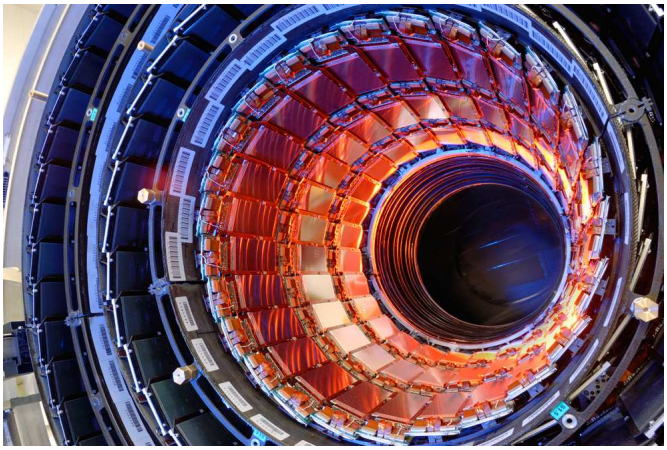

Figure 2.5. Picture of the assembled silicon sensors of the CMS tracker.

2.3. Electromagnetic Calorimeter

The CMS electromagnetic calorimeter(ECAL) [4] is a hermetic homogeneous calorimeter. The ECAL is situated within the magnet and the hadronic calorimeter. It is composed of over 75000 lead tungstate ($PbWO_4$) crystals. The reason for choosing the lead tungstate crystals is the need for optically clear, fast, and radiation resistive material. The crystals emit more than 80% of the light in just 25 ns which is the LHC bunch crossing time. It has a low light output depending on the temperature of the crystal. The crystals needed to be polished to achieve the total internal reflection to improve the light collection on the photodetectors. The end caps have more uniform light collection due to the geometric advantage that the crystal faces are more parallel compared to the barrels. A preshower detector is placed in front of the endcap crystals.

2.3.1. ECAL Layout and Material Used

The layout of the CMS electromagnetic calorimeter is shown in Figure 2.6. The electromagnetic detector is constructed as two barrels and two end caps covering pseudorapidity, η, up to 3.0 to ensure maximum hermeticity.

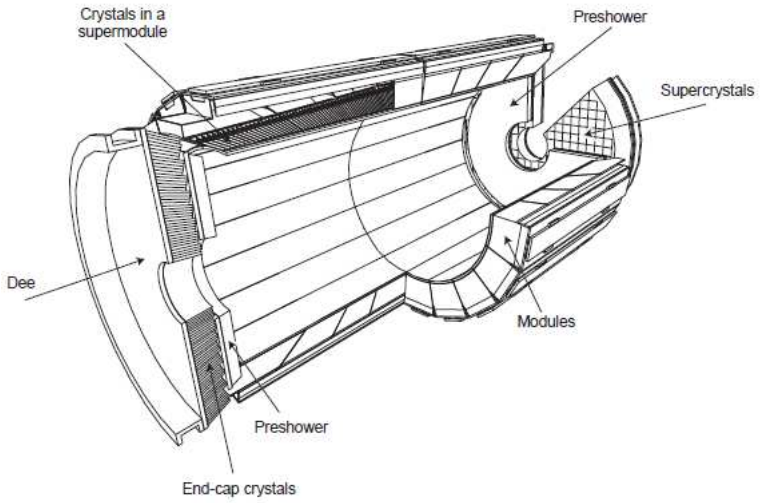

Figure 2.6. The layout of ECAL with the preshower detector.

The ECAL barrels cover $-1.479 < \eta < 1.479$ region. It consists of 61200 crystals with varying shape due to η positioning. The length of the crystals is 23 cm which is roughly 26 X_0, where X_0 represents the radiation length. The cross section of the crystals are 26x26 mm^2 at the rear and 22x22 mm^2 at the front. The crystal weight of the barrel is 67.4 t with a volume of 8.14 m^3 yielding a density of 8.3 t/m^3. It has an inner radius of 124 cm. A submodule is composed of crystals covered by a thin (0.1 mm), aluminum layer box. The distance between crystals in a submodule is about 0.35 mm while between submodules is about 0.5 mm. The submodules are placed into different types of modules according to η positioning, containing a total of 400-500 crystals. Total of 1700 crystals in four modules compose a super module. A super module covers a region of $\phi = 20^o$ so that there is a total of 36 super modules, 18 for the electromagnetic calorimeter barrels on each side. A picture of the ECAL barrel placed inside the hadronic barrel calorimeter is shown in Figure 2.7(a).

In the barrel avalanche photodiodes (APD) are used as photodetectors. They are required to be fast, radiation resistive and capable of working in high magnetic field (3.8T). Since the light emission of crystals are not high, they should be able to operate with a high gain of 50 while being insensitive to particles passing through them. The APD gain depends on the bias voltage and to ensure a good energy resolution the stability of the power supply is important. The APD requires 340-430 V to operate at

a gain factor of 50.

The ECAL endcaps (EE) are located at a distance of 3154 mm from the interaction point on each side. The endcaps extend the η coverage of the ECAL up to 3.0 with their own range of $1.479 < |\eta| < 3.0$. The crystals in the EE are shaped identically and composed of in units of 5x5 crystals also called supercrystals or superclusters (SC). Each endcap has two disks and each disk holding 3662 crystals in total of 156 SCs. The SCs are positioned such that to point 13 m beyond the interaction point. The crystals in the endcaps have a length of 24.5 X_0 or 220 mm. The front face cross section of the crystals is 28.6x28.6 mm^2 and the rear face cross section is 30x30 mm^2. The total crystal weight of the EE is 24.0 t with a volume of 2.90 m^3. A picture of a half disk of the EE is shown in Figure 2.7(b).

The magnetic field configuration and the expected level of radiation variation at the endcap region force to choose vacuum phototriodes (VPT) as photodetectors in the endcaps. They are designed especially for CMS use. To operate in the nominal 4-T magnetic field they have 10 μm thick copper mesh anode. They can operate with a gain of 10 at zero-magnetic field and the gain might be reduced as much as 10% in the presence of 4-T magnetic field. They need to operate with their photocathode grounded, the anode at +800 V, and the dynode at +600 V.

The stability of the temperature is very important due to fact that both the photon emission of the crystals and the amplification of the photodetectors depend on temperature. The optimal operating temperature of the ECAL is 18^oC and need to be kept stable within $\pm 0.05^oC$.

2.3.2. Preshower Detector

The major purpose of the construction of the preshower detector is to differentiate pions from photons. In addition, it improves electron and photon identification against minimum ionizing particles. The preshower is constructed as a sampling type calorimeter. The preshower detector covers a pseudorapidity region of $1.65 < |\eta| < 2.60$.

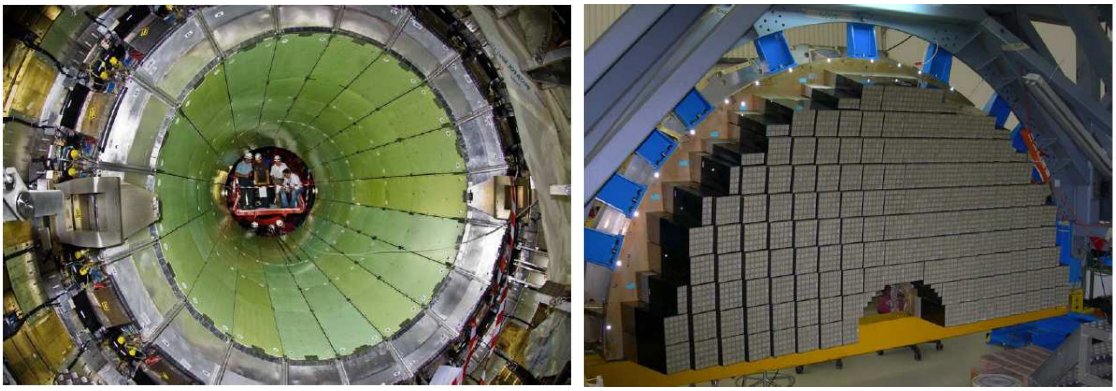

(a) EB (b) EE

Figure 2.7. The pictures of the ECAL barrel EB and endcaps EE.

Lead layer absorbers to start electromagnetic showers of electrons and photons are used at a thickness of $2X_o$. The layer of silicon sensors are placed after an additional lead layers of $1X_o$ to improve the shower energy collection efficiency. Hence the total travel distance before reaching the silicon sensors is $3X_o$ which ensures that 95% of the incoming electrons and photons start showering. There are a total of 4500 silicon detectors with 63x63 mm^2 in size. Each silicon detectors has 32 strips at a 2 mm thickness into which a MIP will deposit 3.6 fC charge.

A micromodule in the preshower detector is the combination of sensor, front-end electronics and support holding it. The micromodules are placed as groups of 7, 8, 9 on baseplates with electronic system called ladders. About 4300 micromodules are placed in 500 ladders. Figure 2.8 shows a picture of the completed preshower detector assembled in the EE.

2.3.3. Electronics

A complete trigger tower of the electromagnetic detector is composed of 5x5 crystals. The on-detector electronics has been designed to read signals from a trigger tower. The parts of it can be listed below;

- Five very front end boards (VFE).
- One front end board (FE).

Figure 2.8. A picture of the preshower detector.

- Eight gigabit optical hybrids (GOH), two for the EB and six for the EE.
- One low voltage regulator (LVR).

The signal amplification is performed by a multi gain pre-amplifier (MPGA) at gain values of 1, 6, and 12. To avoid signal saturation, signals are multiplied with these different gains and the non-saturated signal is sent as output to corresponding analog-to-digital converter by an integrated logic. The non-linearity of the output signal is expected to be <1%. The FE cards store the digitized data during the Level-1 trigger latency. The GOH is used to transmit trigger tower energy to the trigger concentrator card (TCC). A schematic figure of the ECAL on-detector electronics is shown in Figure 2.9.

The on-detector electronics, VFE and FE, are controlled by 40-MHz digital system called the off-detector clock and control system (CCS). The CCS is the part of the off-detector electronics system which gives out the LHC system clock, trigger commands, and configures the FE electronics.

The off-detector electronics is composed of CCS, TCC, data connector cards (DCC), and the selective read-out processor (SRP). As the schematic picture of the ECAL off-detector electronics is shown in Figure 2.10, it serves as both data acquisition (DAQ) and trigger system. The SRP system determines whether the data pass the

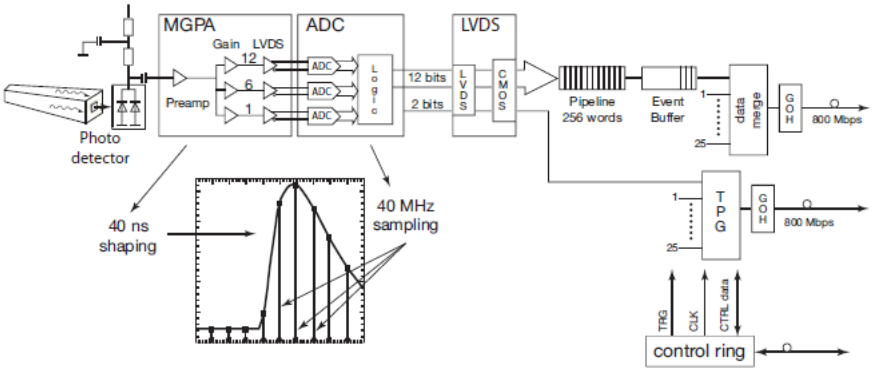

Figure 2.9. A schematic picture of the ECAL on-detector electronics showing signal-processing from APD to TCC.

required configuration by producing the selective read-out flag. It is used by the DCC to reduce the event rate. The DCC is also responsible for the read-out of the data. The trigger primitives which are initiated in the FE cards are finalized, and sent to the regional calorimeter trigger system (RCT) by the TCC.

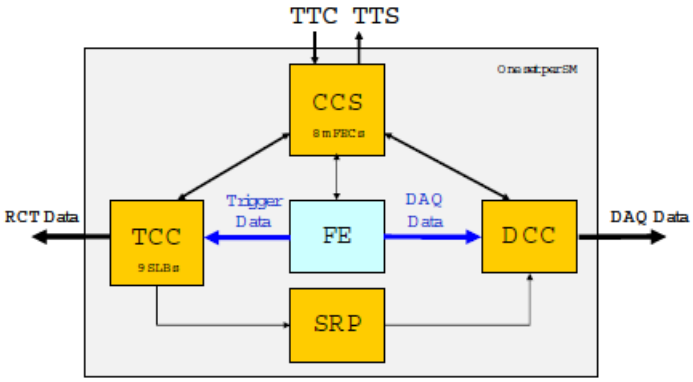

Figure 2.10. A schematic picture of the ECAL off-detector electronics.

The status of the ECAL is monitored by the detector control system (DCS) with the purpose of preventing any damage to the detector. The ECAL safety system (ESS) with the monitoring systems; precision temperature monitoring (PTM), humidity monitoring (HM), high voltage (HV) and low voltage (LV) forms the ECAL DCS.

2.3.4. Calibration and Energy Resolution

Calibration of the ECAL can be divided into two terms such that the energy scale, the global term, and the so called intercalibration, the channel-to-channel relative term. The intercalibration can be described as the accuracy of the channel response depending on the position in the ECAL and the time. In other words the data recorded at different location and/or on different time should be accurate and consistent with each other. Before the installation the detector is calibrated via the test beams, laboratory measurements, and cosmic data. After the installation, the calibration can be maintained with laser monitoring system which is used to measure the changes in the crystal transparency due to the radiation of the LHC environment.

The most important calibration precision will be provided by physics events called *in-situ* calibration. It is the major calibration tool to reduce the constant term in the energy resolution to the desired value of 0.5%. The decay channels $Z \rightarrow e^+e^-$, $Z \rightarrow \mu^+\mu^-$, and $W \rightarrow e\nu$ will be used for intercalibration of the ECAL channels.

The electromagnetic calorimeter is designed with the aim of providing high energy resolution, 0.5%, for photons and electrons above 100 GeV. This is desired for the ability to detect the decay of the Higgs boson into two photons.

For energies lower than $\sim$ 500 GeV the energy resolution can be parametrized as

$$\left(\frac{\sigma}{E}\right)^2 = \left(\frac{S}{\sqrt{E}}\right)^2 + \left(\frac{N}{E}\right)^2 + C^2, \tag{2.2}$$

where E is the energy, S is the stochastic term, N is the noise term and C is the constant term.

The stochastic term has three main contributions; the shower fluctuations from

event to event, photostatistics contribution, and energy deposition fluctuations in the preshower detector. The event-to-event shower fluctuations depend on the crystal size of the reconstructed energy which is 1.5% for 3x3 crystals and 2% for 5x5 crystals. The photostatistics contribution is expected to increase the stochastic term by 2.1%. The energy resolution of the preshower detector also contributes to the stochastic term with a value of $5\%/\sqrt{E(GeV)}$.

The contributions to the noise term are electronics, digitization, and pileup noise. The electronics and digitization noise, measured by the test beams, is $\sim$ 40 MeV/channel for channels in the barrel. The transverse energy equivalent of the noise in the end caps is measured to be roughly constant and around 50 MeV. Also neutron irradiation to the avalanche photodiodes (APDs) in the barrel causes current leakage contributing to the electronic noise. This contribution, depends on the luminosity and time, expected to be 30 MeV/channel after one year of operation at full LHC design luminosity. The signal shape from the preamplifier will extend over several LHC bunch crossings. The signal amplitude is reconstructed with multiple time slices. If additional particles reach the calorimeter overlapping with reconstructed time slices, pile up noise will happen. Its magnitude is expected to be small at low luminosities. However its contribution to the noise become significant at higher luminosities.

The constant term may be caused by calibration errors, energy leak from the back of the crystals, and non-uniformity of longitudinal light collection. The rear energy leakage effect is shown to be negligible by the test beam results.

2.4. Hadronic Calorimeter

The hadronic calorimeter (HCAL) [1] is specifically designed to measure jets coming from the hadronization of quarks, gluons and heavy particles and missing energy caused by the undetectable particles, e.g, neutrinos. It will also help the identification of leptons especially in forward regions. The hadron calorimeter has a total pseudorapidity coverage of $|\eta| < 5.2$ which is crucial for missing energy detection.

The HCAL is designed and constructed as a sampling calorimeter. It is composed of four sub detectors, the hadron barrel (HB), the hadron endcap (HE), the hadron outer (HO), and the hadron forward (HF) calorimeters. The HB, and HE are located in between the ECAL and the magnet while the HO sits between the magnet and the muon system. Due to the constraint of the space between the magnet and the ECAL it was not possible to put enough absorber to detect the tail of hadronic shower. Thus the HO is placed in the outer region of the magnet for completion. The cross section of the HCAL detector with the rest of the CMS is shown in Figure 2.11.

Figure 2.11. Cross section of the HCAL longitudinal view with the rest of the CMS. The HB, HE, HO, and HF locations are shown.

2.4.1. Barrel Calorimeter (HB)

The hadron barrel calorimeter is a sampling calorimeter with 50 mm thick brass absorber plates piled together with 4 mm thick scintillator leaves [5]. It is constructed as two half-barrels with a length of 4300 cm each and located at each side of the interaction point (HB+, HB-). The pseudorapidity coverage goes up to $|\eta| = 1.3$ for the HB. The hadron barrel calorimeter is a sampling calorimeter with 50 mm thick brass absorber plates piled together with 4 mm thick scintillator leafs [5]. It is constructed as two half-barrels with the length of 4300 cm each and located at each side of the interaction point (HB+, HB-). The pseudorapidity coverage goes up to $|\eta| = 1.3$ for the HB.

The total ϕ space is divided into slices of $\Delta\phi = 20^o$ and covered by individual wedges. There are a total of 36 wedges, 18 for HB+ and 18 for HB-, sitting parallel to the beam line. The absorber material (brass layers) has a density of 0.853 kg/m^3 and a radiation length of $X_o = 1.49$ cm. The numbering scheme of the wedges and a transverse plane view are shown in Figure 2.12. Inner width of the wedges is 670 mm while the outer width is 1004 mm and innermost and outermost absorbers are made from steel. To provide optimal segmentation in (η, ϕ) space the plastic scintillators are divided into 16 η segments, thus a segmentation of$(\Delta\eta, \Delta\phi) = (0.087, 0.087)$ is achieved.

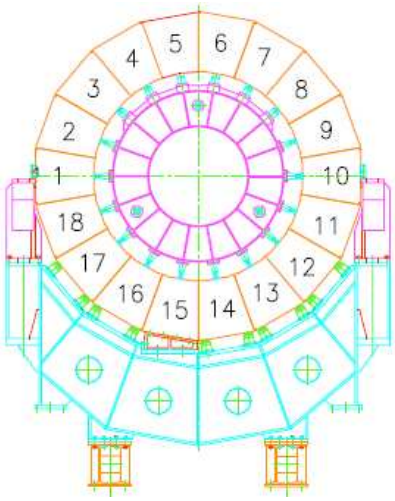

Figure 2.12. Drawing of the HB wedges with numbering scheme.

As scintillator material, 3.7 mm thick Kuraray SCSN81 plastic has been chosen. The HB wedges has four divisions covering a distance of $\Delta\phi = 5^o$ with an index from 1 to 4. Each division is covered by a tile and located on tray and each wedge is covered by a single tray system. The light coming out of the tile scintillators is carried by optical fibers to optical connectors. Two types of optical fibers, wavelength shifting (WLS) and clear fibers, are used. The wavelength shifting fibers collect the light from the scintillator by covering the outer borders of scintillator plane with a single line. The light is delivered to the optical connectors at the end of the tray by the clear fibers. Figure 2.13 shows the cross section of a scintillator tray system. 108 scintillator trays compose one layer of a wedge which has 16 layers. The first layer is placed in front of the first absorber plate so that hadronic showers developing before the HB could be

collected.

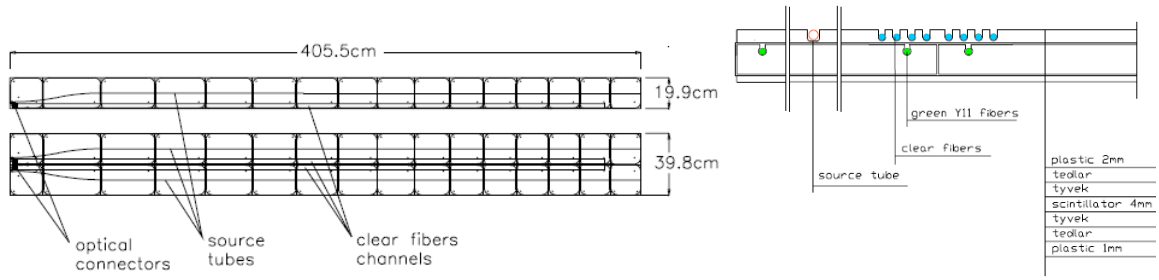

(a) Top view (b) Front view

Figure 2.13. Cross sectional view of scintillator tray system from different planes.

After the optical connectors the light is carried via optical fibers to an optical decoding unit (ODU) which brings the light to hybrid photodiodes (HPD). The hybrid photodiodes will be explained later in detail. Also for the calibration purposes there are optical cables carrying the laser and LED lights whose sources are located outside the detector. These optical cables are fed into HPDs directly and also to scintillators in layer 9.

There are 16 towers in η. The towers 1-14 have single depth so that they are connected to single read-out channels. However towers 15 and 16 have three depths and two of them belong to the HB while the other belongs to the endcap (HE) read-out. Overall, including both the HB+ and the HB-, the hadron barrel calorimeter has 2592 read-out channels.

2.4.2. Endcap Calorimeter (HE)

The hadronic endcap calorimeter extends the pseudorapidity range of the HCAL up to $|\eta| = 3.0$. Absorber material of the HE is brass. Design of the HE is challenging due to its geometry and location at each end of the 4 T solenoid magnet. It requires a very accurate tower structure and a complicated read-out system. It is attached to the muon endcap yoke.

To minimize the gaps between the HB and the HE is very important. This is the main requirement of the design of the HE absorbers in region close to the barrel

detector. The 79 mm thick brass plates formed a self-supporting hermetic construction with 9 mm gaps in between to insert the scintillators. The total interaction length is about 10. A picture of the ECAL absorbers attached to the muon endcap yoke is shown in Figure 2.14.

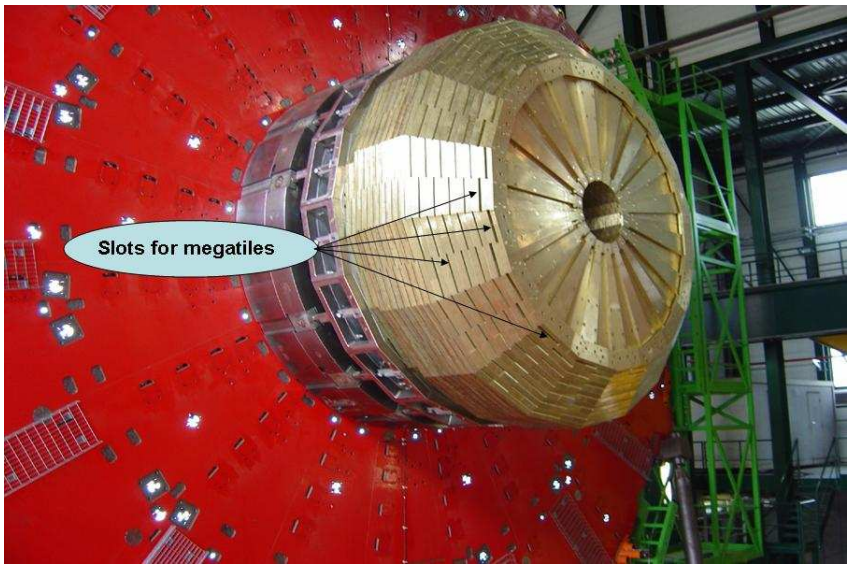

Figure 2.14. The HE absorbers attached to the muon endcap yoke showing the gaps for scintillators.

The light produced by the particles traversing the scintillators will be collected by WLS optical fibers. Because of the endcap geometry, the scintillators are cut as trapezoidal shapes and carved to insert the WLS optical fibers. The collected light is delivered to clear fibers to be carried to the optical connectors and then to the photo detectors. The design of the scintillator trays (Megatiles) is shown in Figure 2.15(a). The trays are inserted into the gaps between absorbers as shown in Figure 2.15(b).

The segmentation of the HE changes depending on the pseudorapidity. For the region below $|\eta| = 1.6$, the segmentation is $\Delta\eta$ x $\Delta\phi = 0.087$ x 0.087 just the same as the HB. As the pseudorapidity region goes beyond $|\eta| \geq 1.6$ the segmentation becomes $\Delta\eta$ x $\Delta\phi = 0.17$ x 0.17. The HE wedges cover $\Delta\phi = 20^o$, thus a total of 36 wedges together in HE- and HE+. The tower numbering is different compared to the HB. The towers closer to the center of the endcap cover $\Delta\phi = 10^o$ while the outer towers $\Delta\phi = 5^o$. The tower geometry on a wedge is shown in Figure 2.16.

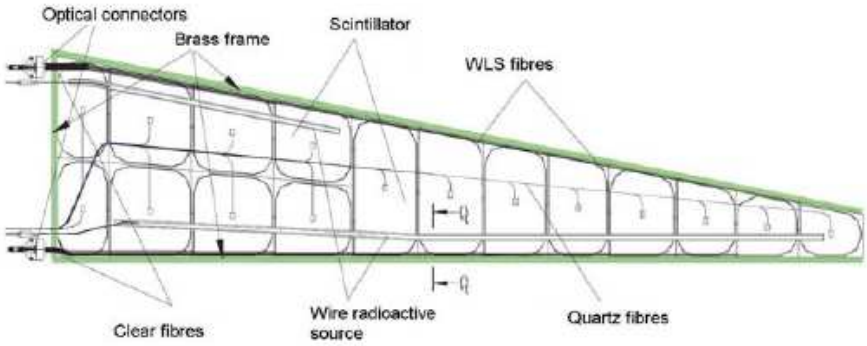

(a) Scintillator tray design

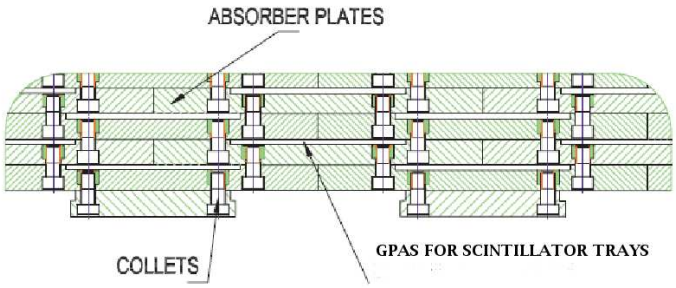

(b) Absorber structure

Figure 2.15. The scintillator tray and the absorbers.

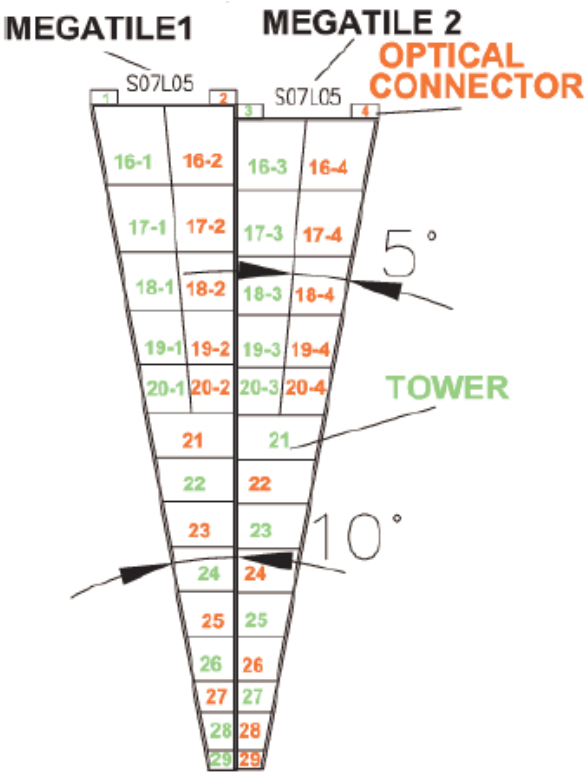

Figure 2.16. Tower geometry on a wedge with the numbering scheme.

The towers close to beam line have three depths while the rest of the towers has two depths. The tower number starts from $i\eta = 16$ and goes to 29. The tower $i\eta = 16$ has three depths and depths 1, 2 belong to the HB and depth 3 belongs to the HE. Therefore the HE calorimeter has 2160 total number of channels, read out separately. Figure 2.17 shows the longitudinal and angular segmentation of a quarter of the HE detector.

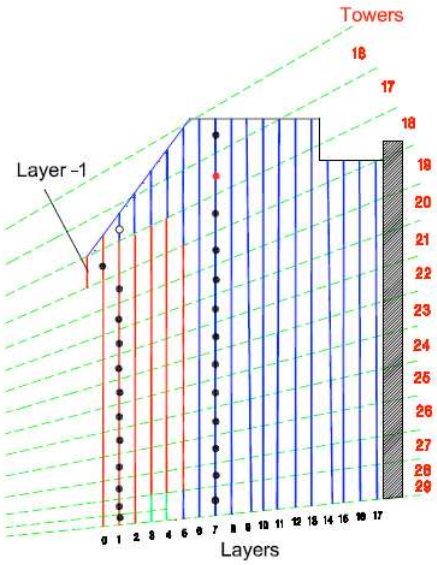

Figure 2.17. Longitudinal and angular segmentation of a quarter of the HE detector.

2.4.3. Outer Calorimeter (HO)

The purpose of building the hadron outer calorimeter is to catch the tails of hadronic showers and improve the missing transverse energy measurement. It is located between the magnet and the muon system. Its pseudorapidity coverage is up to $\eta = 1.3$ and the distance from the beam line to the HO is about 4000 mm. The HO is composed of a total of five barrel rings and each ring is numbered as -2, -1, 0, 1, 2, where $\pm$ sign corresponds to the sign along the z axis (beam line). The center ring has two layers while the others have single layers. With the HO the total interaction length of the CMS calorimeter is extended to 11.8 λ_ℓ.

The HO rings are divided into 12 sectors, each covering $\Delta\phi = 30^o$. These slices are also divided in η. The number of η sectors are different for each ring. The ring

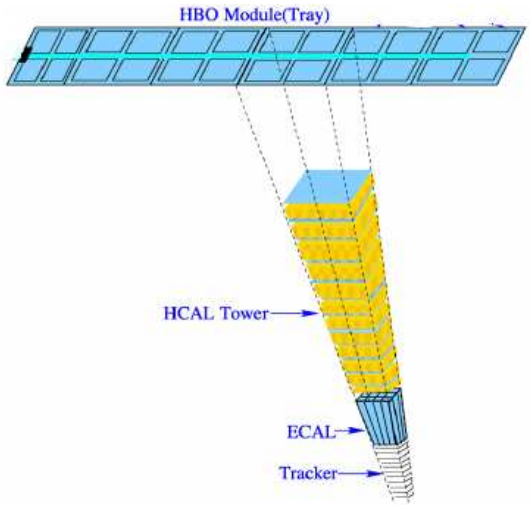

Figure 2.18. A drawing of the HO tray segment, matching the segment of the CMS calorimeter system.

number 0 has 8 η divisions. The ring number 1 has 6 η divisions while the number 2 ring has 5 η divisions. Thus a tile covers such a $\Delta\eta$ x $\Delta\phi$ cell in the HO. This segmentation is designed to match the projection of an HB tower into an HO tower. Figure 2.18 shows the HO tray and its matching towers in the previous calorimeters. These tiles in each ϕ slice are placed together on a scintillator tray. A tile covers a ϕ slice on a ring and all the tiles together compose the HO rings as shown in Figure 2.19

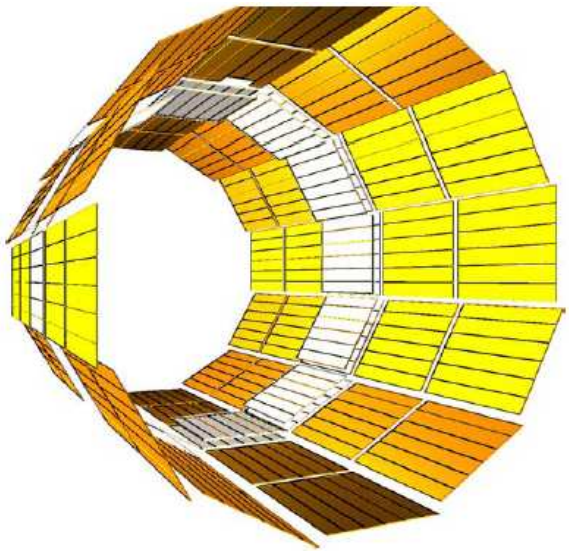

Figure 2.19. The HO rings layout composed by the trays. White ring has two layers.

A scintillator tile is divided into four grooves with optical WLS fibers inserted

into these grooves to collect the light in a large tile efficiently. Each tray covering a $\Delta\phi = 5^o$ slice contains 5, 6, and 8 tiles in rings ± 2, ± 1, and 0, respectively. Six trays together covers one $\Delta\phi = 30^0$ sector in a layer. Total number of channels in the HO is 2160.

The light collected from the tiles via WLS fibers is carried to the optical connectors by clear optical fibers. Optical connectors deliver the light to the photodetectors. The HO detector uses the HPD as photodetectors. But due to non-stability problems of HPD under large magnetic field, recently some silicon photo multipliers (SiPM) are inserted for testing purposes.

2.4.4. Forward Calorimeter (HF)

The forward calorimeter will experience huge amounts of particle flux. The radiation doses of up to Grad over ten years of operation at designed luminosity is expected at the forward calorimeter region. This harsh radioactive environment drives the choice of quartz fibers as the active medium. They can operate with only a few percent transparency loss in the UV wavelengths.

The forward calorimeters (HF) are located at each side of the CMS. Its pseudorapidity coverage is $3.0 < |\eta| < 5.0$ which is 40% of the available phase space of the CMS. The HF is a sampling calorimeter composed of steel as absorber material and quartz fibers embedded in the absorbers as active material. The main objectives of the HF is to improve the missing energy measurement and the identification of very forward jets. It has two parts, HF- and HF+, and each part is constructed as a cylinder around the beam line with an active radius of 1300 mm and a length of 1650 mm.

The HF wedges has $\Delta\phi = 20^o$ width and there are 18 wedges total at each part. The wedges are divided into two ϕ segments and 12 η segments, thus one wedge has 24 towers. The towers have a segmentation of $\Delta\eta$ x $\Delta\phi$ = 0.175 x 0.175. The quartz fibers inserted into the holes are parallel to the beam line. There are two different lengths of fibers, long (L) and short (S). The long fibers run over the full depth of

the absorbers while short fibers start from a depth of 220 mm. Each tower has one bundle of Long and and one bundle of Short fibers. These are read-out separately to enable to distinguish electromagnetic and hadronic showers. A large fraction of the electromagnetic showers are expected to deposit their energy in the first 220 mm of the absorber while hadronic showers deposit roughly the same amount of energy in both length fibers. Figure 2.20 shows five wedges with quartz fibers inserted and connected to the photo multiplier tubes (PMT). The HF has 1728 total number of channels.

Figure 2.20. The HF wedges.

2.4.5. Electronics

The HCAL detector electronics can be divided into two parts; on-detector, located on the detector itself, and off-detector, located in the higher levels of the CMS cavern. On-detector electronics consists of hybrid photodiodes and front-end electronic cards containing the charge-integrator and encoder (QIE). Off-detector electronics consists of the HCAL trigger readout (HTR) cards integrated with the global CMS electronics, trigger and DAQ systems. Figure 2.21 shows an overview of the HCAL read-out electronics including the connections with Level-1 trigger and condition database (CDB).

The light produced by the particles passing through the scintillators is carried to the HPD via wavelength shifting fibers, clear optical fibers, and then optical decoder units. The multi-pixel hybrid photodiodes convert the optical signal to electronic signal with a certain gain which is determined by the high-voltage applied to the HPD.

The QIE cards convert the analog signal from photodetectors of the HCAL to the digital signal. Each HPD is connected to three front electronic cards (FE) and each FE contains six QIE cards. Therefore signal from each pixel of the HPD is digitized by a single QIE. The digitization takes longer than the LHC bunch crossing time of 25 ns. The QIE has a pipeline composed of four capacitors and each analog signal (25 ns) is connected to those capacitors in turn. The charge accumulated in capacitor is converted to a 7-bit non-linear scale, so called ADC count or fC. Later this non-linear scale will be converted to a linear scale called linearized ADC or nominal fC.

During the initialization of the electronics, calibration constants, pedestals, gains, and map information are downloaded from condition database. This information is needed to process signal read-out accurately. In addition, some information like temperature, humidity and some other constants are recorded to the condition database for calibration and stability monitoring purposes.

The digitized signal from three QIE cards combined with the monitoring information compose a 32-bit data package at a rate of 40 MHz. These data are sent to the HCAL trigger read-out boards (HTR). The HTR receives data from 48 channels and creates the HCAL trigger primitives and send them to the regional calorimeter trigger system. It has Level-1 trigger pipeline for synchronization purpose. To generate the level-1 trigger primitives, the data from the QIE cards are need to be linearized and this requires ADC to GeV gain constant to be downloaded from the condition database. Then the linearized signal in GeV is converted to transverse energy by using a table as shown in Table 2.1.

The timing synchronization is very important for read-out electronics, hence for the data. The optical path distance to the HPD and the time of flight from the interaction point are different for each read-out channel. This will result in a time shift between the signals from different channels. Therefore the timing of signal from each channel is needed to be synchronized relative to each other. Another timing synchronization is needed to be made according to the timing of the LHC machine. This synchronization is performed by the channel control ASIC (CCA) that controls

Table 2.1. The HCAL trigger tower sizes in η and ϕ space.

Tower index	$\lvert\eta_{max}\rvert$	Detector	Size	
			η	ϕ
1–15	$0.087\times\eta$	HB	0.087	5°
16	1.392	HB, HE	0.087	5°
17–20	$0.087\times\eta$	HE	0.087	5°
21	1.830	HE	0.090	5°
22	1.930	HE	0.100	5°
23	2.043	HE	0.113	5°
24	2.172	HE	0.129	5°
25	2.322	HE	0.150	5°
26	2.500	HE	0.178	5°
27	2.650	HE	0.150	5°
28	3.000	HE	0.350	5°
29	3.314	HF	0.461	20°
30	3.839	HF	0.525	20°
31	4.363	HF	0.524	20°
32	5.191	HF	0.828	20°

the QIE clock and allows fine-skewing of the integration phase relative to the LHC clock.

The forward hadron detector (HF) uses photomultiplier tubes (PMT). The optical signal is generated by quartz fibers which produce light via Cherenkov radiation. The Cerenkov radiation happens when a charged particle travels through matter with a speed greater than the speed of light in that medium. The signal generated in the quartz fibers is delivered to the PMT front window directly by quartz fiber bundles.

The pulse shape for the HPD and the PMT are different. The scintillators in the HB, HE, and HO with the HPDs create a signal pulse, of which ∼70% of the pulse is included in a single bunch crossing (25 ns). While quartz fibers for the HF with the PMTs produce much faster pulses such that the total pulse width is 10 ns which means 100% of the energy is contained in ∼10 ns.

The *in-situ* calibration of the HCAL will be performed using the laser system. The quartz fibers deliver the laser from the off-detector source to the wedges of the

HCAL. The path length from the source to the wedges are equalized. There are three calibration fibers for each wedge. Two of them are fed into the HPDs directly and the other one is fed into two 9th layer of the wedges. This calibration system will synchronize the timing of the HB and HE channels. However only test beam data were used to synchronize the HO and HF channels.

The normalization for physics analysis depending on the LHC real time luminosity will be contributed by the HF luminosity monitoring. The desired precision of the luminosity measurement is to provide the average luminosity with a 1% statistical uncertainty at 1 Hz rate which means it will be updated every second.

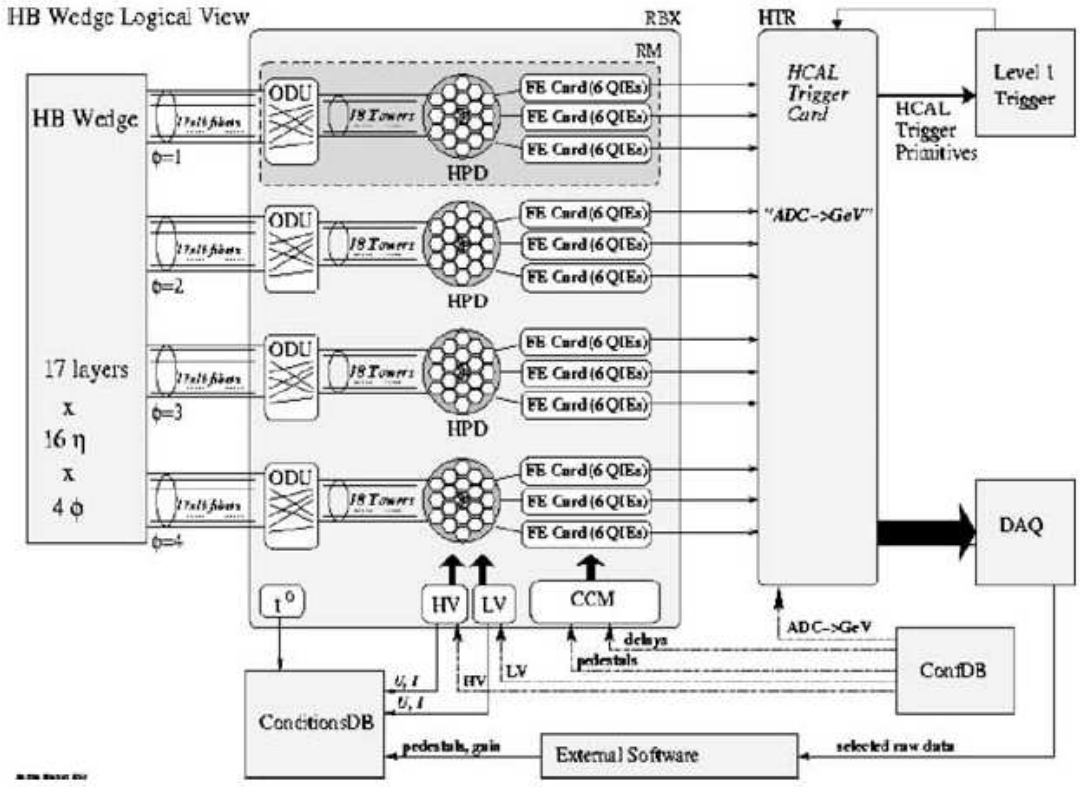

Figure 2.21. The complete layout of the HCAL electronics with condition database and Level-1 trigger connections

2.5. Muon System

The Muon detection is very important for the CMS as its name implies. Muons are relatively easy particles to reconstruct due to their minimum ionization charac-

teristics, less affected by the tracker and calorimeters while they can leave signal in the entire detector. These factors make muons to have less background and easy to reconstruct with high position and momentum resolution given a good muon system, high magnetic field, good tracker, and calorimeters.

The CMS muon system [6] consists of three types of particle detectors; drift tubes, cathode strip chambers, and resistive plate chambers placed with massively instrumented flux-return system. Pseudorapidity region up to $\eta = 1.2$ (barrel region) is covered by the drift tube system. The cathode strip chambers cover $0.9 < |\eta| < 2.4$ endcap region. Due to trigger concerns a dedicated muon trigger system composed of resistive plate chambers is placed in both barrel and endcap regions.

2.5.1. Drift Tube System

Four layers of drift tube system located inside and outside of the layers of iron flux-return yoke cylindrical rings compose the barrel muon detector. First three layers have 60 drift chambers while the most outer one has 70. The idea of using four drift chambers instead of two, one inside and one outside of the return yoke, is driven by the concern of sufficient measurement and identification of muons despite the massive and intense iron yoke material. Therefore two more drift chambers are placed inside the return yoke rings.

The basic unit of drift chambers is a single drift tube which is shown in Figure 2.22. The tubes are filled with a gas mixture of Ar/CO_2. Four layers of these tube cells compose a super layer (SL). These layers are arranged such that even number layers shifted by half the with of the tube relative to odd number layers to increase the track identification. The bunch crossing and track identifier (BTI) system is the trigger unit in each trigger board (TRB) and provides track and bunch crossing information of an identified muon in the barrel region. The SLs covering two ϕ segments are combined in track correlator (TRACO) with the BTI information. The TRACO and BTI are grouped in trigger services (TS) as two components. The TRACO provides transverse ϕ information to TSϕ component while the BTI providing longitudinal θ information

to TSθ. The information sent from each TS sector to the sector collectors (SC) is coded and transmitted to the regional trigger.

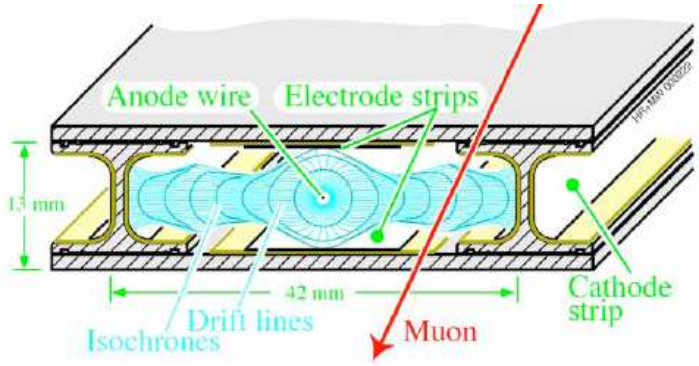

Figure 2.22. Schematic view of a drift tube.

2.5.2. Cathode Strip Chambers

The cathode strip chambers (CSC) [7] are multi-wire chambers whose wires are parallel to the strip cathodes as shown in Figure 2.23. The cathode-strips provide ϕ information while multi-wires provide radial information. A cathode strip chamber consists of six layers. The choice of CSCs for the endcap muon identification is due to their ability to operate in non-uniform magnetic fields at high rates.

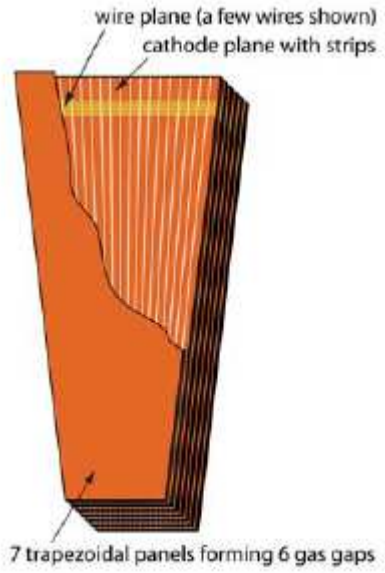

Figure 2.23. Layout of a cathode strip chamber.

The CSC can provide precise measurements and trigger for muons. Each CSC

is equipped with cathode local charged track (CLCT) and anode local charged track (ALCT) boards. CLCT board triggers hits from cathode strips while ALCT board triggers anode wire hits. A local charge track is constructed if at least four of six layers produce hits. These hits can be either from cathode strips or anode wires depending on the muon path. The cathode strips can provide track resolutions of about 1-2 mm. The CLCT board finds the strip with the maximum signal amplitude and compares it with the strips at each side of it. The information from all six layers are combined to improve the resolution. The ALCT checks hits in layers for every bunch crossing and requires at least two layers with coincident hits to provide information on the bunch crossing in which the muon is produced.

2.5.3. Resistive Plate Chambers

Resistive plate chambers (RPC) are composed of parallel plate layers filled with gas. They provide good longitudinal and timing resolution better than a bunch crossing, 25 ns. The RPCs are dedicated for muon triggering and placed in both endcap regions. They are combined with drift tubes in barrel region and cathode strip chambers in endcap region to provide the required muon identification and momentum measurement requirements of the CMS.

There are six layers of RPCs in the barrel region. Four of them are placed at each side of the two innermost drift tube chambers. The other two are placed at inner sides of the two outer drift tube chambers. The RPC operates with a gas mixture of 96.2% $C_2H_2F_45$, 3.5% C_4H_{10}, and 0.3% SF_6. A gas recirculation system is needed due to the cost of the gas mixture used for the large RPC volume. The basic RPC unit is composed of double gap modules where one gap refers to upper gap and the other refers to lower gap. Depending on the location of the RPC, each chamber consists of either 2 or 3 double gap modules in the barrel region. For endcap region each RPC chamber is composed of double gap modules. Figure 2.24 shows the schematic layout of 2 and 3 double gap RPC modules.

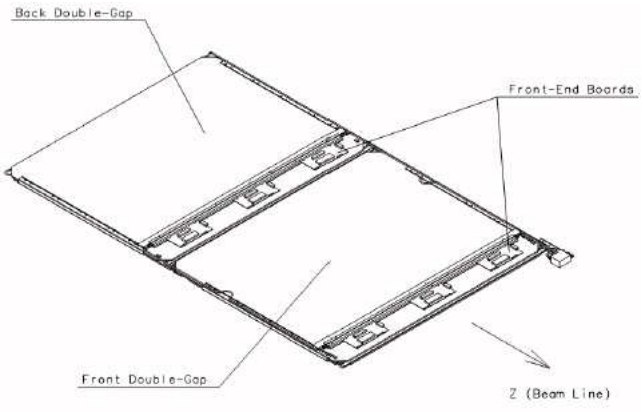

(a) 2 double-gaps

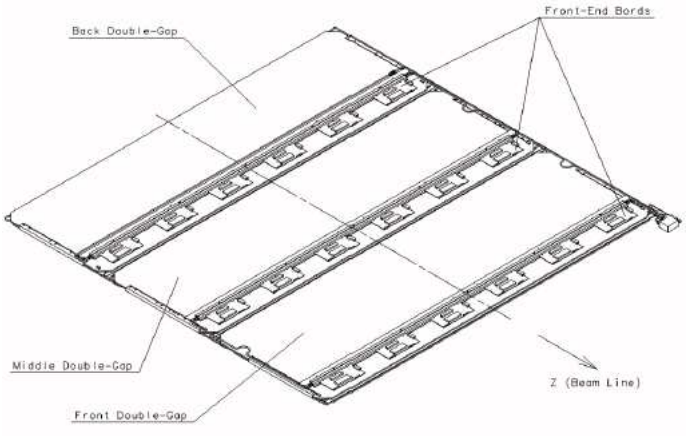

(b) 3 double-gaps

Figure 2.24. Schematic layout of the RPC double gap modules.

2.6. Trigger and Data Acquisition Systems

The CMS trigger system has two-level structure, Level-1 (L1) and high level trigger (HLT). The L1 trigger reduces the event rate from 40 MHz to 10 kHz by custom and programmable electronics processing rough information from calorimeter and muon triggers. The Level-1 trigger [8] electronics is designed as field-programmable gate array (FPGA), application-specific integrated circuit (ASIC), and programmable memory lookup tables. However the HLT is a software system and can use the complete read-out system and can make high-resolution calculations with complex algorithms. These algorithms are the user defined software and will be developed in time.

The L1 trigger consists of local, regional, and global levels. Trigger primitives are generated by local triggers and shaped together at regional level. Each object at this level is sorted according to its rank determined by various quantities like energy and momentum. The global calorimeter or muon trigger picks the highest rank object and pass it to the global trigger which is the top level of the L1 trigger system. A schematic structure of the Level-1 trigger is shown in Figure 2.25.

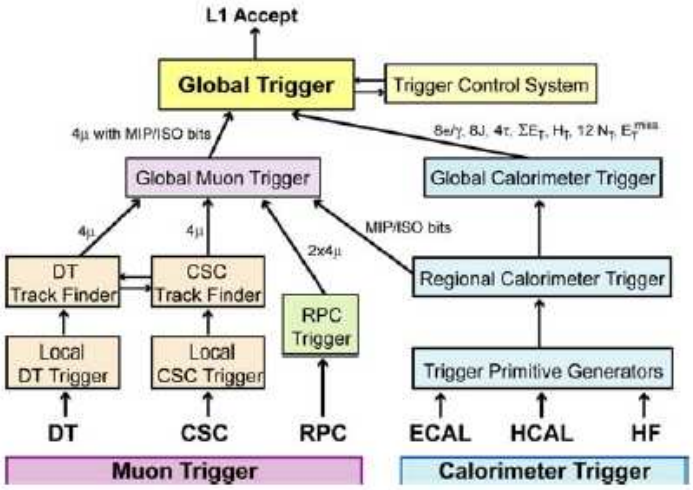

Figure 2.25. A schematic layout of L1 trigger system.

2.6.1. Calorimeter Trigger System

The calorimeter trigger has three-level architecture. These are local calorimeter trigger or trigger primitive generators (TPG), regional calorimeter trigger (RCT), and global calorimeter triggers (GCT).

The local calorimeter trigger is composed of on-detector and off-detector electronics. The energy deposition in the trigger towers in the ECAL and/or the HCAL are summed up and converted to the transverse energy, E_T. Then it is sent to the regional calorimeter with additional important information like isolation, minimum ionization, and τ-veto.

The calorimeter region is made of 4x4 trigger towers in the ECAL and the HCAL, while a single trigger tower corresponds to a single calorimeter region in the HF. The regional calorimeter trigger (RCT) determines the electron/photon candidates and transverse energy in one calorimeter region. The RCT decides whether electron/photon candidate is isolated or not. Non-isolated candidates need to pass two vetoes related to the shower profile. The first one is if the shower is contained in 2x5 ECAL crystals. The second one is the fraction of the electromagnetic energy to the hadronic energy which is determined by the energy deposited in ECAL and HCAL. This ratio should be less than 5%. If one of those two requirements fail, the candidate is labeled as non-isolated. If it passes those requirements with all the eight neighboring towers, it is labeled as isolated. The regional calorimeter sends four isolated and four non-isolated electron/photon candidates to the global calorimeter trigger. The RCT also sums the transverse energy in a calorimeter region, but not in the HF. It decides if the jet is a τ jet or quark/gluon jet. If the energy deposition is narrower than 2x2 trigger towers in a calorimeter region where the towers are 4x4, it will be labeled as a τ jet in the region $|\eta| < 3.0$.

The global calorimeter trigger (GCT) uses the information coming from RCTs and determines the jets, the total transverse energy, the missing transverse energy, and number of jets. It sorts up to four quark/gluon jets and four τ jets in the HCAL region

$|\eta| < 3.0$, and four jets in the HF region and sends to the global trigger. It computes the direction and the magnitude of the total transverse energy and missing energy in transverse plane coordinates, $\hat{x}$ and $\hat{y}$, within pseudorapidity region up to 5.0. These quantities are also sent to the global trigger by GCT. In addition, the GCT provides jet multiplicity above 12 different E_T thresholds. It also provides information for muons and muon isolation to global muon trigger system.

2.6.2. Muon Trigger System

The Muon sub systems contributes to the muon trigger. The DTC, the CSC, and the RPC are designed to provide tracking in η and ϕ space with bunch crossing information for triggering purposes. This information is combined by the global muon trigger and is passed to the global trigger of the CMS detector.

The DTC local trigger has four components collecting tracking and bunch crossing information. First one is the bunch crossing and tracking identifier (BTI) which looks for coincident hits at least in four of the six layers in a drift tube chamber to trigger. Four BTIs in the inner region and 12 BTIs in the outer region are connected to track correlators (TRACO). The TRACO makes correlation of the track segments measured in the inner and the outer ϕ segments. It passes at most the two track-segment data sets per bunch crossing to the trigger servers (TS). The TS has two, TSθ and TSϕ, components. The TSθ receives information from TRACO while the TSϕ receives from the BTI. The TS selects the better tracks among all that are received. Finally the sector collectors (SC) receive the position, the momentum, and the track information from each sector and transfers to the drift tube trigger track finder (DTTF).

In the endcap region the cathode strip chambers (CSC) are used. A muon track segment called local charged track (LCT) is composed of the position, angles and bunch crossing information. The LCTs are reconstructed from the anode and cathode hits in a chamber. The best two LCTs in a chamber are sent to the cathode strip chamber track finders (CSCTF). The CSCTF construct the muon tracks in the endcap region. The CSCTF and DTTF transfers up to four muon candidates to global muon trigger.

The resistive plate chamber trigger collects hits from multiple layers. The pattern comparator trigger logic looks for three hits coincident in time out of four planes of the RPC chambers. It assigns the transverse momentum and charge by comparing strip hits of all four muon stations. The RPC trigger also uses information from the outer layers of the hadronic outer calorimeter (HO). The RPC trigger sends eight muon candidates, four for the barrel region and four for the endcap region, to the global muon trigger for every LHC bunch crossing.

The global muon trigger receives sixteen muon candidates for every 25 ns. It also receives isolation and minimum ionizing particle information from the global calorimeter trigger (GCT). If the muon candidates and information from GCT match, the kinematic variables will be merged by the global muon trigger. The major responsibility of the global muon trigger is to clean the muon background and improve the muon efficiency by using information from almost all the CMS detector.

2.6.3. Global Trigger

The final decision to accept or reject the event is made by the global trigger (GT). The decision depends on the objects and the related information sent by the GCT and GMT. GCT sends the electron-photon, hadronic and τ jets, the missing energy, twelve different jet-multiplicity above twelve different thresholds, and H_T which is the sum of the jet p_Ts above a pre-defined threshold. The GMT sends the muon candidates.

The input signals from GCT and GMT are called technical triggers. The calculations based on basic and/or complex algorithms with the technical triggers are performed by the global trigger logic (GTL) stage. The results of the calculations are sent to the final decision logic (FDL). The FDL makes the decision to accept or reject the event. In case of *accept* decision, a Level-1 accept signal (L1A) is generated and delivered to the sub-systems to record the event.

The delivery of the L1A is controlled by the trigger control system (TCS). This delivery is made depending on the status of the sub-systems of the CMS. The status

of a sub-system could be in the following predefined states: ready, overflow warning, synchronization loss, busy, disconnected, and error. This status signal is provided by the trigger throttle system (TTS).

2.6.4. Data Acquisition (DAQ)

The CMS data acquisition system will perform the data collection, data analysis and reduction, event building, filtering and recording at a rate of 100 kHz. The L1 trigger will reduce the LHC event rate from 40 MHz to 100 kHz. The DAQ will receive $\sim$ 100 GByte/s data flow. The data will be sent to the event filter to do the physics selection and reduce the event rate to 100 Hz. The events after filtering will be recorded at 100 Hz rate. The design architecture of the DAQ system is shown in Figure 2.26.

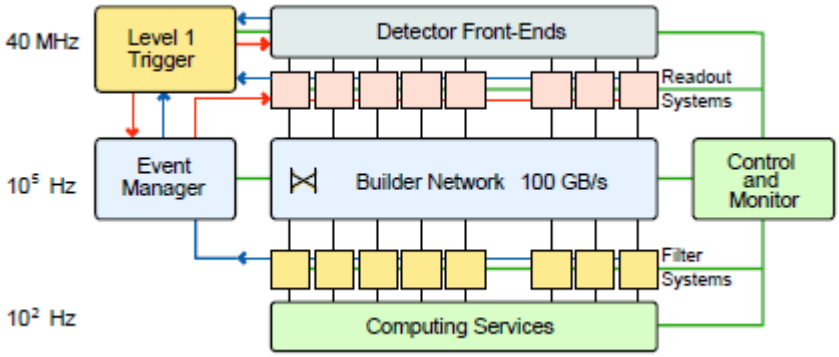

Figure 2.26. Design architecture of the DAQ system.

The sub-detector systems store digitized data in the pipeline buffers and wait for the L1A signal from timing and trigger control (TTC) before transferring them to the DAQ system. This data transfer is performed by the front end drivers (FED) and front end read-out links (FRL). The FRL reads the data from FED and might merge the data from two FEDs into one if necessary. The event manager processes the event building and filtering of the data. There is also a testing mechanism to test the full central DAQ system before starting the data taking.

3. PHYSICS RECONSTRUCTION

In this section the reconstruction algorithms for the physical objects will be discussed. These objects are the electrons, muons, jets, and missing energy. There are several different types of algorithms to reconstruct and identify these objects. The algorithms are characterized depending on the properties of the objects and the sources of information collected. These sources might be the energy deposition in the calorimeters and/or hits in the tracker, and in the muon system. The important quantities about these energy depositions and hits are the magnitude, shape, and the timing information.

3.1. Electron Reconstruction

The reconstruction of electrons [9] is performed with the information collected from the electromagnetic calorimeter (ECAL) and the tracker in CMS. Electron reconstruction starts with Super Clusters (SC) in ECAL. Super Clusters are 5×5 ECAL crystals containing energy deposited by particles that may be electrons as well as other particles and jets. Then the tracks, reconstructed by a Gaussian Sum Filter (GSF) in CMS tracker, matched to the SC to form the *GSF* electrons. The next step is the isolation of the candidate followed by some electron ID requirements. The final step is passing the High Level Trigger (HLT).

3.1.1. Electron Clustering

The electrons and photons deposit their energy via producing an electromagnetic shower in the ECAL. High energy electrons deposit more than 95% of their energy in a 5×5 crystal cell. In CMS, electrons first interact with the tracker material. Electrons traversing the tracker radiate photons through bremsstrahlung when these radiated photons reach ECAL, they are spread in ϕ relative to the initial electron. Depending on the momentum of the electron, this effect can be quite large. Therefore it is important to contain these photons coming from bremsstrahlung when measuring the electron

energy. For this purpose, different super-clustering algorithms are used in barrel and endcap regions specific to their geometry.

These algorithms used in endcap and barrel regions are called "Island" and "Hybrid" [10] and used in endcap and barrel regions, respectively. The Island algorithm searches crystals above a certain threshold which are called *seed* crystals. It collects all the seeds found and removes the ones which are close to the higher energy seeds. The algorithm uses the seed crystal with the highest energy to cluster the energy deposition. It looks for the crystals in both directions of ϕ with the same η. It collects the crystals until a crystal with zero energy or an increase in the energy are detected. Once the clustering for the one η is completed it moves to next η and do the same ϕ clustering. This will continue until it finds zero energy or an increase in the energy of the crystal in both η directions. Once the crystal is used for clustering it will not be used again. Hence no double counting of the energy will occur.

The Hybrid algorithm looks for the seed crystal with the highest energy that should be above a certain threshold. Then it constructs 1×3 crystal dominoes by collecting the energy in the crystals with the same ϕ of seed crystal and its neighbours in both η directions. If the energy of the seed crystal is high enough, 1×5 dominoes can be clustered with the next two neighbours of the seed crystal in both η directions. Then those crystal dominoes clustered together along both ϕ directions as super-clusters. This algorithm helps collect the energy spread in ϕ by the photons coming from bremsstrahlung.

3.1.2. Electron Track Reconstruction

The electron track reconstruction starts with initial tracks, also called *seed*, found by the *seed generator*. A seed is generated when at least two hits in the pixel detector are found. These hits must be in the direction of the super clusters in the ECAL to avoid too many possible hit combinations. After finding the seed hits in the pixel tracker, compatible hits in the silicon tracker layers are searched. The search for hits in the tracker continues until the last layer of the tracker or no hits found in two successive

layers.

Then those hits are fit using the Gaussian-Sum Filter [11] and all possible trajectories are built. If more than one compatible hits found in a layer, the number of trajectories will be proportional to the number of compatible hits in the layer. A minimum five compatible hits are required to build a track. There will be no χ^2 cut applied during the building process of the trajectories. However the two tracks with the smallest χ^2 will be kept.

Two important issues will be the matching of the tracks to super-cluster and bremsstrahlung estimation due to tracker material. The matching between the tracks and super-cluster can be made both by using the initial track at vertex and the most outer part of the track. The fraction of the energy loss due to the bremsstrahlung can be estimated with the relative difference between momentum of the track at the inner-most and outer-most states as,

$$f_{brem} = \frac{(p_{in} - p_{out})}{p_{in}}. \tag{3.1}$$

3.1.3. Electron Identification

In CMS all the possible electrons are collected in *electron collection*. This collection might also include fake electrons or photons and very low energy electrons. For physical analysis with electrons, it is needed to select the desired electrons. This selection requires some electron identification procedure [12].

There are two types of electron identification. The first one uses fixed threshold cuts called "fixed threshold identification". The second one categorizes the electrons according to their energy loss due to bremsstrahlung and uses different threshold cuts for each type of electron. This method is called "category based identification". Both

method uses different cut values depending on the location of the electrons. In other words, the cut values for barrel and endcap electrons are different in both identification method.

The bremsstrahlung fraction, defined in Equation 3.1, is used to categorize the electrons. There are three electron categories, *low-brem* electron, *bremming* electrons, and *bad track* electrons. Each of those electron categories have different selection cuts according to category based electron identification method.

The selection cuts will be categorized as "tight" and "loose" cuts. The choice will depend on the physics analysis. If the expected background is high, then tight selection will be used to reject the background as much as possible. If the expected background is not high or one wants to keep more electrons, then the loose selection might be used.

There are in total five quantities which are used to select the electrons:

- The ratio of the electromagnetic energy to the hadronic energy. It is determined by taking the ratio of the energy deposited in the hadronic calorimeter and the electromagnetic calorimeter; E_{had}/E_{em}.
- η difference between the super-cluster and the track of the electron at the inner tracker; $\Delta\eta_{in}$.
- ϕ difference between the super-cluster and the track of the electron at the inner tracker; $\Delta\phi_{in}$.
- Shower shape of the electron super-cluster in $i\eta$;

$$\sigma_{i\eta i\eta} = \frac{\sum_k w_k (i\eta_k - \bar{i\eta}_{5\times5})^2}{\sum_k w_k}. \tag{3.2}$$

where the index k runs over all the crystals in the 5×5 block of super-cluster cyrstals, $i\eta_k$ is the integer eta position of the k^{th} crystal, $\bar{i\eta}_{5\times5}$ is the energy weighted mean of the integer eta, w_k is the weight of the k^{th} crystal.

- Relative isolation which is defined as the sum of the energy around the electron track in the ECAL, HCAL, and the transverse momentum in the tracker divided by the transverse momentum of the electron track;

$$RelIso = (\sum_{\Delta R<0.3} E_T(ECAL) + \sum_{\Delta R<0.3} E_T(HCAL) + \sum_{\Delta R<0.3} P_T(tracker))/P_T. \tag{3.3}$$

3.2. Muon Reconstruction

Muon reconstruction [13] uses information from the muon system, tracker, and calorimeters. The minimum ionizing particles penetrate all the detector parts, thus they produce signals in all the sub-detectors. There are two types of muons in CMS. These are *stand alone* and *global* muons. First one is reconstructed only in the muon system. The second one uses information from the tracker, calorimeters, and the muon system.

The muon system is composed of three different gaseous type detectors, the cathode strip chambers, the drift tubes, and the resistive plate chambers. The resistive plate chambers provide precise triggering while other two allow precise tracking and momentum measurement for muons. The high magnetic field helps muon reconstruction by its bending power on the muon tracks. The muons, produced in the interaction point, first interact with the tracker material and the electromagnetic and hadronic calorimeter before reaching the muon system.

3.2.1. Stand-Alone Muons

The stand alone muons are reconstructed locally. The hits in a chamber are combined to provide a track segment. The compatible track segments are used to build a local muon track. The tracks are built from inside towards outside. However muon track building may be both forward and backward depending on the location of a track segment.

3.2.2. Global Muons

The global muon reconstruction combines the hits from the tracker with the stand alone muon reconstructed in the muon system. The muon tracks in the tracker should be compatible with the stand alone muons. This is provided by defining the desired location of the track inside the tracker according to the location of the stand alone muon. If a muon track, constructed from the hits in the tracker, matches a stand alone muon, then a global muon will be constructed. Additional filtering, backward and forward re-fitting, and smoothening will be applied during the reconstruction of a global muon.

3.2.3. Muon Identification

The muon identification is focused on especially global muons because they are the point of interest for any physics analysis with muons in the final state. The muon identification is rather complicated, since there are more information from all the detectors for a global muon.

The quantities used to identify the global muons:

- χ^2 of the global muon track fit.
- Impact parameter of the fit in the silicon tracker; d_0.
- Number of valid hits inside the tracker; N_{hits}.
- Energy deposition in the hadronic calorimeter; E_{HCAL}.
- Energy deposition in the electromagnetic calorimeter; E_{ECAL}.
- Relative isolation (Equation 3.3).

In addition there are also classification of muons depending on the number and quality of the track segments in the muon system. If there are at least two track segments, the muon will be called “TMLastStation” muon. If there is only one track segment, it will be called “TMOneStation” muon. Also there are “tight” and “loose” requirements for both global muon classes.

3.3. Jet Reconstruction

In particle physics, jets refer to collection of particles coming from the fragmentation (hadronization) of quarks or gluons. Jets leave energy in the electromagnetic and the hadronic calorimeters. They will also produce signals in the tracker if they are charged. Jets are classified according to the clustering algorithms and the input objects that are used to reconstruct them.

In CMS, there are two main types of clustering algorithms, *cone-type* and *sequential* [14]. Furthermore there are two *cone-type* algorithms, "Iterative Cone" [15], and "Seedless Interfaced-Safe Cone". Similarly, there are also two different types of *sequential* algorithms and these are the "k_T" and "Anti-k_T" algorithms. In total, there are four different clustering algorithms to find jets in the CMS detector.

3.3.1. *Cone-Type* Algorithms

The iterative cone algorithm creates an object list which consists of calorimeter towers or particles above a certain E_T threshold. The objects of the list are in descending order according to their E_T. The tower with the largest energy will be used to define a cone with a radius, R, in (η, ϕ) space around the tower itself. Then all the towers inside the cone are used to determine a probe jet with a direction and energy. After that a new seed will be defined by the direction of the probe jets. This new seed will be used to define a new probe-jet. This will continue until the axis of the consecutive probe-jets agrees with certain precision. If this condition is satisfied, the probe jet will be considered as a stable jet and will be included in the jet collection. The constituents of this jet will be removed from the object list. Then the whole procedure will be repeated for the remaining objects of the list. The cone size and the threshold for the seed objects can be adjusted. The Seedless Interfaced-Safe Cone (SISCone) algorithm does not require seeds to find jets. Instead it uses all the particles to determine the stable cones. This method is not iterative, thus requires less computational power compared to the iterative algorithm.

3.3.2. *Sequential* Algorithms

The sequential clustering algorithms utilize the distance information between input objects to find stable jets. The input objects could be stable particles or calorimeter cells above a certain energy threshold. The algorithms determine the minimum distance, d_{ij}, between the two objects, i and j and the distance of i^{th} object to the beam;

$$d_{ij} = min\{k_{T_i}^{2p}, k_{T_j}^{2p}\}\frac{R_{ij}^2}{R_{jet}^2}, \tag{3.4}$$

$$d_{iB} = k_{T_i}^{2p}, \tag{3.5}$$

where $R_{ij} = \sqrt{(\eta_i - \eta_j)^2 + (\phi_i - \phi_j)^2}$ and k_{T_i} is the transverse momentum of i^{th} particle. If the smallest distance is d_{ij}, the algorithms will merge i and j objects together and add into the list as a new object. Also the objects i and j will be removed from the list. If the smallest distance is the d_{iB}, then i^{th} object will be considered as stable jet and removed from the list of objects. The predefined quantity R_{jet} will be the size of the jets. It will ensure that all the objects with $R_{ij} < R_{jet}$ will be merged while all the clustered jets will be separated by at least R_{jet}.

The parameter p in Equations 3.4 and 3.5 will determine the relative power of the momentum with respect to the geometrical distance. The name of the algorithm will depend on the choice of p;

p	Name
1	k_T
0	Cambridge/Aachen
-1	Anti-k_T

Jet classification also depends on the input objects that are used by the algorithms to find jets. These input objects are only calorimeter towers, calorimeter towers together with tracks from the tracker, and individual reconstructed particles. Therefore there will be three different types of jets according to their constituents.

3.3.3. Calorimeter Jets

The jets which are reconstructed by using only the calorimeter towers are called "calorimeter jets". Calorimeter towers provide energy and location information. In CMS, the calorimeter towers are one or more hadronic and geometrically corresponding electromagnetic calorimeter cells. Towers will be included for jet clustering if only they carry a transverse energy, E_T, above a certain threshold. This threshold will depend on the geometrical location of the towers.

3.3.4. Calorimeter Jet-Plus-Tracks

The tracks reconstructed in the tracker may be used to improve the momentum measurement of the calorimeter jets. The tracks will be associated with jets if the jet axis and the tracks match with a certain precision in $\eta - \phi$ space. The momentum of the tracks will be added to the energy of the related calorimeter jet. But the direction of the jet axis will not be affected by the tracks. In other words the direction of the jets will remain unchanged.

3.3.5. Particle Flow Jets

Particles are individually reconstructed objects with tracks if they carry charge. Particle reconstruction may include information from every sub-system of the CMS detector depending on the type of the particle. *Particle Flow* algorithm uses particles as input objects to find jets. *Particle Flow* (PF) jets are clustered from individually reconstructed particles. The CMS detector has a very high performance silicon-based tracker which improves the precision of tracks and momentum measurements for charged particles. PF jets utilize this advantage for better momentum measurement.

3.3.6. Jet Energy Correction

Energy measurement of jets is quite difficult due to the nature of jets. They could include many number of charged and/or uncharged particles. Some portion of

their energy might not be detected or their energy may be overestimated because of the imperfection of detectors. Therefore energy corrections will be applied to reconstructed jets and will be called *corrected* jets.

In CMS there are three different energy corrections applied to jets. First one is the *offset correction*. This correction intends to subtract the fake contributions to jet energy measurement mostly coming from electronic noise and from other proton-proton interactions *pile-up* effect. The second one is the *relative correction* which aims to equalize the detector energy response to jets as a function of pseudorapidity. This correction uses dijet balance method where there are two back-to-back jets with the same energies. The third correction is called *absolute correction*. This correction is determined by using some special decays like $\gamma + jet$, $Z \rightarrow e^+e^- + jet$, and $Z \rightarrow \mu^+\mu - + jet$. In those decays the jet and the other particles will be back-to-back with the same total momentum. It is well known that the CMS detector has much better momentum measurement for leptons and photons compared to that for hadrons. Therefore the jet energy scale will be corrected by measurement of these particles in the decays.

3.4. Missing Energy Reconstruction

The particles which are not detectable by detectors create missing energy [16]. Neutrinos and muons are the known SM particles which can escape detectors without detection. Muons can be detected and their energy can be determined by measuring the curvature of their tracks under magnetic field. However, neutrinos could not be detected since they do not interact with the detector material. Therefore energy carried by neutrinos cannot be measured directly. But it is possible to estimate it by summing all the energies measured in the detector. If the initial momentum is zero then the total momentum of all the final particles should be zero, thus a possible imbalance in the final state could be the indication of missing energy caused by an undetectable neutrino. Not only neutrinos but also some undetectable and stable particles predicted by the theories beyond the SM could cause these missing energies. In that case, missing energy could be considered as an important signal for new physics searches. Especially

experiments in the large hadron collider, CMS and ATLAS, have special effort on missing energy measurement.

The CMS detector has pseudorapidity coverage up to $\eta = 5$. However, the particles traveling very close to the beam line carry large longitudinal momentum and will escape the detector without any detection. Because of this fact it is not possible to measure the missing energy in the longitudinal direction. On the other hand, the CMS detector has full ϕ coverage in transverse plane and its volume is filled with dense detector material. Therefore all the particles will be detected except those that do not interact with the detector material. Another fact is that the particles escaping the CMS detector in very forward region $\eta > 5$ will carry very low transverse momentum;

$$p_T \leq 0.0013 \times p \tag{3.6}$$

where $0.0013 = cosh(\eta = 5)$. Therefore it is much more convenient to measure missing energies in transverse plane than other. As a result it will be called missing transverse energy (MET) and will be calculated by;

$$\begin{aligned} \vec{E}_T^{miss} &= -\sum_n (E_n \sin\theta_n \cos\phi_n \hat{x} + E_n \sin\theta_n \sin\phi_n \hat{y}) \\ &= E_x^{miss}\hat{x} + E_y^{miss}\hat{y} \end{aligned} \tag{3.7}$$

where n corresponds to all calorimeter towers, $\hat{x}$ and $\hat{y}$ are the unit vectors of the transverse plane perpendicular to the beam direction along $\hat{k}$, θ and ϕ are the longitudinal and azimuthal angles, respectively. MET, defined by this equation, is a vector quantity. Most of the time its magnitude is also referred as "MET" which may be confusing.

There is also another quantity called scalar transverse energy ($\sum$ET) which is the scalar sum of the energies in transverse plane;

$$\sum E_T = \sum_n E_n sin\theta_n, \tag{3.8}$$

where n corresponds to all calorimeter towers and θ is the longitudinal angle.

In CMS there are two types of MET; calorimeter missing transverse energy (CALOMET) and particle flow missing transverse energy (PFMET). CALOMET considers only energy depositions in calorimeter towers while PFMET uses also the track information from the tracker, related to the energy depositions in the calorimeter towers. Therefore PFMET has relatively better energy resolution. MET is also calculated without towers from the hadron outer and the hadron forward calorimeters and named as METnoHO and METnoHF, respectively.

Missing energy measurement is very sensitive to instrumental effects. Any noisy or dead calorimeter cell could create fake imbalance, thus fake missing energy. It requires a very detailed understanding of the detector to remove these fake contributions to missing energy measurement. Another important reason concerning the fake missing energy comes from muons which leave a fraction but not all of their total energy in the detector. Raw MET is needed to be corrected regarding muons.

4. HYBRID PHOTODIODES CHARGE SPECTRUM

4.1. Introduction

The following analysis presents the full charge spectrum of the Hybrid Photo Diodes (HPD) used in the readout of the Hadron Barrel (HB) and Hadron Endcap (HE) subdetectors when operated in the full magnetic field [17]. The data used here were taken during the 2008 CRAFT data taking period. The full charge spectrum can be obtained from the events taken in the global runs that do not have real energy in the hadron calorimeter ("pedestal events"). Most of the triggers used during these runs (besides the HCAL noise triggers) provide pedestal events.

Specifically, data were collected using cosmic triggers based on muon triggers and streamed offline to the "cosmic data stream". For these events, some of the HCAL towers do contain real energy from the muons that caused the trigger. During CRAFT data-taking, 10 time slices (each integrating over 25 ns) of charge information were read out per trigger. The calorimeter is timed so that most of the energy from the muon should occur in the 4th time slice. Therefore it is expected that the early time slices should be mostly free of real energy and can be used to measure the HCAL noise rate.

4.2. Hybrid Photodiode (HPD)

A Hybrid photodiode [18] is composed of a high-voltage applied vacuum tube with a photocathode on one side and a plane semiconductor PIN diode array at low-bias voltage on the other side. Electrons freed from the photocathode by photons are accelerated inside the vacuum tube via the electro-static field produced by the applied high voltage ($\sim$ 10 kV). These accelerated electrons are stopped by hitting the silicon PIN diodes and produce electron-hole pairs, thus a current pulse. The Hybrid photodiodes can operate at 1000 to 5000 gain which depends on the applied high-voltage linearly.

The choice of multi-channel hybrid photodiode (HPD) [19] in the CMS is driven by the operating environment at 4T magnetic field and by an affordable cost. The sub-detectors of the hadronic calorimeter, HB, HE, and the HO use HPDs as photodetectors. Each of these HPDs have 19 read-out channels and 18 of them are assigned to channels of the calorimeters. These channels form a silicon PIN diode array as shown in Figure 4.1.

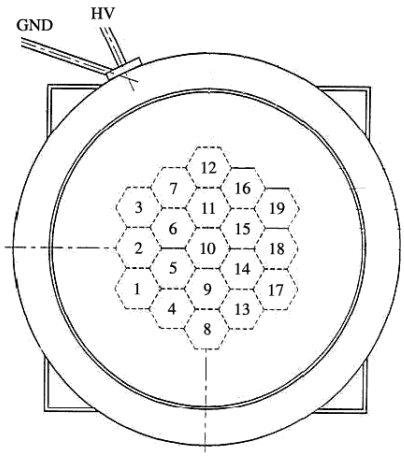

Figure 4.1. A schematic drawing of a HPD showing the pixel array.

The fiber optic cables deliver the light coming from the channels (scintillators) to the window of the HPD. The window is used to map the cables into tower bundles and each bundle goes into a pixel which the tower is assigned to. The bundles could have between 2 to 19 1-mm thick fibers.

The photons free electrons from the photocathode surface. These electrons are accelerated under HV $\sim$ 8 kV in the vacuum tube towards the silicon PIN diode array. Electrons hitting the silicon PIN diode produce electron-hole pairs and a current pulse that is read out by the front-end electronics of the HCAL. The HPDs for the HCAL are customized for the CMS operating conditions.

The large magnetic field is the major factor forcing the customization of the HPDs. The magnetic force causes the photo-electrons to shift from its straight path due to the electro-static field acceleration, thus the electron may hit another pixel and cause a cross-talk effect. This shift is directly related to the travel distance under

the influence of the magnetic field, in other words the acceleration gap. The second order effect caused by the reflection from the dead surface may even increase this travel distance, hence the cross-talk effect. On the other hand too short a gap may cause a high-voltage breakdown. The studies [20] showed that a length of 3.3 mm acceleration gap causes 290 μm shift for a 5^o misalignment to the magnetic field as well as preventing any risk of high voltage breakdown. Therefore the pixels and fiber optic cable bundles are adjusted with 400 μm separation to prevent cross-talk effect.

The HPD uses T-type silicon photodiodes with trapezoidal output pulse. The width of the pulse, determined by the drift time of the charge carriers, is needed to be shortened for reducing the pileup effects for the LHC physics. This goal is accomplished with a thinner silicon diode, 200 μm instead of 300 μm. Hence the pulse width of the customized HPD is reduced to $\sim$ 25 ns, which is the LHC bunch crossing time.

Also the over all geometry and instrumental structure of the HPD for the CMS HCAL are customized according to the operating conditions. The picture in Figure 4.2 shows the cross sectional view of an HPD used in the HCAL.

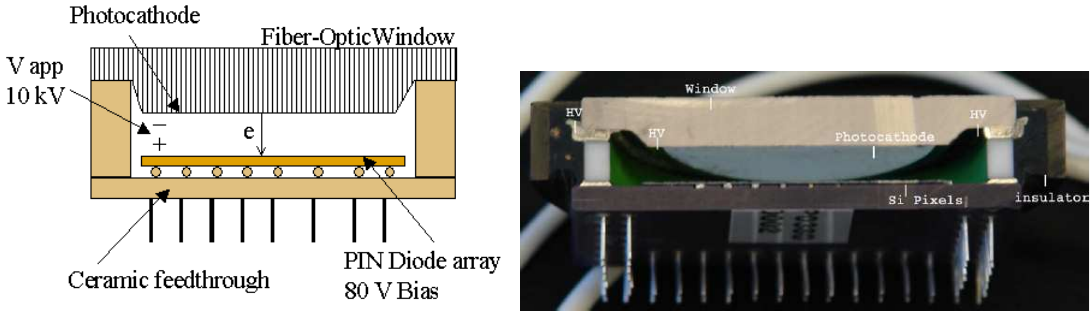

(a) Drawing (b) Picture

Figure 4.2. The HPD cross sectional view.

The HPDs are tested together with photo multiplier tubes (PMT) and avalanche photodiodes (APD) for comparison in a dedicated test beam at CERN in 1996 [21]. The HPDs showed consistent results compared to the APDs for electrons. For muon beams, the HPD showed a better signal-to-noise ratio despite their lower quantum efficiency. However high event rate in the LHC and limitations on the size of the fiber bundles will prevent clean signal detection with the HPDs. The energy resolution of

the HPDs were the worst compared to the APD and the PMT resolution. This was mostly caused by the shower leakage due to the limited number of HPD channels.

4.3. Structure of HPD Noise

The HPD noise spectrum contains spurious signals from thermal emission, ion feedback and discharge. The noise signals produced by these effects can be differentiated by the size of the produced charge.

Thermal emission is caused by the electrons which are freed from the photocathode surface by thermal fluctuations. Thermal emission produces signals in the pedestal region, generally less than 0.5 GeV per event per time slice (25 ns).

The vacuum inside the HPDs is not perfect and includes some gas molecules. Occasionally these gas molecules are ionized by the electrons released from the photo cathode. These ions are accelerated towards the photocathode due to the electric field generated by the high-voltage, and they may remove some additional electrons from the surface of the photo-cathode. These electrons can ionize more gas molecules and so on. This effect is called "ion feedback", and it occurs at a rate of 10^{-6} per time slice (25 ns).

The total charge produced by this effect is proportional to the energy of the particles hitting the HPD photo cathode, since "ion feedback" is produced by the electrons released from the photo cathode. The energy equivalent of the charge produced per time slice (25 ns) produced by this effect ranges (roughly) from 1 GeV to 5 GeV.

The high voltage setting and the magnetic field can affect the amount of ion feedback. Significant enhancement of the ion feedback can occur at higher voltage and magnetic fields, and is called *discharge*. The rate of discharge varies substantially from HPD to HPD, as it depends on characteristics of HPDs, like material properties, defects, etc., that vary. This effect can give a relatively large signal per event, mostly greater than 10 GeV integrated over the duration of the pulse, with a discharge that

can last for several time slices.

An RBX contains four HPDs serving four adjacent phi slices and an HPD serves all the channels in a ϕ slice. Because of this structure there is often anomalous energy in adjacent ϕ and η channels in an event. Figure 4.3 shows a typical event with HPD noise in a phi slice and Figure 4.4 shows a typical event with anomalous energy in the four phi slices associated to one RBX.

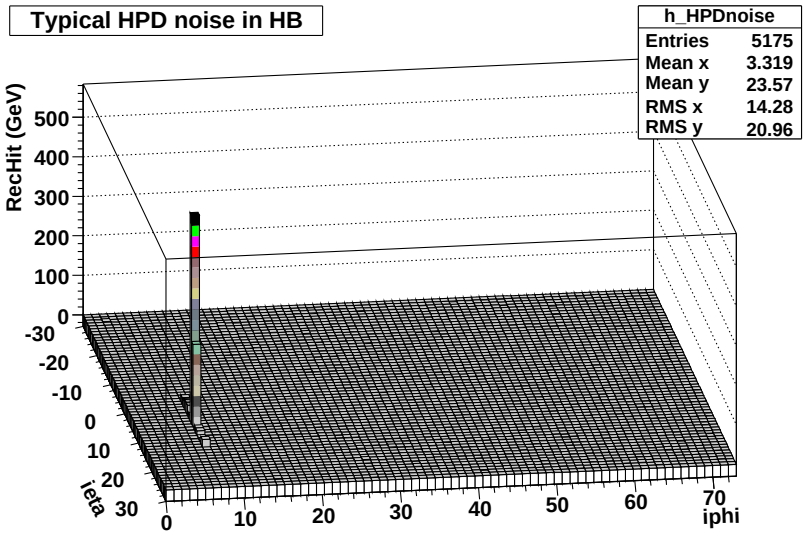

Figure 4.3. Pattern of energies in a typical HPD discharge event.

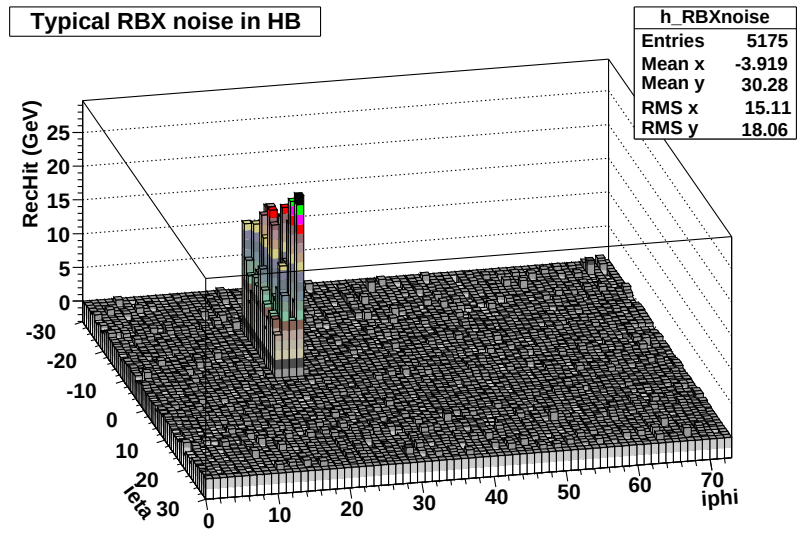

Figure 4.4. Energy patterns in an event involving discharge of all HPD's in an RBX.

4.4. Method

Data from the 2008 CRAFT runs were used. Signals from real particles during data taking will produce a signal that is mostly confined to two time buckets [22]. For our noise measurement, the sum of the linearized QIE output for the first two, three and four time slices in each event for all HPD channels in the HB and HE are used. Signals from real muons should predominantly populate the 5^{th}, 6^{th}, and 7^{th} time slices.

As the spurious signals with large integrated charge that are most likely to interfere with rare physics signals, such as searches for supersymmetry and large extra dimensions, a very large number of events are needed to obtain the noise rate. Since the ratio of ion feedback to pedestal is in the order of 10^{-6}, one needs to analyze at least millions of events to be able to study the ion feedback region reliably. Two data samples are used to obtain this rate, 15 million events taken with muon-based cosmic triggers and 14 million events taken with random triggers.

The "random triggers" sample appears not to have been truely random; this sample seems to be contaminated by events that were actually taken on calorimeter triggers. If so, the rate obtained from this sample represents an upper limit on the noise rate.

All the plots in this analysis are normalized to the larger sample size (15 million events) for ease of comparison.

Figure 4.5 below shows the average charge in ADC counts versus time slice for *Cosmic* data for more than 10 M events and for all channels in the HB and HE. There is a clear muon signal in the 4^{th} and 5^{th} time slice. However, there is also a clear muon contamination in the 3^{rd} time slice. This is probably because it is difficult to adjust the timing of the calorimeter correctly for these cosmic ray events. It could also be due to showers of cosmic muons that arrive at similar times.

Event dumps can be used to confirm the muon contamination after the 2^{nd} time

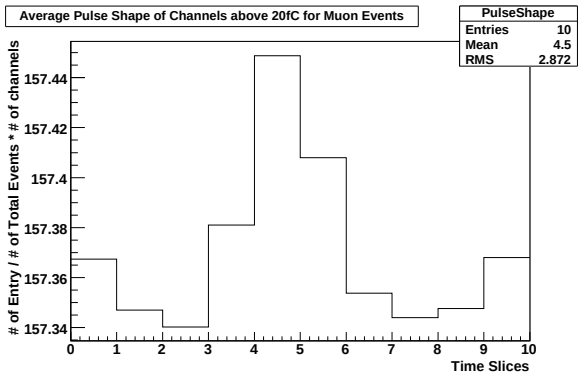

Figure 4.5. Average integrated charge in ADC counts versus time slice number for Cosmic data.

slice. Table 4.1 shows the ADC counts for each time slice from an event from cosmic data stream of the run 68288.

Table 4.1. ADC counts versus time slice number from an event dump from the cosmic data stream of the run 68288.

Timeslices (25 ns)	0	1	2	3	4	5	6	7	8	9
ADC counts (fC) (linearized)	2	22	188	46	12	4	3	4	2	3
	2	4	36	18	5	3	1	3	3	4
	3	4	5	12	5	4	3	3	3	2
	3	4	20	10	5	3	2	3	4	1
	3	4	10	5	4	3	4	3	4	4

One can see that the peak of the signal is in the third time slice and the second time slice also has some part of the signal.

For the rest of this analysis, only the first two time slices are considered in our sum.

4.5. Analysis

Figure 4.6 shows the full charge spectrum of HPDs in the HB- (hadron barrel covering minus η), which is similar to the other HPDs in the HB+, HE- and HE+, summed over two time slices.

In this plot, the horizontal axis is the nominal charge in fC and the vertical axis is rate, calculated assuming the events are random samplings of the integrated charge in a 50 ns interval, and so the total time interval, used in the rate calculations, is the number of events times 50 ns. The pedestal value (10 fC for four time slices) is not subtracted. The average pedestal value for each time slice is 2.5 fC, in agreement with the expected value. The average conversion from ADC counts to energy is 0.16 fC/GeV.

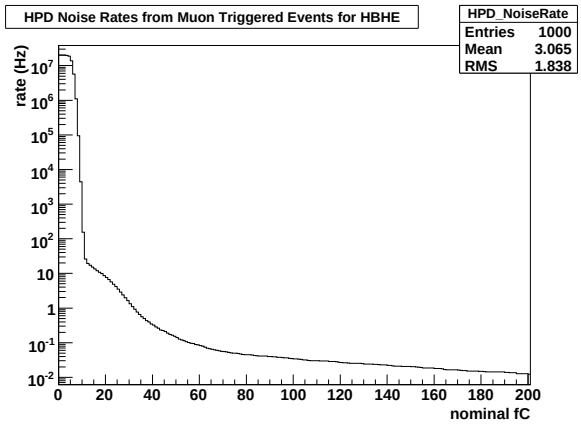

Figure 4.6. Rate versus charge integrated over 2 time slices in ADC counts for Cosmic data. The pedestal of 2.5 fC was not subtracted. The average conversion from adc counts to GeV is 0.16 fC/GeV

The noise rate for an energy threshold of 10 GeV (67.5 fC) obtained using the first two time slices times the total number of HB/HE HPD's (5184) is very close to the noise rate determined from the HCAL jet trigger (100 Hz) with the same threshold.

Since there could still be some muon contamination even in the first two slices, the RandomTriggers data stream is also analyzed (the "MinimumBias" stream was not minimum bias at all, but instead contained muon-triggered events). The integrated rate

plots are shown in Figure 4.7.

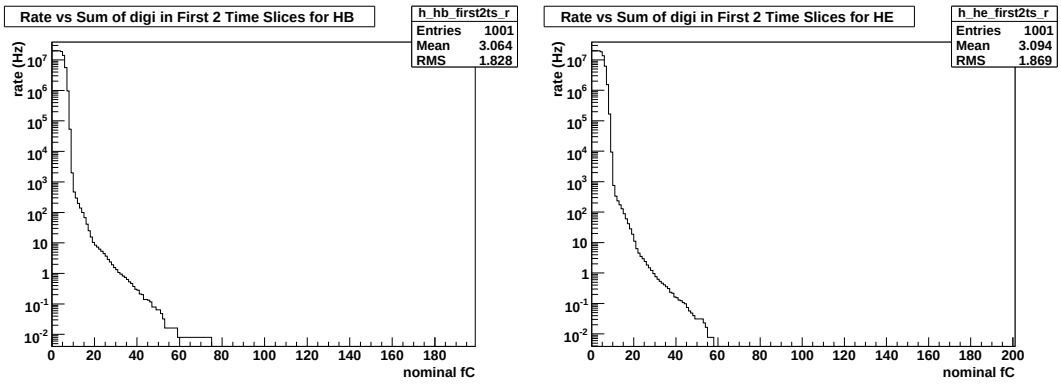

(a) HB (b) HE

Figure 4.7. Rate from an HB and HE HPD obtained with the first two time slices.

The plot in Figure 4.8(a) shows the comparison between the *Cosmic* (Red) and *RandomTriggers* (Green) spectra obtained by summing over the first two time slices. In this plot there is no shift between the two spectra since the pedestal values are the same for both. The significant result from this plot is that using the first two time slices gives very similar HPD charge spectra in both *Cosmic* and *RandomTriggers* data. Hence to obtain the spectrum from cosmic data it is better to use the first two time slices. But if one looks at the plot closely (Figure 4.8(b)), it can be seen that there are some additional signals in the higher region for the *Cosmic* data.

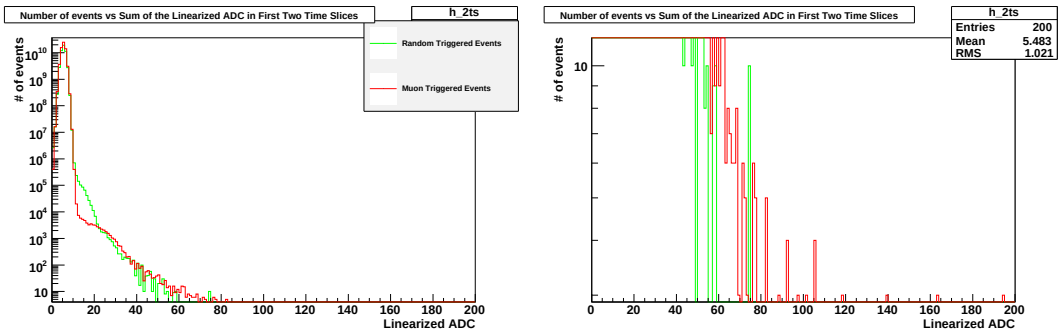

(a) Full range (b) Y-axis zoomed

Figure 4.8. Noise spectrum obtained by summing over the first two time slices with the Random Triggers and with the Muon Triggers (Cosmic).

As mentioned before, this may come from picking up the part of the real signal. But the rate is very low so that one can ignore it and use both spectra.

Figure 4.9 shows the noise rate for detector η and ϕ for calorimeter cells with $E_T > 5$ GeV. The depths are not shown separately. For this plot 10k events of run 68288 are used with calorimeter triggered data set. It can be seen that a small number of channels are noisier than the rest of the cells.

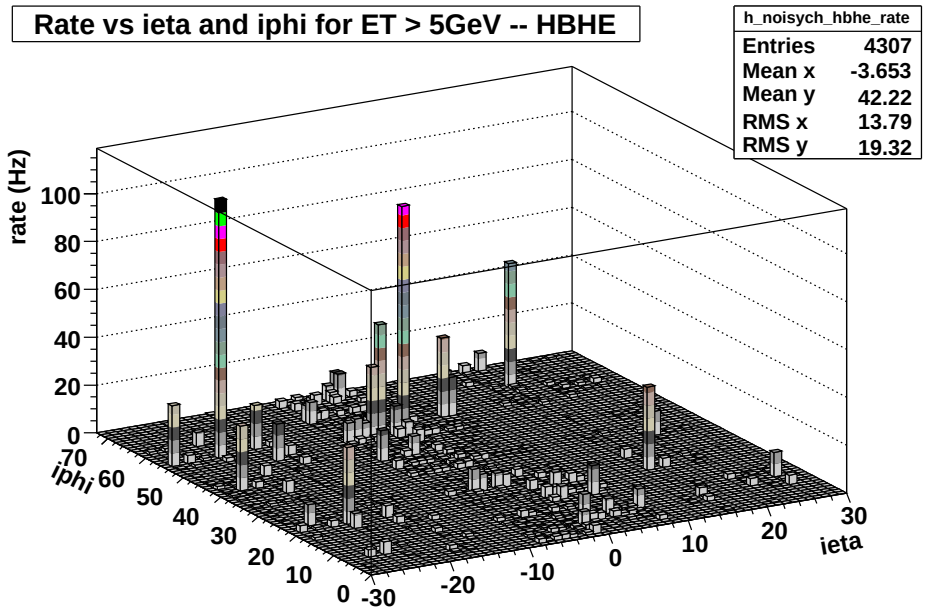

Figure 4.9. Noise rate vs. iη and iϕ above 5 GeV transverse energy threshold on calorimeter cells.

4.6. Concluding Remarks

The charge spectra of the HPDs in the barrel and endcap detectors have been obtained. The spectra showed that using the first two time slices is better and the results are more reliable in terms of noise rates in large scales. The noise calculations from HCAL jet trigger and from these spectra have a small difference which is understood. Hence both rate calculations are in reasonable agreement.

5. ELECTRON EFFICIENCY AS A FUNCTION OF JET MULTIPLICITY

5.1. Introduction

Efficiency measurement in particle detection plays an important role in experimental high energy physics. Almost all the physics analyzsis depend on detecting the particles; leptons and/or jets. In a real detector, in presence of background, this detection would not give the exact number of produced particles since we cannot reconstruct every single particle exactly as it is. Hence we must determine the electron efficiency, the ratio of the particles we can detect to the particles actually produced.

In this analysis we studied the efficiency measurement of electrons as a function of jet multiplicity. We need to measure the electron efficiency when there are also jets in the event because for many experimental signatures with electrons in the final state we also expect jets. For example, Standard Model $W/Z(\rightarrow e) + jets$, top quark decays to electron channel, SUSY decays to electron channels..

There are two types of backgrounds in electron reconstruction; background due to instrumental effects and physics background. The former mostly caused by the imperfections in the instruments, such as electronic noise which may be reconstructed as energy deposition. The Compact Muon Solenoid (CMS) has a good Electromagnetic Calorimeter (ECAL) [1] which reduces the instrumental effects in electron reconstruction. Still there may be a small background contribution from instrumental effects. The physics background in electron reconstruction is caused by the real particles that may act like electron by depositing energy in ECAL, e.g., photons, and jets.

In CMS, electron reconstruction [9] starts with Super Clusters (SC) in ECAL. Super Clusters are the reconstructed 5×5 ECAL crystals containing energy deposited by particles which may be electrons as well as other particles and jets. Then the tracks, reconstructed by a Gaussian Sum Filter (GSF) in CMS tracker, matched to some of the

SCs to form the GSF electrons. The next step is the isolation of the electron candidates followed by some electron ID requirements.

Therefore the electron efficiency [23] could be defined at each individual step in reconstruction as well as "total" efficiency which is the number of SCs matched to the ID requirements by passing all the sub-steps of reconstruction. Additionally, these electrons need to be triggered by the HLT and Level-1 triggering system. There is an efficiency associated with this also.

We determined the electron efficiency in terms of the jet related quantities in the event, such as number of jets and distance between jets and electrons. These jet related quantities are expected to affect electron efficiency. Hence it is important to study these effects in detail to have a better understanding of the electron reconstruction efficiency in the presence of jets.

5.2. Control Samples

The official Spring10 $Z(\rightarrow ee)+Jets$ MC samples are used for the analysis. Table 5.1 shows the MC samples with p_T bin, number of events, and theoretical cross sections. The samples named in DBS as "/ZeeJet_PtXtoY/Spring10-START3X_V26_S09-v1/GEN-SIM-RECO" where X and Y represent the p_T bin intervals.

Table 5.1. Cross sections and the number of events in MC samples for $\sqrt{s} = 7$ TeV. p_T bins for each sample are shown separately.

	Z($\rightarrow e^+e^-$)+Jets									
	0-15	15-20	20-30	30-50	50-80	80-120	120-170	170-230	230-300	300-Inf
$\sigma(pb)$	4434	145	139	84	32	9.9	2.8	0.72	0.19	0.07
# of events	214330	209740	175590	189024	118383	150600	127820	153000	110720	113675

5.3. Data-Driven *Tag&Probe* Technique To Measure The Electron Efficiency

In this analyses we used the *tag&probe* method [24] to calculate the electron efficiencies. This method uses the Z mass constraint from the dielectron pair to determine the efficiency. The "tag" is the electron passing a set of tight selection criteria defined by user. The "probe" is also an electron which is required to pass some analysis level selection criteria. Once the tag and probe are paired the invariant mass M_{ee} is required to be in the region of M_Z mass window. The efficiency could be defined as the ratio of the probes passing the selection criteria to all probes,

$$\epsilon = \frac{N_{TP_p}}{N_{TP_p} + N_{TP_f}}, \tag{5.1}$$

where N_{TP_p} is the number of *tag&probe* pairs which the probes pass certain criteria, while N_{TP_f} is the number of the tag& probe pairs which the probes fail certain criteria. Note that here "certain criteria" do not refer to the selection criteria of tag or probe. It refers to the criteria which one wants to calculate the electron efficiency for. The details of the tag and probe selections will be given in sections 5.4.1 and 5.4.2, respectively.

If a probe also satisfies the tag selection, then there will be two tags and hence two probes. Therefore there will be double counting of *tag& probe* pairs in such events. If we include these events then the efficiency equation in 5.1 should be modified as:

$$\epsilon = \frac{2n_{TT} + n_{TP_p}}{2n_{TT} + n_{TP_p} + n_{TP_f}}. \tag{5.2}$$

The term n_{TT} is the number of *tag&probe* pairs which the probes pass also the tag selection. The term n_{TP_p} is the number of *tag&probe* pairs which probes pass a certain criteria but could not pass tag selection. The term n_{TP_f} is the number of *tag&probe* pairs which the probes fail for a certain criteria and these probes do not pass the tag selection. Another possibility is that there might be more than one probe in some events. These events will be rejected because such events will bias the efficiency

calculation.

5.3.1. Description of the Software

There is a tool available in the CMSSW framework called Tag & Probe software [25] which enables the CMS users to measure the lepton efficiencies by using the method described above.

There are two steps to measure the efficiency. The first step is to produce an output file with Root-tree which contains information of tag, probe, passing probe, and the variables added by user. This can be done by running the configuration file named "$Electron\_TagProbeTreeProducer\_cfg.py$". It is possible to define the properties of the objects to be stored by modifying this file. The next step is to run "$testTagProbeFitTreeAnalyzer\_Zee.py$" on the output file produced by step one. It will calculate the efficiencies by using three different techniques to subtract the background contamination in the probe sample since it effects the efficiency measurement. These techniques are Side Band Subtraction, Shape based Background Subtraction, and MC truth by using generated level information. The results for each technique is stored separately in the output file. The results are stored as unbinned "RooDataSet" format in ROOT framework and also 1-D efficiency plots saved as "RooPlot" objects. Therefore it is possible to retrieve efficiency plots directly or to make your own.

5.4. Electron Efficiency

The analysis of electron efficiency is performed according to a well-defined factorized sequence of sub-efficiency measurement. Even if the "total" efficiency is the most interested one by users it is also very important to know how the efficiency changes and is affected by the selection process of the probes leading to the tag electron, thus a better understanding of the efficiency. Also the uncertainty in the efficiency measurement improves by separating reconstruction efficiency from ID and triggering efficiencies. Below we will describe the factorized electron efficiency sequence with details used in this analysis.

5.4.1. Tag Selection

Tag should be a reasonably well-reconstructed electron. Following selection criteria are used for tag;

- Transverse energy above a threshold value, $E_T > 20GeV$
- Absolute eta, $|\eta| < 1.44$ or $1.56 < |\eta| < 2.5$.
- Isolation requirements defined in section 5.4.4.
- ID requirements defined in section 5.4.5.
- HLT triggering defined in section 5.4.6.

The electrons passing all those requirements will be called "tag".

5.4.2. Probe Selection

Probe collection is made among SCs in ECAL. Requirements for SCs to be selected as probe electrons are,

- Transverse energy above threshold, $E_T > 20GeV$
- Absolute eta, $|\eta| < 1.44$ or $1.56 < |\eta| < 2.5$
- Not to have nearby jets closer than, $\Delta R < 0.1$.

The SC which satisfies these cuts are named as "goodSuperClustersClean" and accepted as probes.

5.4.3. Reconstruction Efficiency

The next step in the process is passing "GsfElectron" selection criteria. It is slightly different for a probe electron to pass this selection criteria since GSF electron collection is already available in reconstructed data. Therefore the probe selection criteria listed above except for the last one will be also applied to GSF electrons. Then every probe electron which is close to those GSF electrons with $\Delta R < 0.3$ will

be considered as probes passed GSF electron requirements. The efficiency for this selection will be called as *reconstruction* or *GSF electron*, $SC \rightarrow GSF$, *efficiency* and might be represented with

$$\epsilon_{GSF} = \frac{N_{T(SC \rightarrow GSF)}}{N_{T(SC)}}, \tag{5.3}$$

where $N_{T(SC \rightarrow GSF)}$ is the number of probe electrons passing GSF electron selection and $N_{T(SC)}$ is the number of all probes.

5.4.4. Electron Isolation Efficiency

A good electron candidate is needed to be isolated which makes the next step the isolation selection. The isolation criteria depends on the location of the candidate and could be in barrel or endcap. Table 5.2 shows the cuts for isolation.

Table 5.2. Relative isolation requirements for GSF electrons

Relative Isolation	Barrel	Endcap
$(\sum_{\Delta R<0.3}(E_{T(ECAL)}-1)+\sum_{\Delta R<0.3}E_{T(HCAL)}\sum_{\Delta R<0.3}P_{T(tracker)})/P_T$	0.15	(no cut)
$(\sum_{\Delta R<0.3}E_T(ECAL)+\sum_{\Delta R<0.3}E_T(HCAL)\sum_{\Delta R<0.3}E_T(tracker))/P_T$	(no cut)	0.1

The isolation efficiency then can be shown as

$$\epsilon_{iso} = \frac{N_{T(Gsf \rightarrow Iso)}}{N_{T(Gsf)}}, \tag{5.4}$$

where $N_{T(Gsf)}$ is the total number of GSF electrons while $N_{T(Gsf \rightarrow Iso)}$ is the number of isolated GSF electrons which passed isolation selection criteria.

5.4.5. Electron ID Efficiency

After making sure we have isolated GSF electrons, next step is to apply a set of cuts which are called ElectronID selection criteria. It includes the quantities:

- The shower shape of energy deposition in $i\eta$, $\sigma_{i\eta i\eta}$.
- η difference between SC and track at vertex, $\Delta\eta_{SCtoTrack}$.
- ϕ difference between SC and track at vertex, $\Delta\phi_{SCtoTrack}$.
- The ratio of energy deposited in the hadronic calorimeter to the electromagnetic calorimeter, E_{HAD}/E_{EM}.

The cut values are given in Table 5.3. The efficiency of the ID selection is given by

$$\epsilon_{ID} = \frac{N_{T(Iso \to ID)}}{N_{T(Iso)}}, \tag{5.5}$$

where $N_{T(Iso \to ID)}$ is the number of Isolated GSF electrons that pass the ID selection criteria, $N_{T(Iso)}$ is the total number of isolated GSF electrons.

Table 5.3. The electron ID cut values

	Barrel	Endcap
E_{Had}/E_{EM}	0.5	0.07
$\sigma_{i\eta i\eta}$	0.01	0.03
$\Delta\eta_{SCtoTrack}$	0.007	0.01
$\Delta\phi_{SCtoTrack}$	0.8	0.7

5.4.6. Trigger Efficiency

The final selection is the trigger requirement. The ID electrons need to pass high level electron trigger, namely "$HLT\_Ele15\_SW\_LooseTrackIso\_L1R$". The HLT efficiency is then defined by

$$\epsilon_{HLT} = \frac{N_{T(Id \to HLT)}}{N_{T(Id)}}. \tag{5.6}$$

5.5. Jet Multiplicity

Before going into the details of electron efficiencies, it is important to understand the jet multiplicity of the sample and, of course, the description of the jet selection criteria used in this analysis, since we studied the electron efficiencies as a function of jets. We used "L2L3CorJetAK5Calo" corrected jets and applied the following kinematic cuts listed below.

- η requirement, $|\eta| < 2.6$.
- p_T requirement, $p_T > 20$ GeV.

As a final requirement for the jet selection, we removed jets with electrons ($\Delta R < 0.1$). This is required to remove the electrons from the jet collection and does not change the electron collection. The jets passing the selection criteria are used in determining the jet multiplicity of events as shown in Figure 5.1(a). No-jet and 1-jet events has the highest statistics, thus will be dominant in the electron efficiency measurement.

Note that zero-jet does not mean that the events do not have any jets. This is important because the jets failing our selection may still have effects on electron efficiencies, thus those efficiencies might be smaller compared to the efficiencies measured with MC samples that are produced without jets.

Distance between the electrons and jets is also important since it will affect the electron efficiency due to isolation. Because of this reason we need to understand the electron efficiency as a function of ΔR between the electrons and jets. Figure 5.1(b) shows the ΔR distribution between the selected electrons and jets. We will also measure the electron efficiencies as a function of $\Delta R_{eltojet}$ in this analysis.

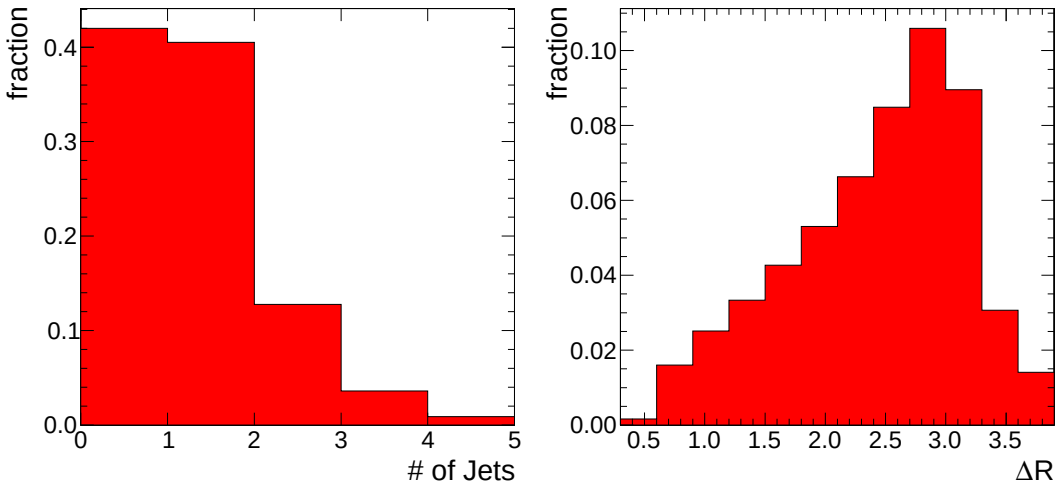

(a) # of jets (b) $\Delta R_{eltojet}$

Figure 5.1. Jet multiplicity and $\Delta R_{eltojet}$ between electrons and jets distributions of $Z(\rightarrow ee)$ + jets events.

5.6. Results of Efficiency Measurements

5.6.1. Electron Reconstruction Efficiency, $SC \rightarrow GSF$

The GSF electron efficiencies as a function of probe p_T and η for 0-, 1-, 2-, 3-, and 4-jet events are shown in Figure 5.2. The difference in efficiencies according to the number of jets in the event can be easily seen. These differences vary according to η and p_T of the SCs.

The GSF efficiencies are also determined as a function of the distance between electrons and jets, $\Delta R_{eltojet}$, as shown in Figures 5.3(a) and 5.3(b) as a function of probe η and p_T, respectively. The GSF efficiencies also can be seen for all events as a function of probe η and p_T in Figure 5.4.

The efficiencies for $SC \rightarrow GSF$ vary between 85-99.9% depending on the η location and p_T of the probes. For the same η or p_T bins it is possible to see more than 10% difference in GSF efficiencies depending on the jet multiplicity or $\Delta R_{eltojet}$ of the events.

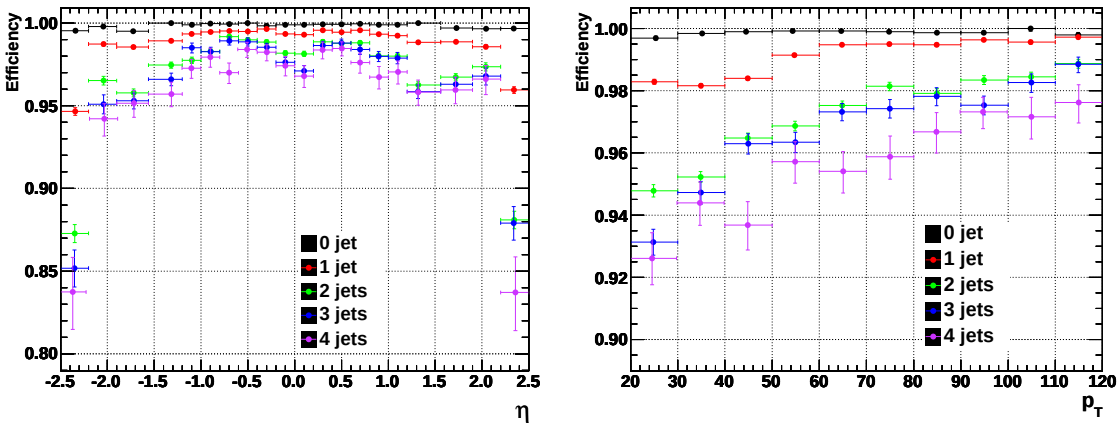

(a) (b)

Figure 5.2. GSF electron efficiencies for different jet multiplicities as a function of η and p_T of the probes.

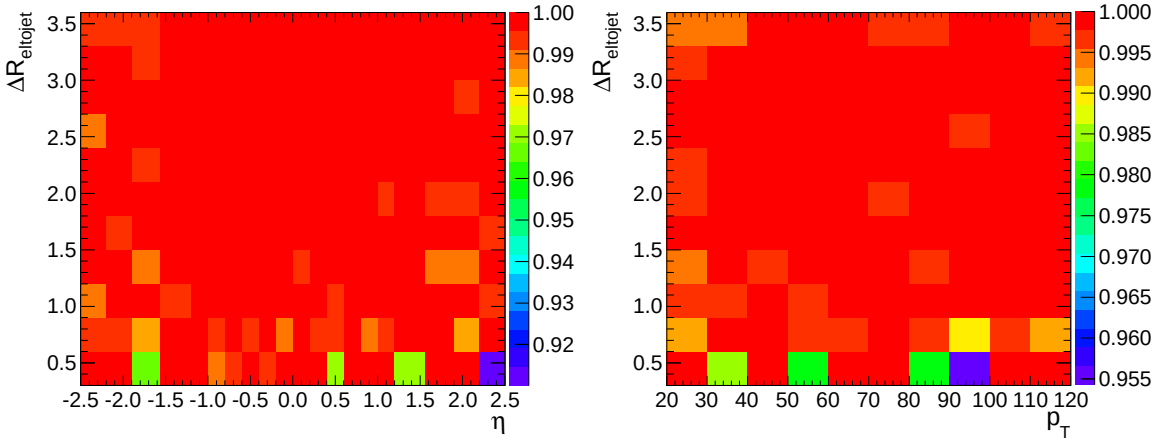

(a) (b)

Figure 5.3. GSF electron efficiencies as a function of the distance between electrons and jets.

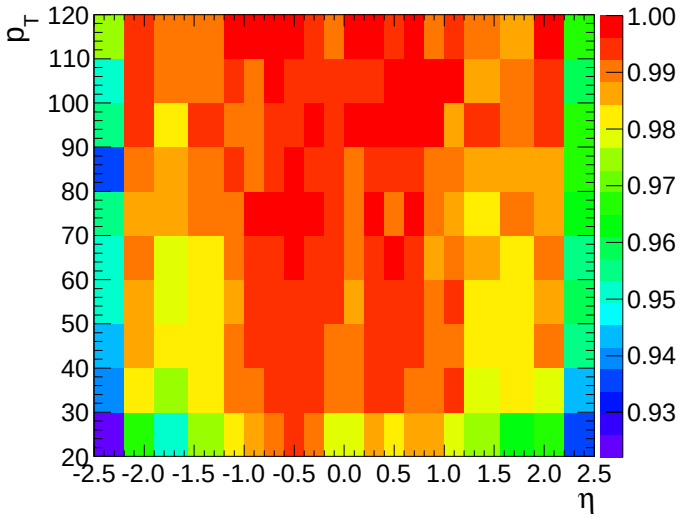

Figure 5.4. GSF efficiency as a function of p_T vs η.

5.6.2. Isolation Efficiency, $GSF \rightarrow Iso$

The isolation efficiencies as a function of probe p_T and η for 0-, 1-, 2-, 3-, and 4-jet events are shown in Figure 5.5. The difference in efficiencies according to the number of jets in the event can be easily seen. These differences vary according to η and p_T of the SCs.

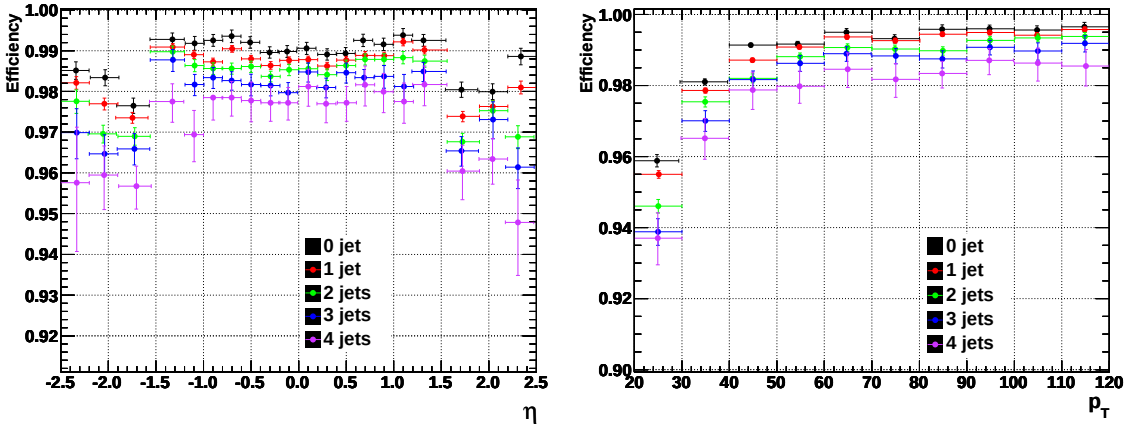

(a) (b)

Figure 5.5. Isolation efficiencies for different jet multiplicities as a function of η and p_T of the probes.

The isolation efficiencies are also determined as a function of the distance between electrons and jets, $\Delta R_{eltojet}$, as shown in Figures 5.6(a) and 5.6(b) as a function of probe

η and p_T, respectively. The isolation efficiencies also can be seen for all events as a function of probe η and p_T in Figure 5.7.

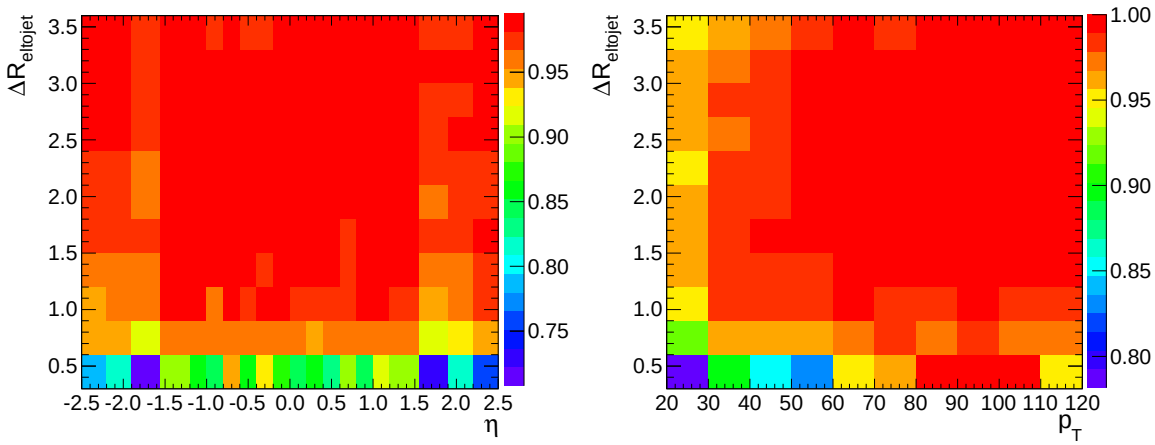

(a) (b)

Figure 5.6. Isolation efficiencies as a function of the distance between electrons and jets.

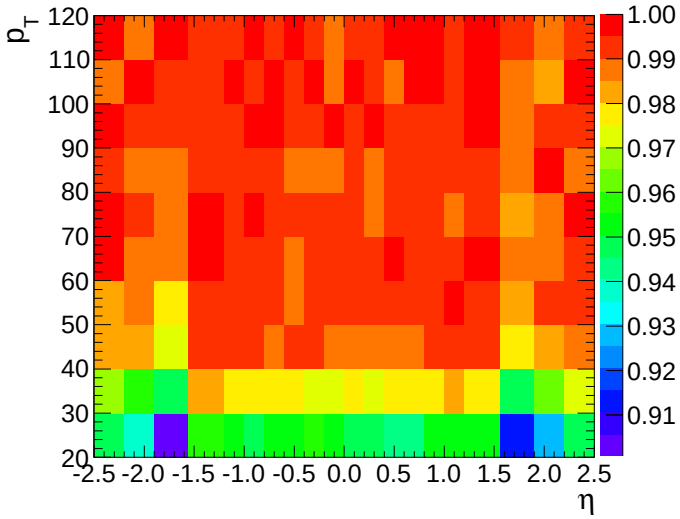

Figure 5.7. Isolation efficiency as a function of p_T vs η

The efficiencies for $GSF \rightarrow Iso$ vary between 94-99% depending on the η location and p_T of the probes. For the same η or p_T bins it is possible to see up to 5% difference in isolation efficiencies depending on the jet multiplicity or $\Delta R_{eltojet}$ of the events.

5.6.3. ID Efficiency, $Iso \rightarrow Id$

The ID efficiencies as a function of probe p_T and η for 0-, 1-, 2-, 3-, and 4-jet events are shown in Figure 5.8. The difference in efficiencies according to the number of jets in the event can be easily seen. These differences vary according to η and p_T of the SCs.

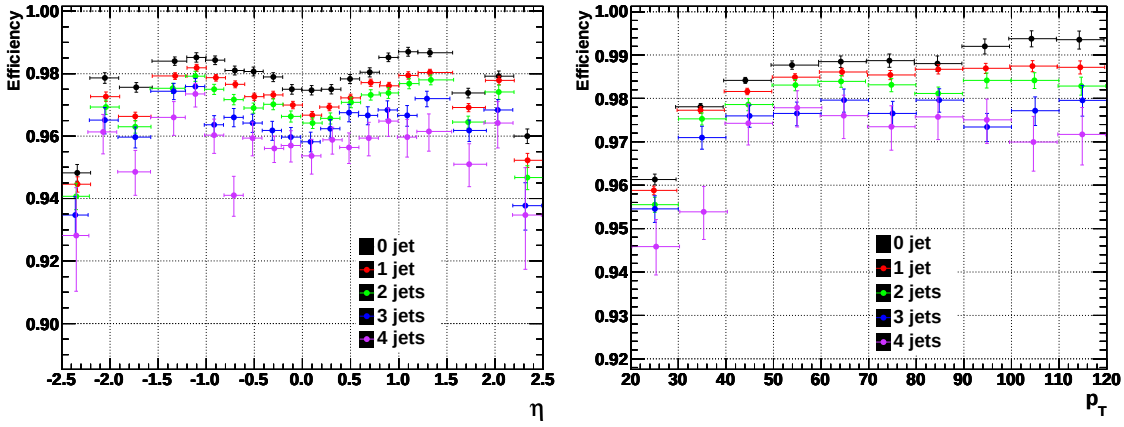

(a) (b)

Figure 5.8. ID efficiencies for different jet multiplicities as a function of η and p_T of the probes.

The ID efficiencies are also determined as a function of the distance between electrons and jets, $\Delta R_{eltojet}$, as shown in Figures 5.9(a) and 5.9(b) as a function of the probe η and p_T, respectively. The ID efficiencies also can be seen for all events as a function of probe η and p_T in Figure 5.10.

The efficiencies for $Iso \rightarrow Id$ vary between 93-99% depending on the η location and p_T of the probes. For the same η or p_T bins it is possible to see up to 3% difference in ID efficiencies depending on the jet multiplicity or $\Delta R_{eltojet}$ of the events.

5.6.4. HLT Efficiency, $Id \rightarrow HLT$

The HLT efficiencies as a function of probe p_T and η for 0-, 1-, 2-, 3-, and 4-jet events are shown in Figure 5.11. The difference in efficiencies according to the number of jets in the event can be easily seen. These differences vary according to η and p_T of

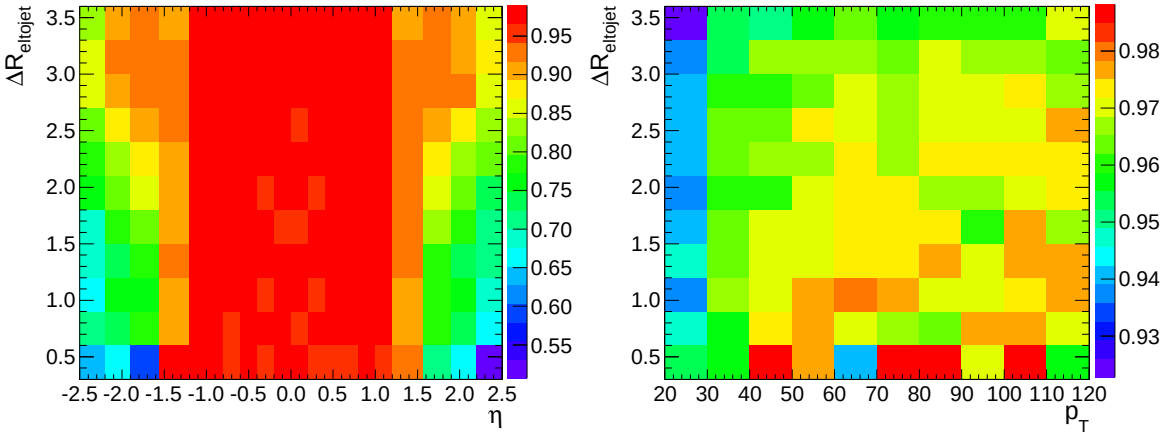

(a) (b)

Figure 5.9. ID efficiencies as a function of the distance between electrons and jets.

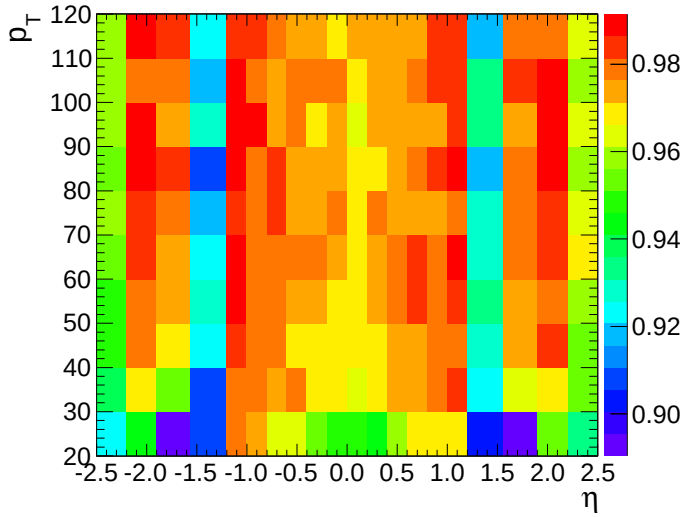

Figure 5.10. ID efficiency as a function of p_T vs η.

the SCs.

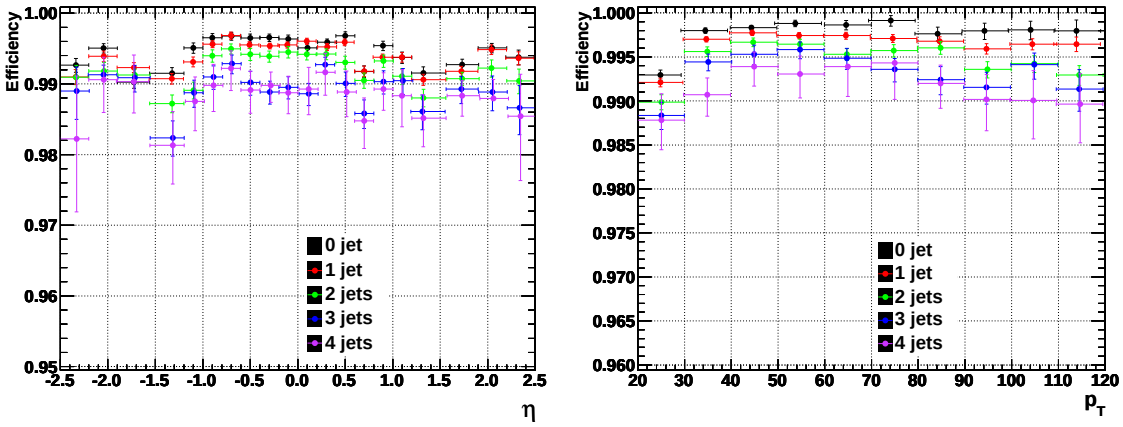

(a) (b)

Figure 5.11. HLT efficiencies for different jet multiplicities as a function of η and p_T of the probes.

The HLT efficiencies are also determined as a function of the distance between the electrons and jets, $\Delta R_{eltojet}$, as shown in Figures 5.12(a) and 5.12(b) as a function of probe η and p_T, respectively. The HLT efficiencies also can be seen for all events as a function of probe η and p_T in Figure 5.13.

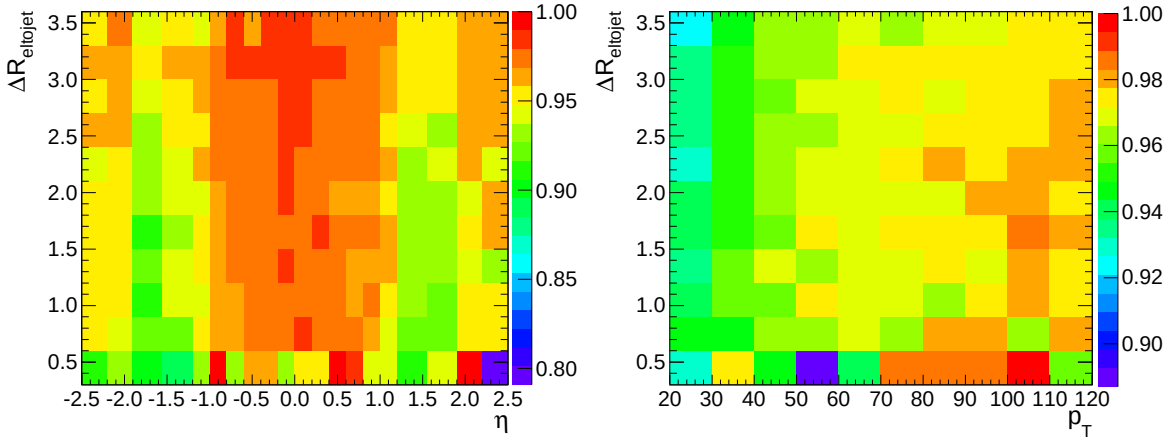

(a) (b)

Figure 5.12. HLT efficiencies as a function of the distance between electrons and jets.

The efficiencies for $Id \rightarrow HLT$ vary between 98.5-99.9% depending on the η location and p_T of the probes. For the same η or p_T bins the differences in HLT efficiencies are less than 1% for different jet multiplicities.

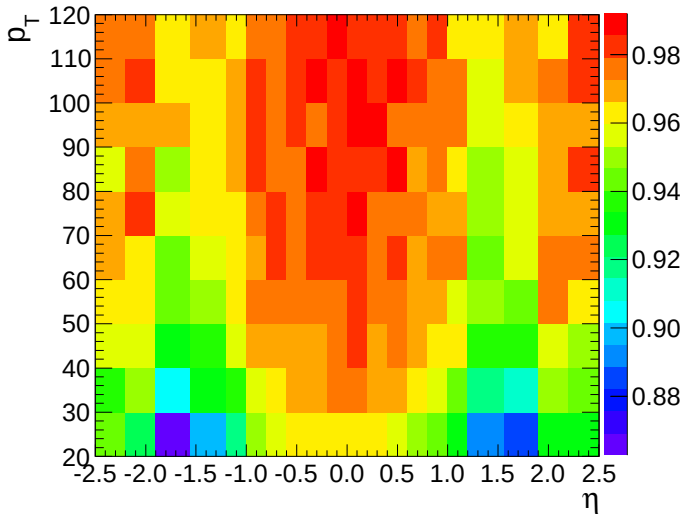

Figure 5.13. HLT efficiency as a function of p_T vs η.

5.6.5. Total Electron Efficiency, $SC \rightarrow HLT$

Total efficiencies as a function of probe p_T and η for 0-, 1-, 2-, 3-, and 4-jet events are shown in Figure 5.14. The difference in efficiencies according to the number of jets in the event can be easily seen. These differences vary according to η and p_T of the electrons.

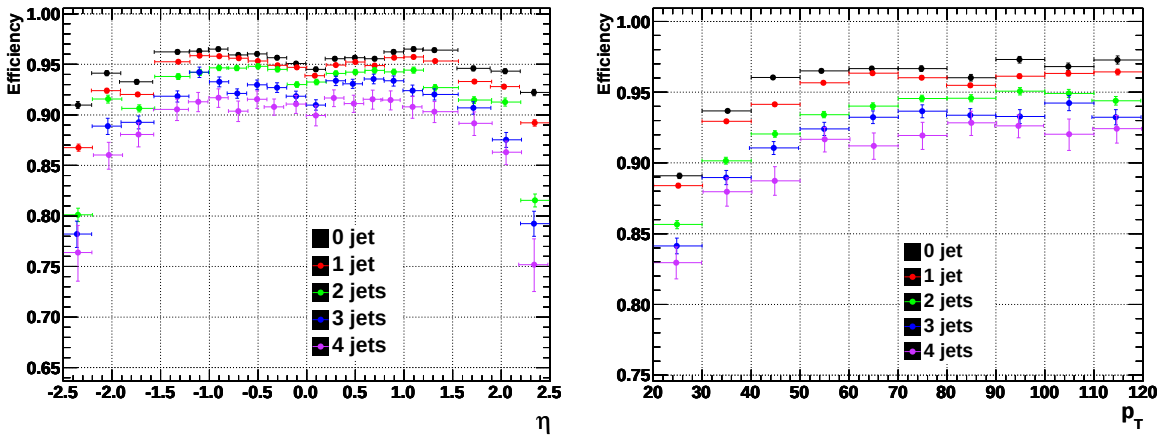

(a) (b)

Figure 5.14. Total efficiencies for different jet multiplicities as a function of η and p_T of the electrons.

Efficiencies for ($SC \rightarrow HLT$) vary between 75-96% depending on the η of electrons. In central region the differences are less than ∼5%. However, the differences

in efficiencies reache up to ∼17% in the forward regions. Therefore the differences in electron efficiencies with respect to different jet multiplicities depend on the η location of the electron.

On the other hand, the differences in electron efficiencies as a function of electron p_T go up to only 7%. The differences in electron efficiencies do not strongly depend on the p_T of the electrons. The efficiencies as a function of electron p_T vary between 83-97% regardless of p_T bin.

Total efficiencies are also determined as a function of the distance between electrons and jets, $\Delta R_{eltojet}$, as shown in Figures 5.15(a) and 5.15(b) as a function of probe η and p_T, respectively. Total efficiencies can be also seen for all events as a function of probe η and p_T in Figure 5.16.

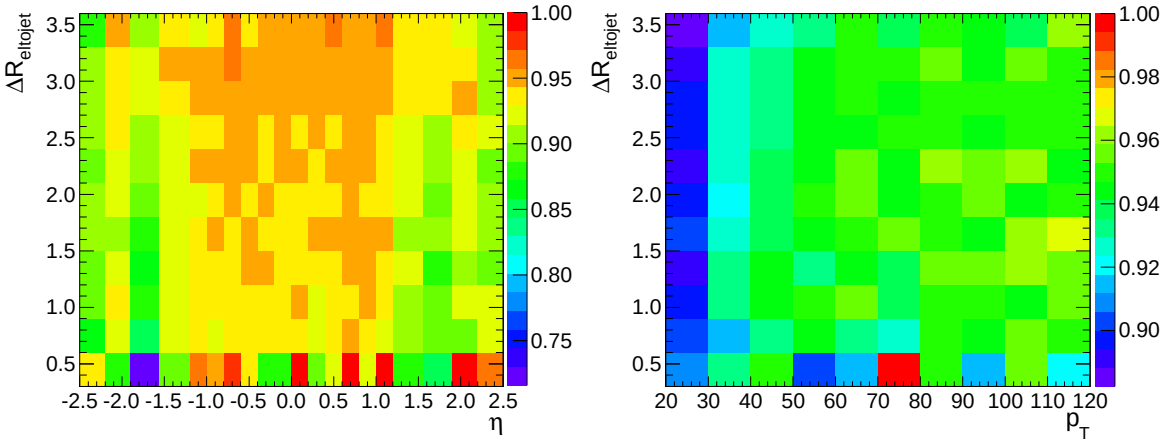

(a) (b)

Figure 5.15. Total efficiencies as a function of the distance between electrons and jets.

Electron efficiencies as a function of $\Delta R_{eltojet}$ vary between 75-99% and 90-97% as a function of electron η and p_T, respectively. Electron efficiencies as a function of η show larger differences between different $\Delta R_{eltojet}$ bins compared to the differences as a function of electron p_T.

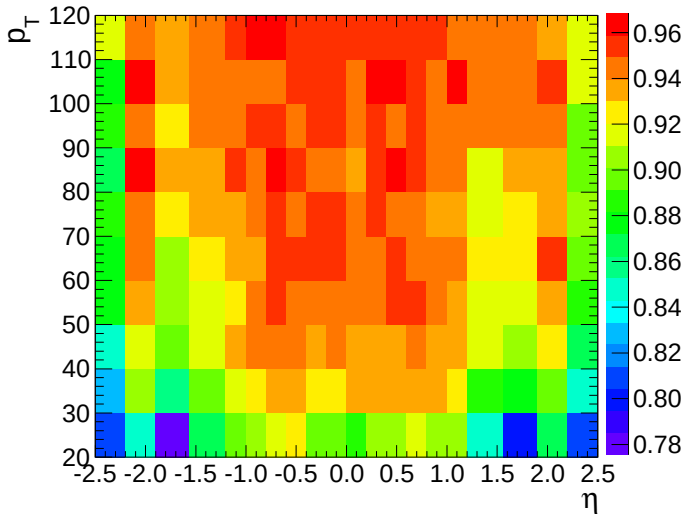

Figure 5.16. Total efficiencies as a function of p_T vs η

Table 5.4. Total electron efficiencies for each probe p_T bins (columns) and jet multiplicity of events (rows).

p_T	0 Jet	1 Jet	2 Jets	3 Jets	4 Jets
$20 < p_T < 30$	0.886	0.877	0.856	0.841	0.829
$30 < p_T < 40$	0.935	0.929	0.902	0.889	0.880
$40 < p_T < 50$	0.960	0.940	0.919	0.911	0.888
$50 < p_T < 60$	0.961	0.958	0.935	0.922	0.916
$60 < p_T < 70$	0.963	0.961	0.938	0.929	0.911
$70 < p_T < 80$	0.962	0.957	0.941	0.933	0.913
$80 < p_T < 90$	0.960	0.955	0.945	0.929	0.922
$90 < p_T < 100$	0.970	0.959	0.951	0.928	0.921
$100 < p_T < 110$	0.961	0.961	0.950	0.935	0.917
$110 < p_T < 120$	0.968	0.962	0.940	0.927	0.920

Table 5.5. Total electron efficiencies for each probe η bins (columns) and jet multiplicity of events (rows).

η	0 Jet	1 Jet	2 Jets	3 Jets	4 Jets
$-2.5 < \eta < -2.2$	0.910	0.868	0.801	0.773	0.764
$-2.2 < \eta < -1.9$	0.941	0.922	0.918	0.889	0.860
$-1.9 < \eta < -1.56$	0.935	0.920	0.908	0.891	0.882
$-1.56 < \eta < -1.2$	0.960	0.952	0.939	0.918	0.906
$-1.2 < \eta < -1.0$	0.961	0.957	0.940	0.939	0.912
$-1.0 < \eta < -0.8$	0.963	0.958	0.946	0.936	0.918
$-0.8 < \eta < -0.6$	0.959	0.957	0.948	0.927	0.904
$-0.6 < \eta < -0.4$	0.960	0.954	0.949	0.925	0.915
$-0.4 < \eta < -0.2$	0.956	0.950	0.947	0.921	0.907
$-0.2 < \eta < 0.0$	0.951	0.949	0.923	0.914	0.910
$0.0 < \eta < 0.2$	0.947	0.941	0.938	0.910	0.901
$0.2 < \eta < 0.4$	0.954	0.949	0.939	0.932	0.915
$0.4 < \eta < 0.6$	0.955	0.951	0.940	0.929	0.915
$0.6 < \eta < 0.8$	0.954	0.948	0.946	0.936	0.919
$0.8 < \eta < 1.0$	0.960	0.958	0.941	0.931	0.918
$1.0 < \eta < 1.2$	0.964	0.960	0.944	0.920	0.909
$1.2 < \eta < 1.56$	0.961	0.955	0.921	0.916	0.903
$1.56 < \eta < 1.9$	0.947	0.936	0.923	0.908	0.886
$1.9 < \eta < 2.2$	0.940	0.930	0.921	0.874	0.861
$2.2 < \eta < 2.5$	0.921	0.885	0.819	0.790	0.751

Table 5.6. Total electron efficiencies for each probe η bins (columns) and probe p_t (rows).

	$20 < p_T < 30$	$30 < p_T < 40$	$40 < p_T 50$	$50 < p_T < 60$	$60 < p_T < 70$	$70 < p_T < 80$	$80 < p_T < 90$	$90 < p_T < 100$	$100 < p_T < 110$	$110 < p_T < 120$
$-2.5 < \eta < -2.2$	0.805	0.825	0.852	0.873	0.873	0.889	0.868	0.888	0.878	0.916
$-2.2 < \eta < -1.9$	0.851	0.906	0.920	0.933	0.944	0.943	0.961	0.942	0.968	0.944
$-1.9 < \eta < -1.56$	0.775	0.856	0.893	0.908	0.904	0.921	0.933	0.924	0.930	0.931
$-1.56 < \eta < -1.2$	0.862	0.895	0.912	0.918	0.928	0.934	0.935	0.942	0.939	0.943
$-1.2 < \eta < -1.0$	0.895	0.911	0.932	0.929	0.933	0.935	0.951	0.944	0.947	0.952
$-1.0 < \eta < -0.8$	0.905	0.928	0.943	0.942	0.937	0.943	0.945	0.955	0.948	0.959
$-0.8 < \eta < -0.6$	0.912	0.935	0.941	0.950	0.958	0.953	0.959	0.956	0.947	0.959
$-0.6 < \eta < -0.4$	0.921	0.937	0.941	0.945	0.953	0.947	0.954	0.948	0.956	0.950
$-0.4 < \eta < -0.2$	0.900	0.929	0.935	0.942	0.954	0.955	0.945	0.951	0.954	0.950
$-0.2 < \eta < 0.0$	0.895	0.929	0.942	0.942	0.952	0.957	0.945	0.951	0.949	0.954
$0.0 < \eta < 0.2$	0.889	0.931	0.938	0.941	0.941	0.945	0.932	0.941	0.943	0.955
$0.2 < \eta < 0.4$	0.904	0.934	0.936	0.948	0.945	0.949	0.950	0.955	0.963	0.953
$0.4 < \eta < 0.6$	0.902	0.937	0.939	0.954	0.956	0.945	0.964	0.941	0.964	0.949
$0.6 < \eta < 0.8$	0.911	0.930	0.943	0.950	0.946	0.947	0.952	0.950	0.951	0.954
$0.8 < \eta < 1.0$	0.901	0.930	0.935	0.945	0.941	0.934	0.948	0.945	0.949	0.958
$1.0 < \eta < 1.2$	0.903	0.928	0.932	0.935	0.949	0.931	0.949	0.939	0.959	0.940
$1.2 < \eta < 1.56$	0.851	0.890	0.912	0.912	0.929	0.918	0.918	0.947	0.941	0.939
$1.56 < \eta < 1.9$	0.799	0.878	0.902	0.915	0.923	0.928	0.931	0.945	0.947	0.940
$1.9 < \eta < 2.2$	0.867	0.899	0.928	0.938	0.951	0.936	0.934	0.947	0.952	0.938
$2.2 < \eta < 2.5$	0.811	0.846	0.869	0.882	0.894	0.909	0.901	0.895	0.914	0.918

5.7. Conclusions and Observations

We measured the electron efficiencies as a function of jet multiplicity. It is shown that the electron efficiencies decrease as the number of jets in the event increases. It is also shown that the magnitude of this change in the electron efficiency depends on the η location of the electrons.

For each increase in the number of jets one can see about 1-3% decrease in the efficiency depending on p_T of the electrons. This difference may reach up to 7% if one measures the efficiency as a function of electron η. The difference is larger in the forward region compared to the more central regions.

The electron efficiency is almost flat in ΔR (the distance between electron and jets) except for $\Delta R < 0.6$. The reason behind this can be explained with the isolation of electron. If an electron is close to a jet with $\Delta R < 0.5$ it will actually be in the cone volume of the jet. Therefore those electrons will have lower efficiency due to the isolation requirements.

6. SUPERSYMMETRY (SUSY)

6.1. Introduction

Supersymmetry (SUSY) [26] is a fermion-boson symmetry that relates the known particles of the Standard Model (SM) to their super partners, sparticles, with change in spin by a half. Therefore every known SM fermion and boson will have a super partner boson and fermion, respectively. The only difference between super partners will be their spin and all the other properties like masses and quantum numbers will be the same.

The SM is a successful theory in many aspects such as unification of the electromagnetic and weak interactions, prediction of vector bosons and top quark. Despite its success it has many drawbacks. The SM does not answer the questions about the existence of the *mass*. It cannot solve the *hierarchy problem* that is also responsible for large contributions to the *Higgs mass*. The *dark matter* which forms most of the universe does not have a candidate in the SM. Three forces of the universe cannot be unified at any energy scale. Furthermore, the Standard Model does not explain why there are three families of quarks and leptons, the reasons for matter-antimatter asymmetry, etc. Physicist are driven to search and study the theories beyond the SM by the temptation of solving these drawbacks.

Supersymmetry is one of the most well-known theories beyond the SM. It brings elegant solutions, by introducing fermion-boson symmetry, to the questions which cannot be answered by the SM. The quantum corrections to the Higgs boson mass coming from SM particles are reduced because of cancellations coming from their super partners. It suggests a good candidate for dark matter via the undetectable and stable, if the R-parity is conserved, lightest supersymmetric particle (LSP).

6.2. Minimal Supersymmetric Standard Model (MSSM)

There is a minimal supersymmetric extension to the SM which makes it possible that SUSY is consistent with the Standard Model in a simplest form. It is so called the Minimal Supersymmetric Standard Model (MSSM) which can include the necessary additional new supersymmetric sparticles [28].

6.2.1. Particle Spectrum (Supermultiplets)

The MSSM is the extension of the SM with minimal number of particles to accommodate the supersymmetry. In the MSSM, each spin-$\frac{1}{2}$ fermion has a spin-0 partner including the different chirality states. In addition there are also gauge fermions, so called gauginos as superpartners of gauge bosons. Also there are two spin-$\frac{1}{2}$ Higgsinos as superpartners of spin-0 Higgs boson. Table 6.1 shows the SM particles and their superpartners in the MSSM.

The MSSM should depend on the *gauge symmetry* as the SM does. In other words, the gauginos should be in gauge supermultiplets as their SM partners gauge bosons. Therefore there will be a single bino ($\tilde{B}$), a single zino ($\tilde{Z}$), three winos ($\tilde{W}^0, \tilde{W}^{\pm}$), and eight gluinos ($\tilde{G}_{1-8}$) as superpartners of photon, W and Z bosons, and gluons, respectively.

Contrary to the SM, which has one Higgs boson, the MSSM introduces two Higgsino supermultiplets $\tilde{H}_u = (\tilde{H}_u^+, \tilde{H}_u^0,)$ and $\tilde{H}_d = (\tilde{H}_d^0, \tilde{H}_d^-,)$. The simplest explanation could be made by the fact that the Higgsino has hypercharge and a single Higgsino would cause chiral anomalies. This anomaly can be prevented by introducing two Higgsinos $\tilde{H}_u$ and $\tilde{H}_d$ with hypercharges +1 and -1, respectively.

The higgsinos and gauginos will couple to each other and form mass eigenstates. The neutral higgsinos ($\tilde{H}_u^0$ and $\tilde{H}_d^0$) and the neutral gauginos ($\tilde{B}$ and $\tilde{W}^0$) could combine and produce *neutralinos*. The neutralinos have four eigenstates represented as $\tilde{\chi}_{1-4}^0$. The charged higgsinos ($\tilde{H}_u^+$ and $\tilde{H}_d^-$) and charged winos ($\tilde{W}^+$ and $\tilde{W}^-$) could couple to

Table 6.1. The particle spectrum in the MSSM and corresponding partners in the SM.

The MSSM sparticles	The SM particles
Higgsinos (spin-$\frac{1}{2}$) $\begin{pmatrix}\tilde{H}_u\\ \tilde{H}_d\end{pmatrix}$	Higgs bosons (spin-0) H
Gauginos (spin-$\frac{1}{2}$) $\tilde{g}$, $\tilde{\gamma}$, $\tilde{Z}$, $\tilde{W}^{\pm}$	Gauge bosons (spin-1) g, γ, Z, $W^{\pm}$
Squarks (spin-0) $\begin{pmatrix}\tilde{u}\\ \tilde{d}\end{pmatrix}_{L,R}$ $\begin{pmatrix}\tilde{c}\\ \tilde{s}\end{pmatrix}_{L,R}$ $\begin{pmatrix}\tilde{t}\\ \tilde{b}\end{pmatrix}_{L,R}$	Quarks, (spin-$\frac{1}{2}$) $\begin{pmatrix}u\\ d\end{pmatrix}_{L,R}$ $\begin{pmatrix}c\\ s\end{pmatrix}_{L,R}$ $\begin{pmatrix}t\\ b\end{pmatrix}_{L,R}$
Sleptons (spin-0) $\begin{pmatrix}\tilde{e}\\ \tilde{\nu}_e\end{pmatrix}_{L,R}$ $\begin{pmatrix}\tilde{\mu}\\ \tilde{\nu}_\mu\end{pmatrix}_{L,R}$ $\begin{pmatrix}\tilde{\tau}\\ \tilde{\nu}_\tau\end{pmatrix}_{L,R}$	Leptons (spin-$\frac{1}{2}$) $\begin{pmatrix}e\\ \nu_e\end{pmatrix}_{L,R}$ $\begin{pmatrix}\mu\\ \nu_\mu\end{pmatrix}_{L,R}$ $\begin{pmatrix}\tau\\ \nu_\tau\end{pmatrix}_{L,R}$

each other and form the *charginos*. The charginos have two eigenstates for each charge $\tilde{\chi}^{+}_{1,2}$ and $\tilde{\chi}^{-}_{1,2}$, hence four charginos in total, the same as the neutralinos.

The first and second-family of the squarks and sleptons are not to be expected to have different mass eigenstates since the mixing angles are small. However the third-family squarks ($\tilde{t}_{L,R}$ and $\tilde{b}_{L,R}$) and sleptons ($\tilde{\tau}_{L,R}$) have two different mass eigenstates for each. Table 6.2 shows the sparticles and their gauge and mass eigenstates according to the MSSM.

Table 6.2. The sparticles and their corresponding eigenstates in the MSSM.

Sparticles	Gauge Eigenstates	Mass Eigenstates
Higgsinos	$\tilde{H}_u^0$, $\tilde{H}_d^0$, $\tilde{H}_u^+$, $\tilde{H}_d^-$	h^0, H^0, A^0, $H^\pm$
Squarks	$\tilde{u}_L$, $\tilde{u}_R$	$\tilde{u}_L$, $\tilde{u}_R$
	$\tilde{d}_L$, $\tilde{d}_R$	$\tilde{d}_L$, $\tilde{d}_R$
	$\tilde{c}_L$, $\tilde{c}_R$	$\tilde{c}_L$, $\tilde{c}_R$
	$\tilde{s}_L$, $\tilde{s}_R$	$\tilde{s}_L$, $\tilde{s}_R$
	$\tilde{t}_L$, $\tilde{t}_R$	$\tilde{t}_{L1}$, $\tilde{t}_{L2}$
		$\tilde{t}_{R1}$, $\tilde{t}_{R2}$
	$\tilde{b}_L$, $\tilde{b}_R$	$\tilde{b}_{L1}$, $\tilde{b}_{L2}$
		$\tilde{b}_{R1}$, $\tilde{b}_{R2}$
Sleptons	$\tilde{e}_L$, $\tilde{e}_R$	$\tilde{e}_L$, $\tilde{e}_R$
	$\tilde{\nu}_{eL}$, $\tilde{\nu}_{eR}$	$\tilde{\nu}_{eL}$, $\tilde{\nu}_{eR}$
	$\tilde{\mu}_L$, $\tilde{\mu}_R$	$\tilde{\mu}_L$, $\tilde{\mu}_R$
	$\tilde{\nu}_{\mu L}$, $\tilde{\nu}_{\mu R}$	$\tilde{\nu}_{\mu L}$, $\tilde{\nu}_{\mu R}$
	$\tilde{\tau}_L$, $\tilde{\tau}_R$	$\tilde{\tau}_{L1}$, $\tilde{\tau}_{L2}$
		$\tilde{\tau}_{R1}$, $\tilde{\tau}_{R2}$
	$\tilde{\nu}_{\tau L}$, $\tilde{\nu}_{\tau R}$	$\tilde{\nu}_{\tau L}$, $\tilde{\nu}_{\tau R}$
Neutralinos	$\tilde{B}^0$, $\tilde{W}^0$, $\tilde{H}_u^0$, $\tilde{H}_d^0$	$\tilde{\chi}_1^0$, $\tilde{\chi}_2^0$, $\tilde{\chi}_3^0$, $\tilde{\chi}_4^0$
Charginos	$\tilde{W}^\pm$, $\tilde{H}_u^+$, $\tilde{H}_d^-$	$\tilde{\chi}_1^\pm$, $\tilde{\chi}_2^\pm$
Gluinos	$\tilde{g}$	$\tilde{g}$

6.2.2. Superpotential

In addition to the supermultiplets, superpotential is also need to define the interactions. The most general superpotential for the MSSM can be written as:

$$W_{MSSM} = \bar{u}Y_u Q H_u - \bar{d}Y_d Q H_d - \bar{e}Y_e L H_d + \mu H_u H_d. \tag{6.1}$$

In above equation all the gauge and family indices are suppressed along with tildes for simplicity. The terms Y_u, Y_d, and Y_e are the 3×3 Yukawa coupling matrices. The

terms Q and L represent the superfields corresponding to left-handed squarks-quarks and sleptons-leptons supermultiplets, respectively. The terms $\bar{u}$ and $\bar{d}$ represent the superfields corresponding to right-handed squarks-quarks supermultiplets, while $\bar{e}$ represents the superfields corresponding to right-handed sleptons-leptons supermultiplets. Finally μ is the supersymmetric Higgs mass term similar to the one in the SM. The MSSM superpotential implies new type of interactions that are squark-Higgsino-quark and slepton-Higgsino-lepton couplings in addition to Higgs-quark-quark and Higgs-lepton-lepton couplings in the SM. These new couplings interactions are caused by the Yukawa matrices since they must remain unchanged under interchanging of families.

6.2.3. R-parity

A new symmetry which is introduced by the MSSM is the *matter-parity* or so called R-parity. This new symmetry is needed to reject the possible terms in the superpotential in Equation 6.2 that could be gauge-invariant but violate the baryon (B) and lepton (L) number conservations. The R-parity is defined as:

$$R = (-1)^{3(B-L)+2s}, \tag{6.2}$$

where s is the spin of the particle, B and L are the baryon and lepton numbers of the particle, respectively. The SM particles and Higgs bosons have R-parity = +1, while the supersymmetric particles will have R-parity = −1. If the R-parity is conserved, then the particles and the sparticles can not be mixing. In fact this will lead to very important results:

- The supersymmetric particles will be always produced in pairs.
- The supersymmetric particles will decay into a state with an odd number of supersymmetric particles (mostly one).
- The lightest supersymmetric particle (LSP) has to be stable. A neutral and weakly interacting LSP is actually a good dark matter candidate.

6.3. Soft SUSY-breaking

The supersymmetric particles have not been directly observed yet. Therefore the sparticles should be heavier than their SM partners. Furthermore if it exists, the SUSY must be a spontaneously broken symmetry at low energies analogous to the electroweak symmetry breaking in the SM. The term *soft* means that the supersymmetry-breaking will not cause divergences in scalar masses.

6.3.1. Soft Lagrangian Terms

A general Lagrangian for soft supersymmetry-breaking can be written as:

$$\mathcal{L}_{soft} = (m^2)^i_j \phi^{j*} \phi_i + \frac{1}{2} M_\ell \lambda^\ell \lambda^\ell + \frac{1}{6} A^{ijk} \phi_i \phi_j \phi_k + \frac{1}{2} B^{ij} \phi_i \phi_j + C^i \phi_i. \tag{6.3}$$

which is free of quadratic divergences in quantum corrections to scalar masses.

The terms presented above Lagrangian can be listed as;

- Scalar squared-mass terms $(m^2)^i_j$
- Gaugino mass terms M_ℓ
- Trilinear scalar couplings A^{ijk}
- Bilinear scalar couplings B^{ij}
- Linear scalar couplings C^i

Then it is possible to write a Lagrangian which softly breaks supersymmetry:

$$\mathcal{L} = \mathcal{L}_{SUSY} - \mathcal{L}_{soft} \tag{6.4}$$

After showing the general form of soft susy-breaking Lagrangian, one can apply the recipe to the MSSM and obtain the $\mathcal{L}^{MSSM}_{soft}$. This soft susy-breaking lagrangian will introduce additional 105 parameters to the 19 parameters of the standard model.

Therefore the unconstrained MSSM theory will be practically untractable. The number of free parameters are needed to be reduced by applying reasonably justified constraints to make the MSSM a predictive theory. These constrains are that no new CP-violation, no flavor mixing, and soft susy-breaking universality. The constrained MSSM soft susy-breaking then will reduce the number of parameters to 19;

- The vacuum expectation value of the two-Higgs doublet fields, $\tan\beta$.
- The mass parameter of higgsino, μ.
- The pseudoscalar Higgs boson mass, M_A.
- The masses of the bino, wino, and gluino, three parameters.
- The sfermion masses, ten parameters.
- Third generation trilinear couplings, three parameters.

6.3.2. Minimal Super Gravity (MSUGRA)

Event though the number of parameters are reduced to 19, a more constrained theory of susy-breaking is needed to obtain a more predictive theory. Therefore a set of boundary conditions at GUT scale can be applied to the MSSM parameters. The theory, so called minimal super gravity (mSUGRA), proposes that the soft parameters are equal at GUT scale and soft susy-breaking is mediated by gravity in a hidden sector.

The universality of mSUGRA theory will reduce the number of parameters by unifying them accordingly. First unification is for the gaugino masses which are the masses of bino, wino, and gluino. They will be unified and equalized as

$$m_{1/2} \equiv M_1 = M_2 = M_3. \tag{6.5}$$

Then it will be followed by the unification of the gauge couplings

$$\alpha_u \equiv \alpha_1 = \alpha_2 = \alpha_3. \tag{6.6}$$

which these relations are verified by the experimental results from LEP1. The scalar masses are also unified at GUT scale

$$m_0 \equiv M_{\tilde{Q}} = M_{\bar{u}} = M_{\bar{d}} = M_{\tilde{L}} = M_{\bar{e}} = M_{H_u} = M_{H_d}. \tag{6.7}$$

Lastly the third family trilinear couplings will be unified

$$A_0 \equiv A_t = A_b = A_\tau. \tag{6.8}$$

Therefore the mSUGRA model will need only four continuous, m_0, $m_{1/2}$, $\tan\beta$, A_0, and one discrete, $sign(\mu)$, free parameters for the soft susy-breaking mechanism. This result is very important since it makes the theory experimentally tractable.

6.4. Sparticle Production and Decay Channels

The squarks and gluinos are strongly interacting particles and they will be abundantly produced in high energy hadron collisions. However, these sparticles will not be the direct target of SUSY search since they will not be kinematically accessible [28]. Instead the neutralinos and charginos which are produced by the decay of squarks and gluinos will give clear signals for the SUSY discovery. They will even grant opportunity for testing SUSY models.

6.4.1. Sparticle Production at Hadron Colliders

Even though the squarks and gluinos are expected to be produced in hadron colliders, Tevatron and LHC, their production cross sections are much smaller compared to the SM particles. Therefore, very high statistics data with very precise detectors are needed to search for sparticles. The production processes of the gluinos and squarks from proton-antiproton and proton-proton collisions [29], in a simplest sparticle form,

are

$$(Tevatron) \quad p\bar{p} \rightarrow \quad \tilde{q}\tilde{q}, \tilde{q}\bar{\tilde{q}}, \tilde{q}\tilde{g}, \tilde{g}\tilde{g} \tag{6.9}$$

$$(LHC) \quad pp \rightarrow \quad \tilde{q}\tilde{q}, \tilde{q}\bar{\tilde{q}}, \tilde{q}\tilde{g}, \tilde{g}\tilde{g} \tag{6.10}$$

Notice that sparticles have to be produced in pairs if R-parity is conserved. Even though there is no difference between pp and $p\bar{p}$ collisions in terms of sparticle production it is easier to reach high luminosity with pp collisions since antiproton beams are relatively harder to produce.

It would be useful to draw the Feynman diagrams of each lowest order partonic interaction for sparticle productions. The squark-antisquark final states could be produced only from the quark-antiquark and gluon-gluon initial states. The squark-squark final states can only be a product of quark-quark initial states. Since the initial states come from proton-proton collisions, the quark-quark pairs will include only the first generation quark flavors, u and d. Another final state would be the gluino-gluino pair productions from quark-quark or gluon-gluon initial states. The last production type of the sparticles is the squark-gluino production. The squark-gluon final state production requires quark-gluon initial state.

The production of charginos and neutralinos will be focused by researchers due to their more kinematically available signal production. The charginos and neutralinos will be produced by electroweak interactions as opposed to squarks and gluinos which are produced by strong interaction. Therefore the production charginos and neutralinos can not be included in gluon interaction since gluons interacts only strongly. However, charginos and neutralinos can be produced directly and also indirectly so that even gluinos and squarks produced by strong interaction can decay to charginos or neutralinos.

6.4.2. Sparticle Decays

Decay of squarks and gluinos will depend on the kinematic conditions which means if squarks are heavier than gluinos, then $\tilde{q} \rightarrow q\tilde{g}$ will be dominant. However, if gluinos are heavier than squarks, then $\tilde{g} \rightarrow q\tilde{q}$ will be dominant. Squarks can also decay into neutralinos $\tilde{q} \rightarrow q\tilde{\chi_i^0}$ and charginos $\tilde{q} \rightarrow q\tilde{\chi_i^\pm}$.

Neutralinos or charginos can decay to sleptons, squarks, electroweak gauge boson, lighter chargino or neutralino, and even Higgs scalar if they are sufficiently lighter. The possible two-body decay modes:

$$\tilde{\chi}_i^\pm \longrightarrow W\tilde{\chi}_j^0, \quad Z\tilde{\chi}_1^\pm, \quad \ell\tilde{\chi}_1^0, \quad \nu\tilde{\ell}, \quad h^0\tilde{\chi}_1^\pm \tag{6.11}$$

$$\tilde{\chi}_i^0 \longrightarrow Z\tilde{\chi}_j^0, \quad W\tilde{\chi}_j^\pm, \quad \ell\tilde{\ell}, \quad \tilde{\chi}_1^0\tilde{\chi}_1^0, \quad h^0\tilde{\chi}_j^0 \tag{6.12}$$

The three body decay modes of charginos and neutralinos:

$$\tilde{\chi}_i^\pm \longrightarrow f\prime f\tilde{\chi}_j^0, \quad ff\tilde{\chi}_1^\pm \tag{6.13}$$

$$\tilde{\chi}_i^0 \longrightarrow ff\tilde{\chi}_j^0, \quad f\prime f\tilde{\chi}_j^\pm \tag{6.14}$$

Three-body decays are more important because they will produce leptons in the final states. Therefore they will give promising clear signal since leptons are relatively easier to detect. Some decay modes with leptons in the final states can be given as:

$$\tilde{\chi}_1^\pm \longrightarrow \ell^\pm\nu\tilde{\chi}_1^0 \tag{6.15}$$

$$\tilde{\chi}_2^0 \longrightarrow \ell^+\ell^-\tilde{\chi}_1^0 \tag{6.16}$$

In addition charginos and neutralinos can directly decay to jets via:

$$\tilde{\chi}_1^{\pm} \longrightarrow jj\tilde{\chi}_1^0 \tag{6.17}$$

$$\tilde{\chi}_2^0 \longrightarrow jj\tilde{\chi}_1^0 \tag{6.18}$$

which also give clear signals for discovery but not as clear as isolated lepton channels.

6.5. SUSY Search Strategies in CMS

The CMS collaboration focused on the mSUGRA model to develop strategies, because of its predictive power, for SUSY discovery at the LHC operation conditions [30]. As explained in Section 6.3.2 mSUGRA model of supersymmetry has only five free parameters at Grand Unification scale. These parameters have been used to define different test points for possible experimental signal prediction and search strategies. All of those test points depend on the chargino and neutralino productions from squarks and gluinos. However, the detectable signals are the products of the expected cascade decays of the charginos and neutralinos.

The main kinematically allowed decays of the charginos and neutralinos are

$$\tilde{\chi}_1^{\pm} \longrightarrow \tilde{\ell}\nu, \quad \tilde{\nu}\ell, \quad W^{\pm}\tilde{\chi}_1^0, \quad H^{\pm}\tilde{\chi}_1^0, \quad \ell^{\pm}\nu\tilde{\chi}_1^0 \tag{6.19}$$

$$\tilde{\chi}_2^0 \longrightarrow \tilde{\ell}\ell, \quad \tilde{\nu}\nu, \quad h^0\tilde{\chi}_1^0, \quad Z^0\tilde{\chi}_1^0, \quad \ell^+\ell^-\tilde{\chi}_1^0 \tag{6.20}$$

where $\tilde{\chi}_1^0$ will produce large missing energy, while $W^{\pm}$, Z^0, and $H^{\pm}$ will produce leptons and/or jets. Therefore detection performance of the missing energy together with leptons and jets is very important for SUSY discovery.

6.5.1. MSUGRA Test Points

According to the four continuous and one discrete parameters of the mSUGRA

$$m_0, \quad m_{1/2}, \quad \tan\beta, \quad A_0, \quad sign(\mu) \tag{6.21}$$

14 test points have been defined to cover significantly different experimental signatures that will be used for the analyses. First ten of these test points are called low mass (LM) test points and aimed at the signals in the early period of LHC operation which is above the Tevatron reach. The last four are called high mass (HM) test points and they cover the signals for the ultimate reach of the LHC operation. Table 6.3 shows all the LM and HM test points with their parameters. The position of the mSUGRA test points in the m_0 and $m_{1/2}$ plane are shown in Figure 6.1.

Table 6.3. The mSUGRA test points with corresponding parameters. Masses are in units of GeV.

Test point	m_0	$m_{1/2}$	$\tan\beta$	A_0	$sign(\mu)$
LM1	60	250	10	0	+
LM2	185	350	35	0	+
LM3	330	240	20	0	+
LM4	210	285	10	0	+
LM5	230	360	10	0	+
LM6	85	400	10	0	+
LM7	3000	230	10	0	+
LM8	500	300	10	-300	+
LM9	1450	175	50	0	+
LM10	3000	500	10	0	+
HM1	180	850	10	0	+
HM2	350	800	35	0	+
HM3	700	800	10	0	+
HM4	1350	600	10	0	+

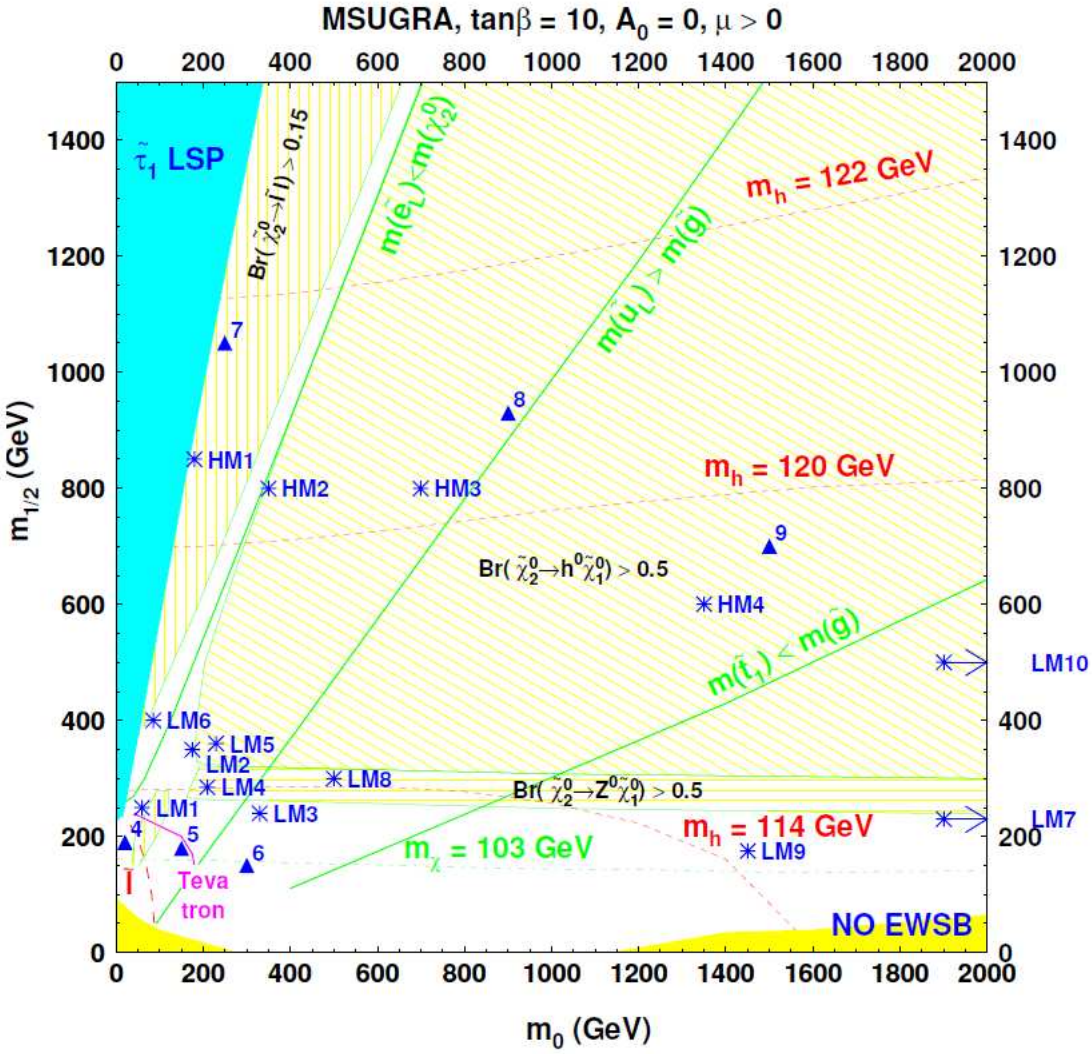

Figure 6.1. The position of the mSUGRA test points in the m_0 and $m_{1/2}$ plane. Note that the other three parameters are $\tan\beta = 10$, $A_0 = 0$, and $\mu > 0$. Figure is taken from [30].

7. SUSY SEARCH WITH Z($\rightarrow e^+e^-$) + JETS + MET IN FINAL STATE

7.1. Introduction

Discovering new physics, such as Supersymmetry [26], is one of the main goals of the CMS at LHC. In our study LM4 test point is chosen due to its promising clean signal. The final state is characterized by Z bosons which are produced from the decay of neutralinos with (97%) branching ratio. The leptonic decay of those Z bosons gives a clean signal in the final state since electrons and muons are relatively easy to detect. The identification of electron-positron pairs from the decay of Z($\rightarrow e^+e^-$) is the starting point of our analysis. In addition a large missing transverse energy, which is a signature of the lightest supersymmetric particle, and jets which come from the fragmentation of quarks and gluons are required [27].

7.2. Signal Topology

Five parameters are needed to define LM4 test point. These are scalar mass, m_0 = 210 GeV, gaugino mass, $m_{1/2}$ = 285 GeV, trilinear coupling, A_0 = 0, vacuum expectation value, tan(β) = 10, and the sign of the Higgsino mixing parameter, $sign(\mu) = +1$. Table 7.1 shows some of the sparticle masses at LM4.

Table 7.1. Sparticle masses (GeV) at LM4.

	$\tilde{u}$	$\tilde{d}$	$\tilde{s}$	$\tilde{c}$	$\tilde{b}$	$\tilde{b}_{1,2}$	$\tilde{t}$	$\tilde{t}_{1,2}$
L	659.41	664.43	664.43	659.41	575.38	600.63	757.38	485.88
R	640.91	640.65	640.65	640.41	605.56	629.89	492.69	653.00
	$\tilde{g}$	$\tilde{\chi}_1^0$	$\tilde{\chi}_2^0$	$\tilde{\chi}_3^0$	$\tilde{\chi}_4^0$	$\tilde{\chi}_1^\pm$	$\tilde{\chi}_2^\pm$	
	695.05	110.29	210.24	384.68	403.73	210.39	402.98	

The inclusive SUSY cross section at LM4 test point calculated by PYTHIA event generator is 6.4 pb for the 10 TeV center-of-mass energy. As one can see from Table 7.1, $m(\tilde{g}) \geq m(\tilde{q})$ which leads to gluinos decaying into squark-quark pairs. The dominant mode for $\tilde{g} \rightarrow \tilde{q}q$ is $\tilde{g} \rightarrow \tilde{b}_1 b$ with 24% branching ratio. Roughly 35% of the events at LM4 include $\tilde{\chi}_2^0$ which comes from $\tilde{b}_1 \rightarrow \tilde{\chi}_2^0 + b$ with 27% branching ratio and there is a direct production of $\tilde{\chi}_2^0$. Besides $\tilde{\chi}_2^0$, 10% of the events include $\tilde{\chi}_2^{\pm}$ which may produce Z boson. About 40% of the LM4 events contain a Z boson.

Almost all (99%) of the Z bosons at LM4 come from the decay channels of $\tilde{\chi}_2^{\pm,0}$,

$$B(\tilde{\chi}_2^0 \rightarrow Z^0 + \tilde{\chi}_1^0) \approx 97\%,$$
$$B(\tilde{\chi}_2^{\pm} \rightarrow Z^0 + \tilde{\chi}_1^{\pm}) \approx 25\%.$$

in SM, it is known that the electron decay channel of Z is $B(Z \rightarrow e^+ + e^-) \approx 3.3\%$. Hence 1.5% of the events at LM4 have $Z(\rightarrow e^+ + e^-)$ in their final states.

The lightest supersymmetric particle, $\tilde{\chi}_1^0$, is undetectable in our detector and causes missing energy (MET) in such SUSY events. High p_T jets are also expected due to quarks and gluons. The two important decays producing electron pairs and MET are shown below,

$$\begin{aligned} \tilde{\chi}_2^0 &\longrightarrow \quad Z^0(\mapsto e^+ + e^-) \quad + \tilde{\chi}_1^0(\mapsto MET) \\ \tilde{\chi}_2^{\pm} &\longrightarrow \quad Z^0(\mapsto e^+ + e^-) \quad + \tilde{\chi}_1^{\pm}(\mapsto W^{\pm} + \tilde{\chi}_1^0(\mapsto MET)). \end{aligned}$$

Therefore, our signal is characterized by e^+e^- pairs coming from the Z decay, large MET due to the LSP, and high P_T jets.

The major background for the analysis comes from the Standard Model. The

events with production of Z and W bosons which may decay into electron channel, includes jets and MET. Those events are namely ZZ, WZ, WW productions and also Z($\rightarrow e^+e^-$) plus jet events for the SM. The last but not the least SM background is the top quark production ($t\bar{t}$). Top quark can decay into electron channel via the decay of W boson and produce electron pairs and also a large MET and jets. QCD background is not included in this analysis.

In addition to the SM background, di-leptons are also produced in other SUSY decays. Some of SUSY events at LM4 may have electron pairs which are produced via the decay $W^{\pm}(\rightarrow e^{\pm} + \nu_e)$. Those events also have the LSP hence large MET such as,

$$\tilde{\chi}_1^{\pm} \longrightarrow W^{\pm}(\mapsto e^{\pm} + \nu_e) + \tilde{\chi}_1^0(\mapsto MET).$$

In our analysis such events are considered as part of the signal events, even though these $e^{\pm}$ pairs do not originate from the Z boson.

7.3. MC Samples

The MC samples Z($\rightarrow e^+e^- + Jets$), ZZ, WZ, WW and $t\bar{t}$ used as background samples for the analysis. For the signal inclusive SUSY LM4 sample is used. All samples are generated with the CMS release "CMSSW_3_1_3" along with "MC_31X_V3" for $\sqrt{s}$ = 10 TeV. The pattuple files are produced with the 6th version of the official "SUSY_pattuple_cfg.py" with the tag "V00-04-12". Table 7.2 shows the data samples with the number of analyzed events and corresponding cross sections.

7.4. Analysis

The starting point of our analysis is to search for e^+e^- pairs. Then the invariant mass distribution of those selected electrons is calculated and the requirement of Z mass window is applied for the signal and the background samples. After that the number of jets above a certain p_T threshold is used to remove the background as much as possible before MET and MHT requirements.

Table 7.2. Cross sections and number of analyzed events for signal and background samples for $\sqrt{s} = 10$ TeV. The effective luminosities (N/σ) are also shown.

	LM4 inclusive	LM4 with Z$\rightarrow e^+e^-$	$t\bar{t}$	WW	WZ	ZZ	Z($\rightarrow e^+e^-$)+Jets									
							0-15	15-20	20-30	30-50	50-80	80-120	120-170	170-230	230-300	300-Inf
$\sigma(pb)$	6.4	0.093	242.8	44.4	17.6	7.3	6430	230	211	142	56.8	18.8	5.4	1.5	0.45	0.2
Analyzed events (N)	119k	1.73k	0.5M	2.1M	2.0M	2.0M	210k	200k	150k	150k	100k	100k	100k	100k	100k	100k
Effective Luminosity (fb^{-1})	18	18	2	47	113	274	0.032	0.869	0.711	1.056	1.760	5.319	18	66	222	500

After all the event selection steps, it was seen that $t\bar{t}$ is the dominant background. The estimation for $t\bar{t}$ events with $e\mu$ method is determined to use for data instead of MC [31].

The details of our analysis are explained in the following subsections.

7.4.1. Electron Selection

The standard electron reconstruction [9] in CMS starts with Super Clusters (SC) found in Electromagnetic Calorimeter (ECAL). Combining the SC with a matching Gaussian Sum Filter track is the reconstruction of a GSF electron. The next step is the isolation of the GSF electron followed by electron ID.

The strongest electron ID requirements suggested by the EgammaPOG [12] are used to select electrons from Z decay along with $|\eta| > 1.44, 1.56 < |\eta| < 2.5$, and $P_T >$ 20 GeV and relative isolation. These selection requirements are also recommended by RA6 [32].

The electron ID is defined with the following first four quantities and the Relative Isolation. Table 7.3 shows the actual requirements for the electron ID selection.

- The ratio of the energy deposited in the hadronic calorimeter to the energy deposited in the electromagnetic calorimeter, E_{Had}/E_{EM}.
- The shower shape of SC in $i\eta$, $\sigma_{i\eta i\eta} = \sum_i^{5\times5} w_i(i\eta - \bar{i\eta}_{5\times5})^2 / \sum_i^{5\times5} w_i$.
- η difference between SC and the track at vertex, $\Delta\eta_{SCtoTrack}$.
- ϕ difference between SC and the track at vertex, $\Delta\phi_{SCtoTrack}$.
- Relative isolation,
  $RelIso = (\sum E_T(ECAL) + \sum E_T(HCAL) + \sum P_T(tracker))_{\Delta R<0.3}/P_T$.

Figure 7.1 shows the P_T, η distribution for all and the selected (passing all the selection requirements) electrons. Figure 7.2 shows the electron ID distributions via N-1 type histograms. The N-1 type of plots show the distribution before all cuts but the

Table 7.3. Electron ID selection

	barrel	endcap
E_{Had}/E_{EM}	0.0201	0.00253
$\sigma_{i\eta i\eta}$	0.0102	0.0291
$\Delta\eta_{in}$	0.00606	0.0032
$\Delta\phi_{in}$	0.0211	0.022
Rel. Isolation	0.1	0.1

one for plotted quantity is applied (white histogram) and after the cut for the plotted quantity is applied (red histogram). These plots make it easy to see the performance of the individual requirement.

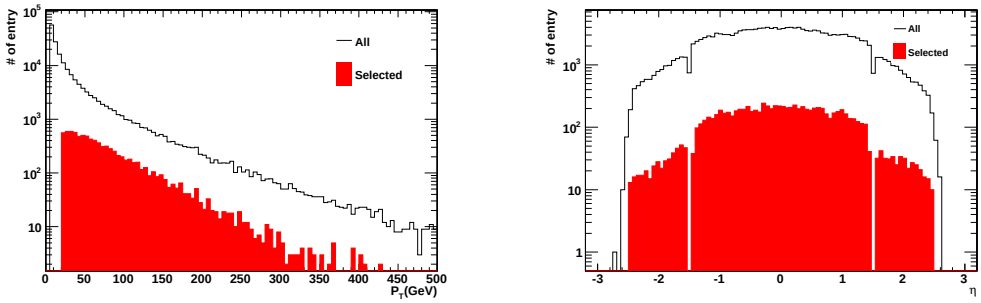

(a) P_T (b) η

Figure 7.1. P_T and η of all(white) and selected(red) electrons for LM4 sample

The $\sigma_{i\eta i\eta}$ distribution in Figure 7.2(e) shows two distinct bumps; which first one corresponds to shower shape in the barrel region while the second one in the endcap region. Note that the first peak is slightly sharper compared to the second one which indicates the barrel region has a higher resolution than the endcap.

To reconstruct invariant mass $M_{e^+e^-}$ given by Equation 7.1, only those electron pairs with opposite charge are used. For the event with more than one e^+e^- pair the $M_{e^+e^-}$ value which is closest to Z boson mass (M_Z) is used (7.3). The $M_{e^+e^-}$ mass range used to select Z candidates is also shown. The performance of the electron selection for the signal and the background is shown in Table 7.4.

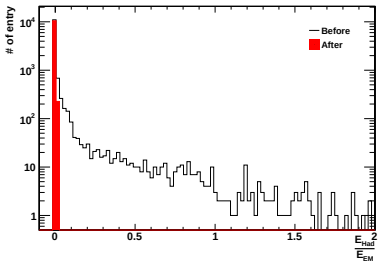

(a) E_{Had}/E_{EM}

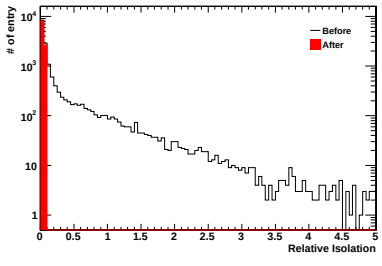

(b) $RelativeIsolation$

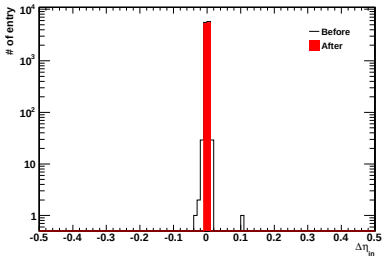

(c) $\Delta\eta_{in}$

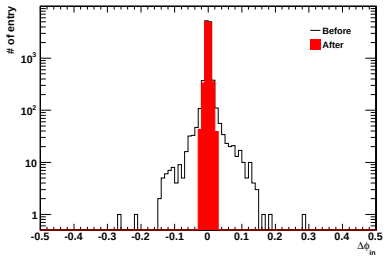

(d) $\Delta\phi_{in}$

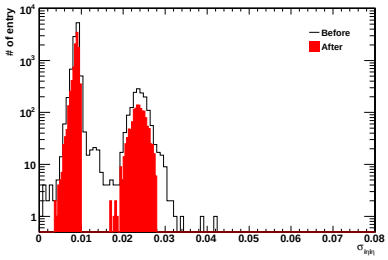

(e) $\sigma_{i\eta i\eta}$

Figure 7.2. Distributions of the electron ID quantities all the requirements except for the plotted quantity (white) and all requirements including the plotted quantity (red).

Invariant mass is determined as

$$\begin{aligned} M^2_{e^+e^-} &= (E_{e^+} + E_{e^-})^2 - |\mathbf{p_{e^+}} + \mathbf{p_{e^-}}|^2 \\ &= m^2_{e^+} + m^2_{e^-} + 2(E_{e^+}E_{e^-} - \mathbf{p_{e^+}}.\mathbf{p_{e^-}}). \end{aligned} \tag{7.1}$$

where E_{e^+}, E_{e^-} are the energy and $\mathbf{p_{e^+}}, \mathbf{p_{e^-}}$ the 3-momentum of the positron and the electron, respectively.

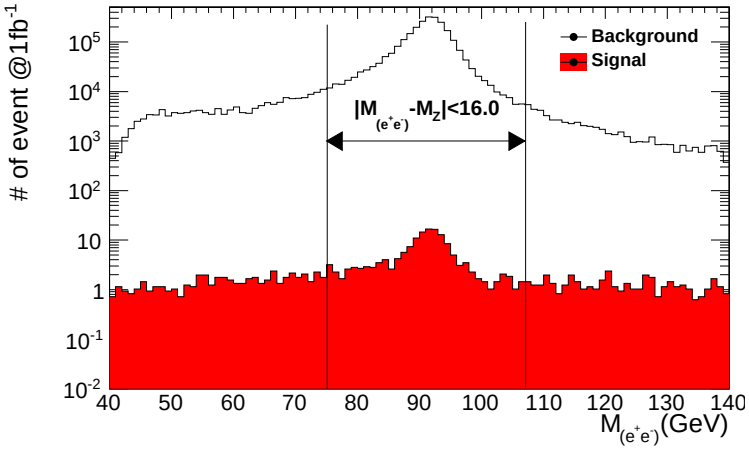

Figure 7.3. Invariant mass distribution for the signal(red) and the background(white)

To see the performance of the Z mass window selection one can look at Figure 7.4 which shows the invariant mass distribution after all the cuts except for the Z mass window selection applied.

Table 7.4. Performance of (e^+, e^-) selection, and $M_{e^+e^-}$ requirements

	LM4	$t\bar{t}$	WW	WZ	ZZ	Z($\rightarrow e^+e^-$)+Jets									
	Z$\rightarrow e^+e^-$					0-15	15-20	20-30	30-50	50-80	80-120	120-170	170-230	230-300	300-Inf
$\sigma(pb)$	0.093	242.8	44.4	17.6	7.3	6430	230	211	142	56.8	18.8	5.4	1.5	0.45	0.2
$1fb^{-1}$	93	242.8k	44.4k	17.6k	7.3k	6430k	230k	211k	142k	56.8k	18.8k	5.4k	1.5k	450	200
(e^+, e^-)	135.3	4076	287	265	209	719k	41k	44k	38k	20k	7670	2647	974	259	121
	146%	2%	1%	2%	3%	11%	18%	21%	27%	36%	41%	49%	63%	58%	61%
$M_{e^+e^-}$	57.4	519.1	32.8	157.9	146.7	425k	14k	30k	28k	11k	4270	2113	792	192	91
	42.4%	12.7%	11.4%	59.6%	70.1%	59.1%	33.9%	68.3%	75.4%	56.2%	55.7%	79.8%	81.4%	74.3%	75.1%

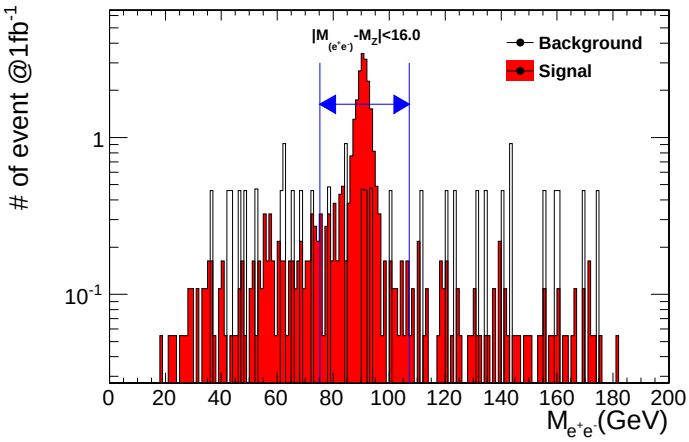

Figure 7.4. Invariant mass distribution for the signal (red) and the background (white) after electron, jet multiplicity, and MET selection criteria applied. Z mass window cut is not applied.

7.4.2. Jet Selection

As explained in Section 3.3, there are two types of jet clustering algorithms [14] used in CMS, *cone type* and *sequential clustering* algorithms. There are three types of *sequential clustering* algorithms named as k_T, Cambridge/Aachen, and Anti-k_T. The Anti-k_T algorithm explained in 3.3.2 is used in this analysis.

The jet finding algorithms use the reconstructed objects as input. Therefore there are three types of jet reconstruction depending on how the particles are reconstructed in CMS. These are Calorimeter Jets, Calorimeter Jet-Plus-Tracks, and Particle Flow. The *Calorimeter* and *Particle Flow* (PF) jets are used and compared in terms of performance in this analysis. Also the jet energy corrections valid for the version used for analysis (CMSSW_3_1_3) are applied to the jets via pattuple production.

Figure 7.5 shows the P_T distribution of the reconstructed jets for the signal and the background samples. Figure 7.6 shows the same distribution for the PF jets. It can be seen that there is no big difference between the calorimeter and the PF jets in terms of the first four jet p_Ts. The blue lines in the plots correspond to $p_T = 50$ GeV. The mean value of the first jet p_T is greater than 50 GeV for both signal and background

samples in Figures 7.5(a) and 7.6(a). But one can see that, in Figures 7.5(d) and 7.6(d), the mean values for the signal and the background events are different.

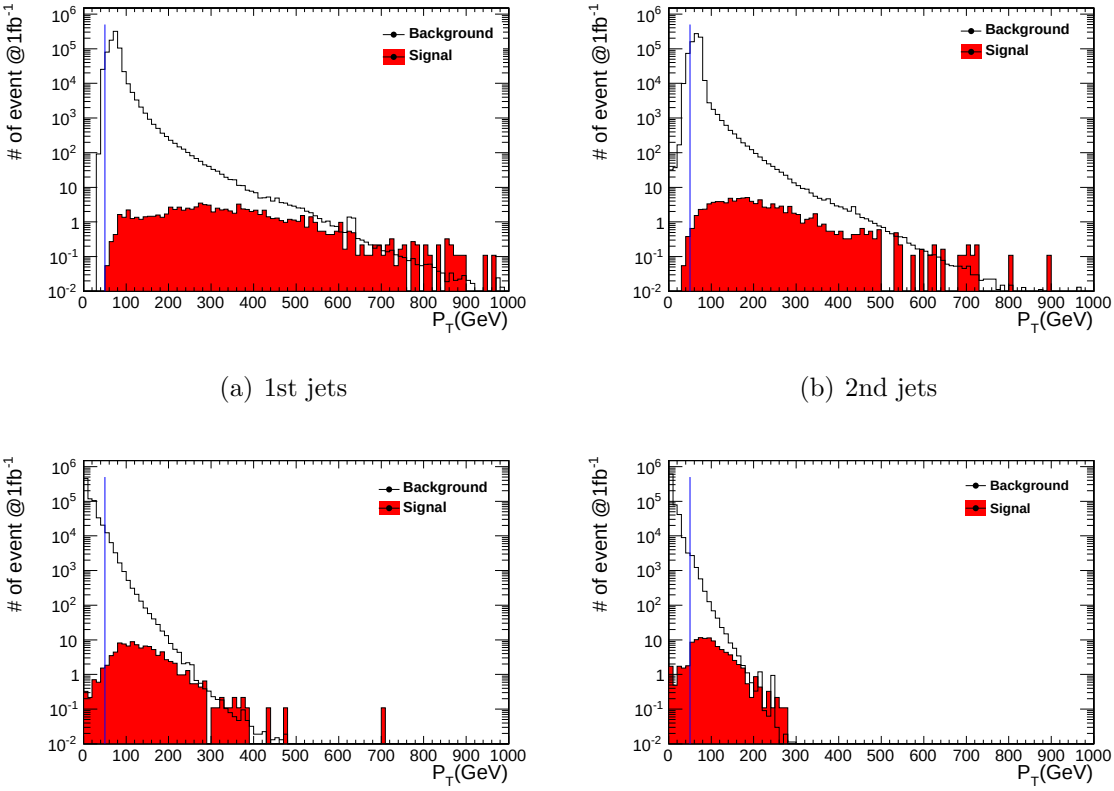

(a) 1st jets

(b) 2nd jets

(c) 3rd jets

(d) 4th jets

Figure 7.5. P_T distribution of the reconstructed calorimeter and generated jets for the signal and the background events after the Z-mass requirement is applied.

This difference shows itself in terms of the jet multiplicity of the events above 50 GeV threshold. Figure 7.7 shows the number of jets above 50 GeV for the signal and the background samples. The jet multiplicity and p_T thresholds are studied to maximize the signal significance. Maximum significance was obtained by requiring at least four jets with $P_T \geq 50$ GeV. Table 7.5 shows the performance of the jet multiplicity requirement. Figure 7.7 shows that a few events containing 13 jets which are quite large. Figure 7.8 shows the jet multiplicity with $P_T \geq 50GeV$ at the generated level. This proves that those are the real jets.

Figure 7.9 shows the jet multiplicity of events that pass the selection cuts except for the number of jets requirement. All the jets are required to have $p_T \geq 50GeV$.

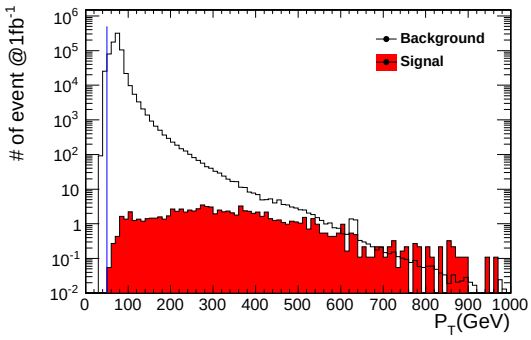

(a) 1st jets

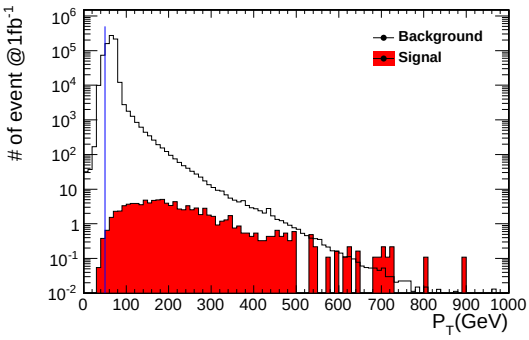

(b) 2nd jets

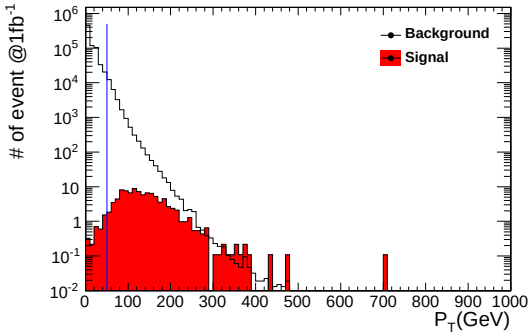

(c) 3rd jets

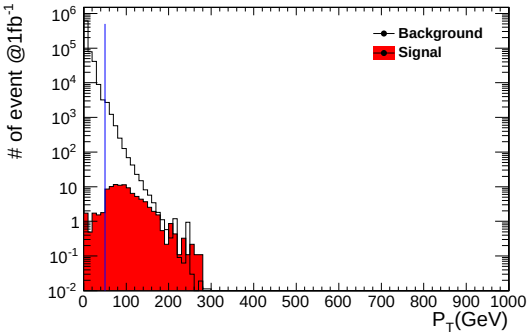

(d) 4th jets

Figure 7.6. P_T distribution of the reconstructed PF and generated jets for the signal and the background events after the Z-mass requirement is applied.

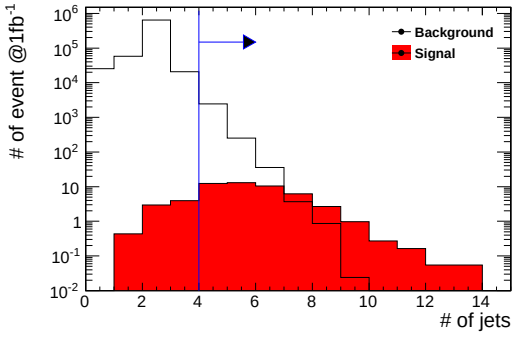

(a) Calorimeter jets

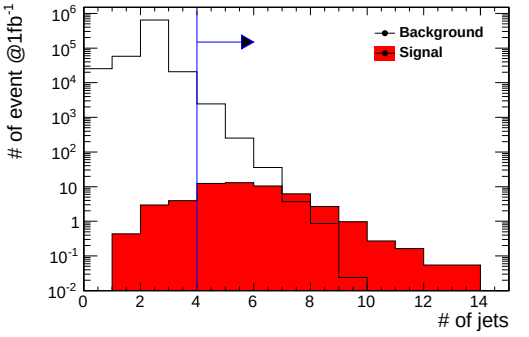

(b) PF jets

Figure 7.7. Number of reconstructed jet distribution with $p_T \geq 50GeV$ for those events after Z-mass requirement is applied.

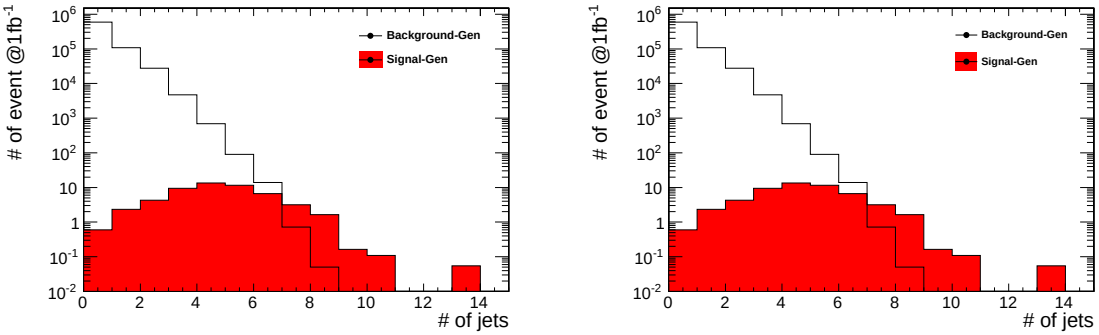

(a) Calorimeter generated jets (b) PF generated jets

Figure 7.8. Number of generated jet distribution with $p_T \geq 50GeV$ for those events after Z-mass requirement is applied.

From this histogram one can see that this cut is quite efficient.

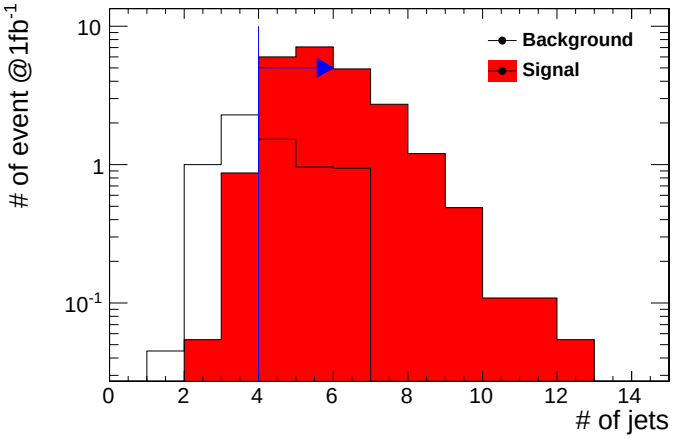

Figure 7.9. Jet multiplicity distribution above $p_T \geq 50$ GeV for these events passing Z-mass and MET requirements. Number of jets cut is not applied.

7.4.3. Missing ET vs Missing HT Selections

Missing transverse energy [16] (MET) is defined ass

$$\begin{aligned}\vec{E}_T^{miss} =& -\sum_n (E_n \sin\theta_n \cos\phi_n \hat{x} + E_n \sin\theta_n \sin\phi_n \hat{y}) \\ =& E_x^{miss}\hat{x} + E_y^{miss}\hat{y} \end{aligned} \tag{7.2}$$

where n corresponds to all towers above a threshold. The $\hat{x}$ and $\hat{y}$ are the unit vectors of the transverse plane perpendicular to the beam direction along $\hat{k}$. In this work corrected MET is used. The jet and muon corrections to MET are applied by PAT production.

The SUSY events have large MET which comes from the undetectable LSP. Neutrinos are also not detectable but they cause a smaller MET. In addition, noisy and fluctuating channels in the calorimeters may create fake MET which may be minimized by corrections.

Both calorimeter and Particle Flow MET collections are used for the analysis. The selections are optimized individually and their performances are compared. Figure 7.10 shows the MET distribution of the signal and the background events and the applied requirements on both PF and Calo type METs.

It is required to have PF MET $\geq$ 230 GeV or CaloMET $\geq$ 200 GeV. The MET requirement removes the SM background significantly. A small amount of $t\bar{t}$ events survives the MET selection. Table 7.5 shows the remaining events passing MET test.

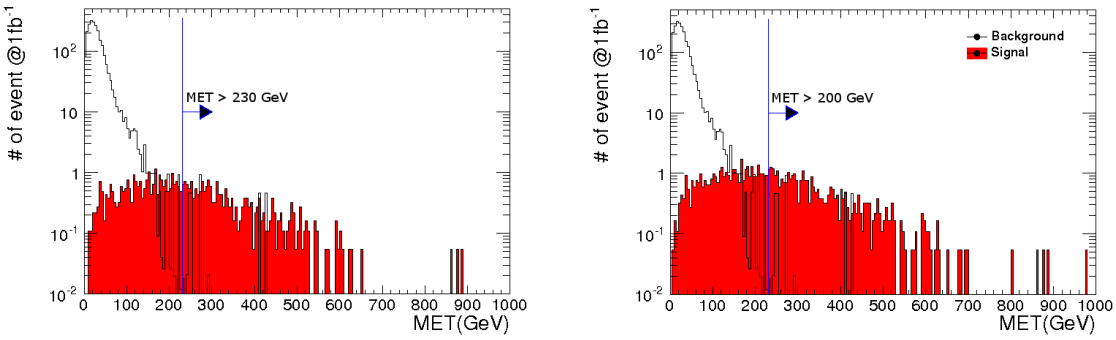

(a) PF MET

(b) Calo MET

Figure 7.10. MET distribution for the signal and the background events after Z mass and jet-multiplicity cuts are applied. Blue lines show the MET cut.

Missing HT which is an alternative way to calculate the missing transverse energy

is defined as

$$MHT = \sqrt{(\sum p_x)^2 + (\sum p_y)^2} \tag{7.3}$$

where p_x and p_y are the x, and y components of the momentum of the jets above a certain P_T threshold. Figure 7.11 shows the MHT calculated using Calo and PF jets for the remaining signal and the background events. The cut on MHT is optimized for the signal significance and the best result is obtained with $MHT > 210$ GeV for PF, or $MHT > 190$ GeV for Calo jets. The results are shown in Table 7.5.

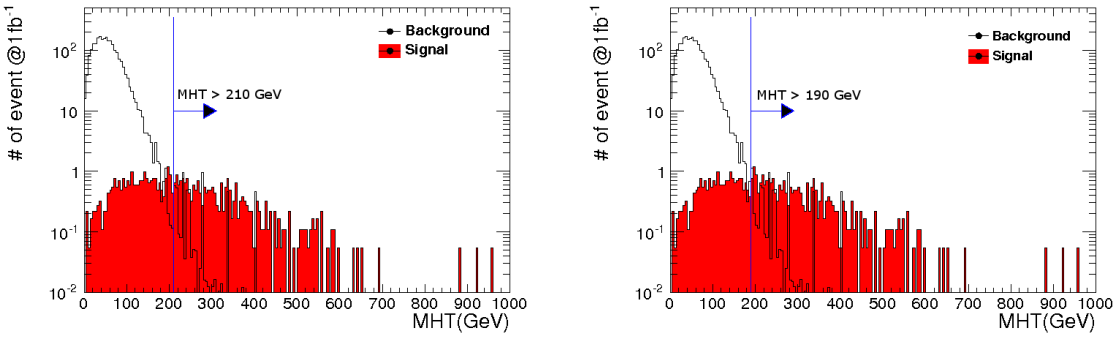

(a) PF MHT

(b) Calo MHT

Figure 7.11. MHT distribution for the signal and the background events after Z mass and jet multiplicity cuts are applied. Blue lines show the MHT cut.

7.4.4. Background Estimation for Top Background with Muons

Top quark pair production ($t\bar{t}$) background events can be estimated by counting the number of events when one of the W bosons coming from $t\bar{t}$ decays into $e\nu$ channel and the other into $\mu\nu$ channel [31]. The branching ratio of $W \to e\nu$ and $W \to \mu\nu$ are almost identical. Hence if the acceptance and the selection efficiency were the same for electrons and muons, the number of $t\bar{t} \to e\mu$ should be twice that of $t\bar{t} \to ee$ events. However, they are not the same and the differences in the selection efficiencies and the acceptance can be estimated from the MC and corrected.

Table 7.5. Number of events for $1fb^{-1}$ before and after each requirement for the signal and the background.

	LM4	$t\bar{t}$	WW	WZ	ZZ	Z($\rightarrow e^+e^-$)+Jets									
						0-15	15-20	20-30	30-50	50-80	80-120	120-170	170-230	230-300	300-Inf
$\sigma(pb)$	6.4 (inclusive) 0.093 (Z$\rightarrow e^+e^-$)	242.8	44.4	17.6	7.3	6430	230	211	142	56.8	18.8	5.4	1.5	0.45	0.2
events at $1fb^{-1}$	6.4k (inclusive) 93 (Z$\rightarrow e^+e^-$)	242.8k	44.4k	17.6k	7.3k	6430k	230k	211k	142k	56.8k	18.8k	5.4k	1.5k	450	200
$M_{e^+e^-}$	57.4	519.1	32.8	157.9	146.7	425k	14k	30k	28k	11k	4270	2113	792	192	91
# of jets															
(PF)	48.6	373.2	2.23	25.9	24.1	334.4	3.7	11.8	126.3	530.3	621.7	286.6	178.1	71.3	35.2
(Calo)	48.6	372.2	2.51	26.1	24.2	365.8	8.2	14.5	125.3	518.4	615.2	394.4	178.5	71.2	35.2
MET															
(PF)	22.4	4.6	0	0	0	0	0	0	0	0	0	0	0	0	0
(Calo)	26.6	8.3	0.1	0.1	0.1	0	0	0	0	0	0	0	0	0	0
MHT															
(PF)	19.9	3.9	0	0.1	0.1	0	0	0	0	0	0	0	0	0	0
(Calo)	27.3	9.2	0.1	0.4	0.2	0	0	0	0	0	0	0	0.2	0.2	0.4

The number of $t\bar{t} \rightarrow ee$ events can be estimated as

$$N^{est}_{t\bar{t}\rightarrow ee} = \left\{ \frac{N_{t\bar{t}\rightarrow ee}}{N_{t\bar{t}\rightarrow e\mu}} \right\}_{mc} . \left\{ N^{obs}_{t\bar{t}\rightarrow e\mu} \right\}_{data}, \tag{7.4}$$

where $N_{t\bar{t}\rightarrow ee}/N_{t\bar{t}\rightarrow e\mu}$ is the ratio of $N_{t\bar{t}\rightarrow ee}$ events to $N_{t\bar{t}\rightarrow e\mu}$ events calculated from the MC and $N^{obs}_{t\bar{t}\rightarrow e\mu}$ is the number of $N_{t\bar{t}\rightarrow e\mu}$ events observed in the data.

The contamination to $e\mu$ events from W+jets events, when one of the leptons are real and the other is fake, are ignored. This background is assumed to be small. Only $t\bar{t}$ events were dominant, hence only $t\bar{t} \rightarrow e\mu$ events were considered.

7.4.5. Electron and Muon Selection

The electron selection is just the same as explained in Section 7.4.1. For muon the selection suggested by RA6 [32] is used. The selection criteria for muons are the following:

- $p_T \geq 20GeV$
- $|\eta| \leq 2.1$
- Muon Type "GlobalMuonPromptTight"
- Relative isolation. $RelIso \leq 0.1$
- $\chi^2/dof \leq 10$
- Number of valid hits inside the tracker ≥ 11
- HCal isolation energy deposition ≤ 6 GeV
- ECal isolation energy deposition ≤ 4 GeV

where the relative isolation is calculated as
$RelIso = (\sum_{\Delta R<0.3} E_T(ECAL) + \sum_{\Delta R<0.3} E_T(HCAL) + \sum_{\Delta R<0.3} P_T(tracker))/P_T$.

After selecting the electrons with the selection rules in 7.4.1 and muons with the selection rules above the invariant mass distribution is calculated using the equation

7.1 for ee, $\mu\mu$, and $e\mu$ pairs. If more than one pair is available the best one that gives the closest invariant mass value to the real Z boson mass is used. The lepton pairs are required to have opposite charges.

7.4.6. Electron and Muon Efficiencies

To understand the differences in the reconstruction efficiency of electron and muons, one can look at the selection at the generated level and compare it to that at the reconstructed level. This helped us see the reconstruction efficiencies of ee, $\mu\mu$, and $e\mu$ pairs in terms of the number of events. The same $t\bar{t}$ sample in the SUSY analysis is used.

Since the generated particles are real, only kinematic, p_T and η requirements are applied at generated level. Again those pairs with invariant mass closest to the actual Z mass are used if more than one are available and are required to have opposite charges. Figure 7.12 shows the comparison of the invariant mass distributions from ee, $\mu\mu$, and $e\mu$ pairs at the generated level to that at the reconstructed level.

From these plots the reconstruction efficiency of electron and muon pairs in terms of number of events are calculated and the results are listed in Table 7.6. The second column gives the number of selected events at the generated level. These numbers represent the actual number of events, hence the denominator for the efficiency calculation while the third column gives numbers for the numerator.

As expected, muons have greater efficiency compared to electrons and the efficiency for $e\mu$ events is in between. Notice that the number of events for $e\mu$ is close to twice that of ee events at the generated level. Ideally, it should be exactly twice, since the number of electrons and muons should be the same and probability of finding an electron and a muon is twice that of finding two electrons or two muons in an event.

Figure 7.13 shows the invariant mass distribution for lepton pairs of different flavors at reconstructed level together. Each histogram has a peak in the central region

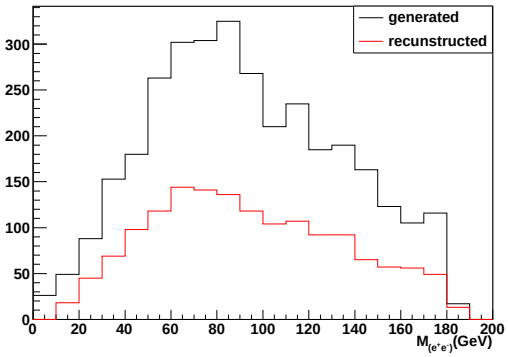

(a) (ee) pairs

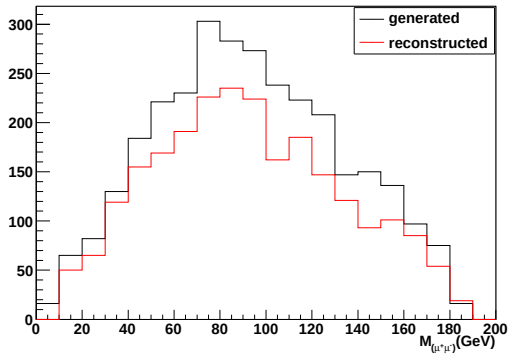

(b) $(\mu\mu)$ pairs

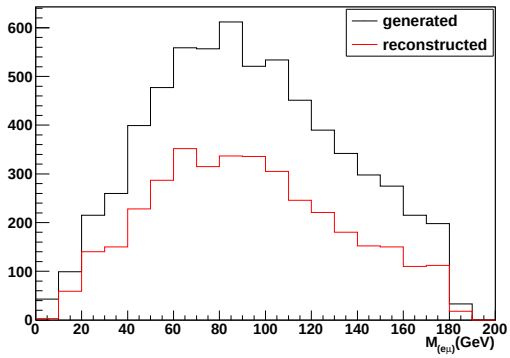

(c) $(e\mu)$ pairs

Figure 7.12. Invariant mass at the generated and the reconstructed level. Horizontal axis shows the number of events.

Table 7.6. The number of events and efficiencies for lepton pair selection. The ee, and $\mu\mu$ numbers are not the same at the generated level due to the different η cuts, $|\eta| < 2.5$ for e while $|\eta| < 2.1$ for μ.

$\ell\ell$	generated	reconstructed	efficiency
$\boldsymbol{ee}$ $\|\eta\| < 2.5$	3302	1522	**46%**
$\boldsymbol{\mu\mu}$ $\|\eta\| < 2.1$	3077	2401	**78%**
$\boldsymbol{e\mu}$	6478	3707	**57%**

due to picking the invariant mass closest to the M_Z. Since this requirement is used for the SUSY selection, that must also be required for the background estimation.

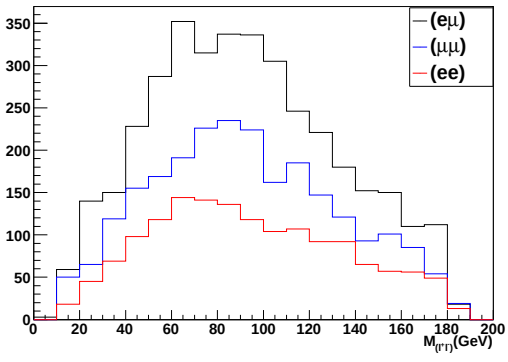

Figure 7.13. Invariant mass distribution at the reconstructed level. Horizontal axis shows the number of events.

7.4.7. The $t\bar{t} \to ee$ to $t\bar{t} \to e\mu$ Ratio

Once the electrons and the muons are selected one can determine the ratio $N_{t\bar{t}\to ee}/N_{t\bar{t}\to e\mu}$ by counting the ee and $e\mu$ events passing our selection cuts. Table 7.7 shows the selection criteria, number of ee and $e\mu$ events passing them and the ratios.

Table 7.7. The number of events passing the cuts with lepton pairs.

cuts	ee	$e\mu$	$N_{ee}/N_{e\mu}$
2 opposite sign lepton	1522	3707	0.41
Z mass window	256	666	0.38
At least four jets	109	204	0.53
MET> 230 GeV	**9**	**21**	**0.43**

Ideally this ratio should be 0.5 if all the differences in acceptance and selection efficiency between muons and electrons are corrected. But the ratio varies as the requirements are applied and the final value from the MC is

$$\frac{N_{t\bar{t}\to ee}}{N_{t\bar{t}\to e\mu}} \cong 0.43.$$

7.5. Results

Table 7.8 shows the total number of remaining events after applying all selection criteria at $1fb^{-1}$. The results are shown for MET and MHT selections with Calorimeter and Particle Flow reconstruction algorithms so that the performance of each method can be seen together.

To calculate the signal significance, the two estimators Z_{Bi} and Z_{PL} [33] are used,

$$Z_{Bi} = \sqrt{2} erf^{-1}(1 - 2P_{Bi}) \tag{7.5}$$

and

$$Z_{PL} = \sqrt{2}\left(n_{on} \ln \frac{n_{on}(1+\tau)}{n_{tot}} + n_{off} \ln \frac{n_{off}(1+\tau)}{n_{tot}\tau} \right)^{1/2} \tag{7.6}$$

where erf^{-1} is the inverse error function and P_{Bi} is the incomplete beta function. Also

n_{off} is the number of background events while n_{on} is the sum of the background and the signal events so that $n_{tot} = n_{on} + n_{off}$. The τ is given by

$$\tau = \frac{\hat{\mu}_b}{\sigma_b^2}$$

where $\hat{\mu}_b$ is the number of background events with uncertainty represented by σ_b.

Table 7.8. Signal significance for $1fb^{-1}$ at $\sqrt{s} = 10$ TeV. The results of two estimators mentioned in the text are listed. The results for the simple significance estimator, $\frac{S}{\sqrt{B}}$, are also added for comparison.

	Selection	Signal	Background	$\frac{S}{\sqrt{B}}$	Z_{Bi}	Z_{PL}
PF Jet+MET	MET	22.4	4.7	10.3	4.9	5.1
	MHT	19.9	4.3	9.6	4.6	4.8
Calo Jet+MET	MET	26.6	8.5	9.1	3.9	4.0
	MHT	27.3	10.7	8.3	3.2	3.3

As one can see from the table the results vary for different selection criteria and the best result is obtained with the PF reconstruction algorithm with MET cut. This is no surprise since it is know that the PF algorithm has better resolution compared to the calorimeter algorithm. And the reason MET cut gives a better result compared to MHT is due to the fact that MHT uses only jets to determine the missing energy while MET uses all the objects, unclustered and clustered towers, eg., leptons, photons, and jets.

Also some plots with very early CMS data at $\sqrt{s} = 7$ TeV for ~ 4 pb^{-1} are produced. These plots were produced with the same selection criteria explained in this chapter including electron and jet selection cuts. The invariant mass distribution of

the electron positron pairs in the data is shown in Figure 7.14. From this distribution it can be seen that most of these electrons and positrons were not produced from the same decay. It is known that the data before cuts have ~ 100 Z bosons decaying into electron channel.

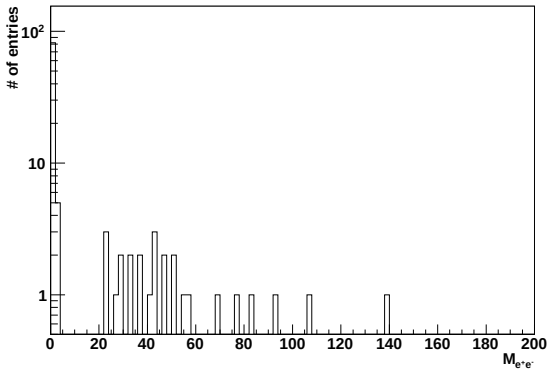

Figure 7.14. Preliminary invariant mass distribution of electron positron pairs with early CMS data at $\sqrt{s} = 7$ TeV for ~ 4 pb^{-1}. Mass unit is in GeV.

The missing transverse energy distribution after electron selection cuts is shown in Figure 7.15. It can be seen that there is no missing energy beyond 35 GeV which means there is no sign of the lightest supersymmetric particle in the data. Therefore no sign of SUSY can be seen with the very early data. Some of the plots obtained with the very early data after individual cuts are shown in APPENDIX A.

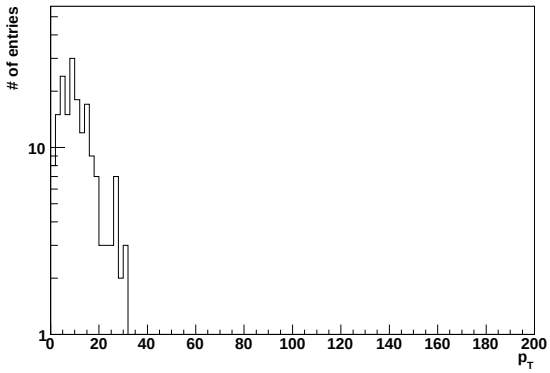

Figure 7.15. Missing transverse energy after electron selection cuts applied. Momentum unit is in GeV.

7.6. Uncertainties

Uncertainties consist of statistical and systematic uncertainties. Statistical uncertainties comes from the limited number of generated MC events used to perform the analysis. However systematic uncertainties arise from the imperfect determination of the properties of the physical objects like electrons, jets, MET which the analysis depends on. Also there is some uncertainty in background prediction arising from the imperfect knowledge of CM production cross sections.

The plots and results in terms of number of events were weighted with

$$w_i = \frac{\sigma_i * \int \mathcal{L}}{N_i^{tot}}$$

where σ_i is the theoretical cross sections, $\int \mathcal{L} = 1 fb^{-1}$ is the integrated luminosity, and N_i corresponds to the number of generated MC events. The index i refers to different MC samples. All these quantities for each sample are listed in Table 7.2. All the plots and the tables are normalized with this weight as

$$N_i^w = w_i N_i^{pass}$$

where N_i^w is the weighted number of events which is used to fill the histograms and tables while N_i^{pass} is the number of MC events that pass the selection criteria. Therefore the statistical uncertainty for N_i^w would be

$$\sigma_{stat} = w_i \sqrt{N_i^{pass}}$$

according to the Poisson statistics.

For the systematic uncertainties two factors, electron identification and jet energy scale (JES) are considered. To determine the systematic uncertainty coming from electron identification, the "electronIDTight" has been changed to "electronIDLoose". Loosening the cuts will increase the selection efficiency of the electrons hence the num-

ber of events passing the complete selection for both the signal and the background. Table 7.9 shows the sensitivity of the analysis to electron ID selection. There is no change in the significance.

Table 7.9. The expected number of events when the electron ID selection is changed. The PF jet + MET cut is used.

	Expected	ElectronIDLoose
Signal	22.4 ± 1.1	24.8 ± 1.2
Background	4.7 ± 1.4	5.7 ± 1.7
Z_{Bi}	4.9	4.9
Z_{PL}	5.1	5.0

Systematic shift of $\pm 10\%$ is applied to the JES to see the variation on the expected number of events. This systematic change affects the two selection requirements. First one is the jet multiplicity above $p_T \geq 50GeV$ and the other one is the MET requirement. Because any change on the JES will affect the correction applied to the raw missing energy by jets. Table 7.10 shows the expected number of events before and after the systematic shift applied to the JES.

Table 7.10. The expected number of events when the systematic shift $\pm 10\%$ applied to JES. The significance for JES+10% is shown only for $\frac{S}{\sqrt{B}}$. The Z_{Bi}, Z_{PL} give null-results due to large increase on the number of background events.

	Expected	$JES - 10\%$	$JES + 10\%$
Signal	22.4 ± 1.1	18.7 ± 1.0	31.2 ± 1.3
Background	4.7 ± 1.4	3.9 ± 1.4	13.2 ± 2.7
Z_{Bi}	4.9	4.9	-
Z_{PL}	5.1	5.0	-
$\frac{S}{\sqrt{B}}$	10.3	9.3	8.5

The +10% systematic shift to JES increases the number of background events by a factor of 3 which is quite big. However this is no surprise because this shift changes MET distribution as shown in Figure 7.16. As one can see from the figures the new MET histogram has many more events passing the $MET \geq 230GeV$ requirement compared to the original MET histogram. The major factor on the final results is the missing transverse energy so that any change on it significantly affects the final results.

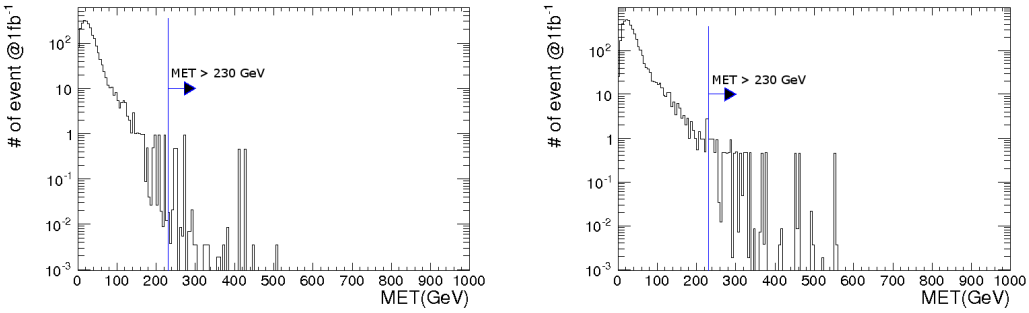

(a) Before (b) After

Figure 7.16. The MET distribution before (a) and after (b) systematic JES shift by 10%

Table 7.11 shows the expected number of the background events before and after JES+10% applied. Before the systematic changes are applied, the number of the background events passing the selection cuts were zero (<0.00X) except for the $t\bar{t}$ sample. After 10% shift is applied on the JES, other background events also pass the selection cuts, especially high p_T Z+Jets samples. Therefore the total number of background events increased to 13 ± 2.7. One should device a method to measure this background directly from data.

These systematic factors also have an effect on the $t\bar{t}$ estimation because the ratio of $N_{t\bar{t}\to ee}/N_{t\bar{t}\to e\mu}$ is directly related to the number of events passing all the selection criteria in signal region for $t\bar{t}$-only sample. Table 7.12 shows the variation on the $N_{t\bar{t}\to ee}/N_{t\bar{t}\to e\mu}$ ratio due to different systematic effects. Note that for the ratio, the muon ID "GlobalMuonPromptTight" is also replaced with "TMLastStationTight" [34].

Table 7.11. The change on the expected number of events after JES is increased by 10%.

	LM4 with Z$\rightarrow e^+e^-$	$t\bar{t}$	WW	WZ	ZZ	Z($\rightarrow e^+e^-$)+Jets									
						0-15	15-20	20-30	30-50	50-80	80-120	120-170	170-230	230-300	300-Inf
Expected	22.4 ± 1.1	4.7± 1.4	0	0	0	0	0	0	0	0	0	0	0	0	0
Expected after JES+10%	31.2 ± 1.3	6.8 ± 1.84	0.1 ± 0.02	0.5 ± 0.07	0.2 ± 0.03	0	0	0	0	0	0.4 ± 0.25	0.9 ± 0.22	1.3 ± 0.14	1.4 ± 0.08	1.6 ± 0.06

Table 7.12. Expected $N_{t\bar{t}\to ee}/N_{t\bar{t}\to e\mu}$ ratio before and after the systematic effects.

	Expected	$JES-10\%$	$JES+10\%$	ElectronIDLoose & TMLastStationTight
$\frac{t\bar{t}\to ee}{t\bar{t}\to e\mu}$	0.43 ± 0.08	0.42 ± 0.06	0.42 ± 0.09	0.48 ± 0.08

7.7. Concluding Remarks

The SUSY search potential with $Z(\to ee)+Jets+MET$ is studied at one of the mSUGRA low mass test points, LM4. Two different types of jet reconstruction algorithms are used with missing transverse energy and missing HT and the results are compared.

The analysis showed that using 1 fb^{-1} data at $\sqrt{s}=10$ TeV one can discover SUSY with Z+jets+MET in final state at LM4 mSUGRA test point with 5.1σ significance using only the statistical uncertainty. The selection criteria can remove all but the $t\bar{t}$ SM background. This background can be estimated by measuring the $e\mu$ rate in the data and scaling it by the ratio $(t\bar{t}\to e\mu)/(t\bar{t}\to ee)$ determined from the MC. The ratio of $(t\bar{t}\to e\mu)/(t\bar{t}\to ee)$ was found to be ~ 0.43 with up to 20% systematic uncertainty.

The systematic uncertainties are studied for lepton identification and jet energy scale factors. The 10% systematic shift on the JES showed a 150% increase for the number of background events passing our selection criteria. This is caused mostly by the large increase in MET.

This study showed that using PF jets with missing transverse energy give better results. Using MHT might be a good alternative to MET since only quantities related to the jets are used. This way the effect of the noise and low p_T jets on the results can be reduced.

Two estimators, Z_{PL} and Z_{Bi}, are used to calculate the signal significance. These two estimators show very similar results, the difference is about 0.1 unit of significance

for the same scenario. Using PF jets with missing transverse energy gave signal significance of 5.1 by the estimator Z_{PL}. Adding the systematic uncertainties could reduce it down to 3.2.

8. CONCLUSIONS

In this thesis, I have performed three different analysis for the CMS detector.

First analysis "HPD charge spectrum" is performed to accumulate the charge spectrum of the HPD detectors of the HB and HE with high statistic and study this spectrum from the *noise* point of view. In this study a method to monitor the HPD charge spectrum is developed which can be used to monitor the HPD noise spectrum especially when high statistic is needed. It is seen that the HPD noise spectrum including the cosmic muon energy deposition can be monitored without dedicated-trigger events to improve the statistic.

The second analysis "Electron efficiency as a function of jet multiplicity" is focused on the relation between the jets and the electron reconstruction efficiency. The analysis shows that each increase in the number of jets decrease the efficiency by about 1-7% depending on p_T and η of the electrons. Also it has been observed that the difference is larger in the forward region compared to the more central regions. The relation between ΔR (between electron and jets) and electron efficiency has been studied also. The results show that except for $\Delta R < 0.6$ the electron efficiency is flat. The reason behind this can be understood in terms of the electron isolation.

The last one "SUSY search with Z($\rightarrow e^+e^-$) + jets + MET in final state" is a physics simulation analysis studying the performance of the dielectron channel with jets and MET for the SUSY discovery in the CMS detector. The analysis shows that SUSY can be discovered with 1 fb^{-1} data at $\sqrt{s} = 10$ TeV. The relevant background can be cleaned with proposed selection criteria except for the $t\bar{t}$ background. An estimation for $t\bar{t}$ background for data is performed with $e\mu$ events.

In SUSY analysis, two different types of comparisons are made. The results showed that *Particle Flow* clustering algorithm for jets and missing transverse energy promises the best performance in ideal detector conditions. On the other hand missing

HT was found to be a good candidate for determining missing energy, especially for the events with large p_T jets are presented.

APPENDIX A: ANALYSIS PLOTS WITH EARLY CMS DATA

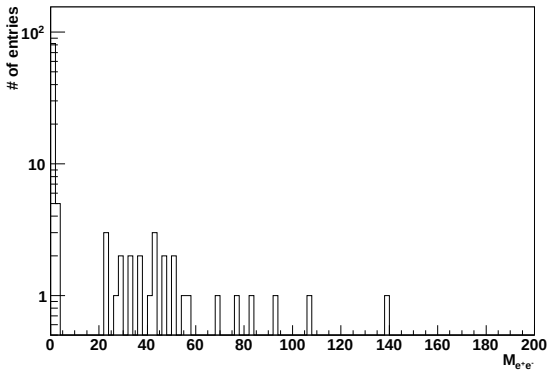

Figure A.1. Invariant mass of electron positron pairs.

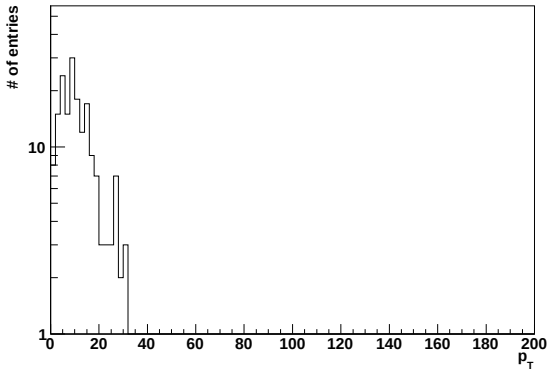

Figure A.2. Missing transverse energy for selected Z events.

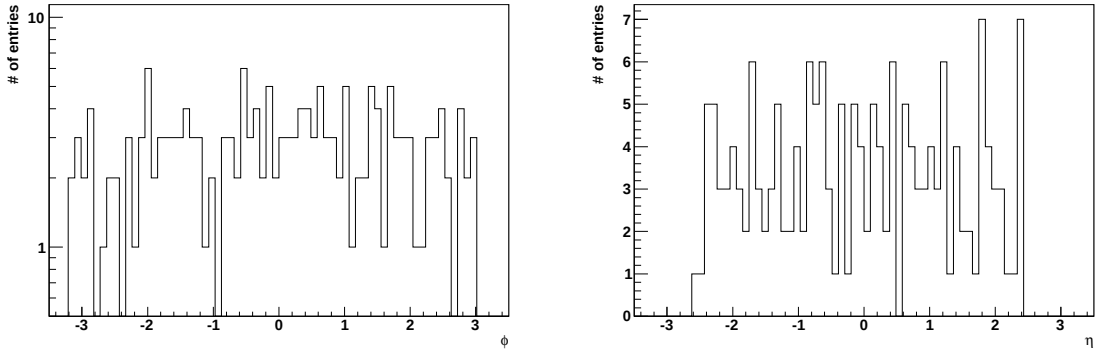

(a) ϕ (b) η

Figure A.3. ϕ and η distribution of Z boson.

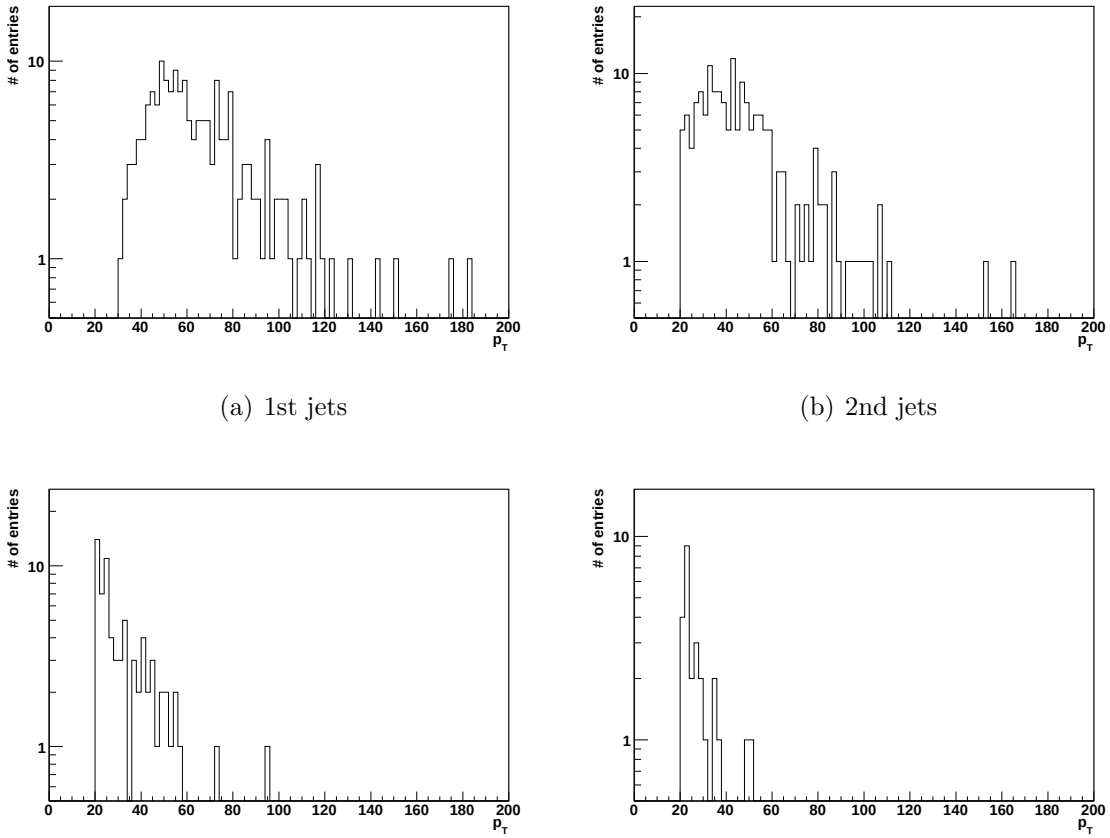

(a) 1st jets (b) 2nd jets

(c) 3rd jets (d) 4th jets

Figure A.4. P_T distribution of the reconstructed PF jets. Momentum untit is in GeV.

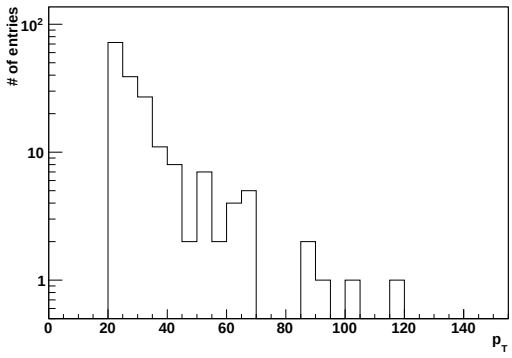

(a) p_T

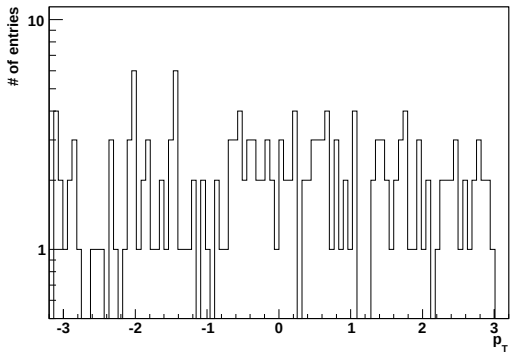

(b) ϕ

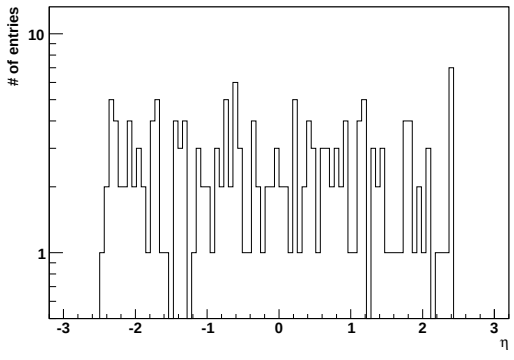

(c) η

Figure A.5. Distributions of electron quantities.

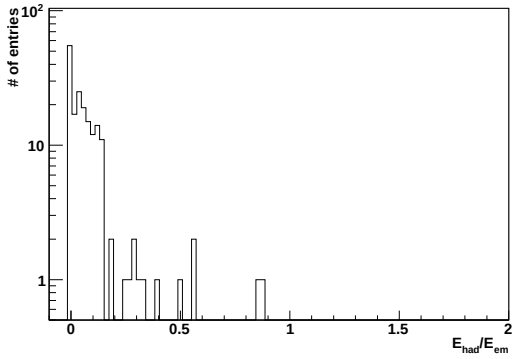

(a) E_{Had}/E_{EM}

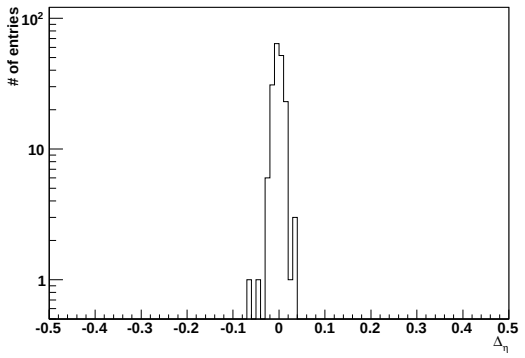

(b) $\Delta\eta_{in}$

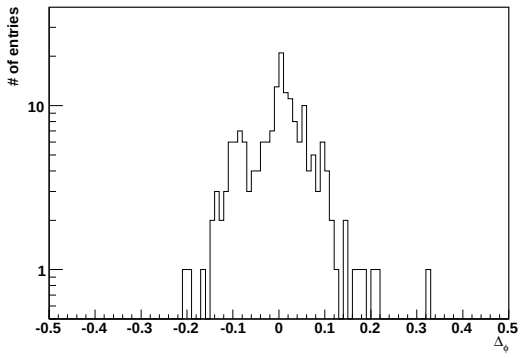

(c) $\Delta\phi_{in}$

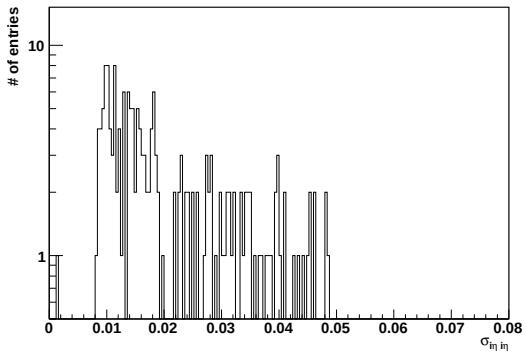

(d) $\sigma_{i\eta i\eta}$

Figure A.6. Distributions of electron ID quantities.

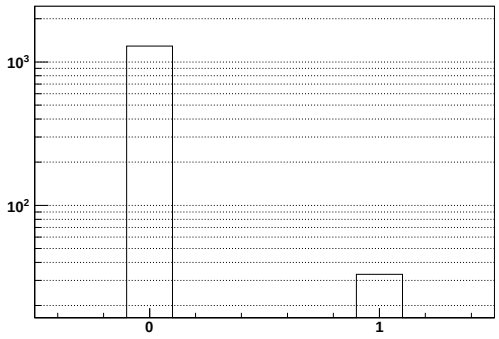

(a) Loose ID

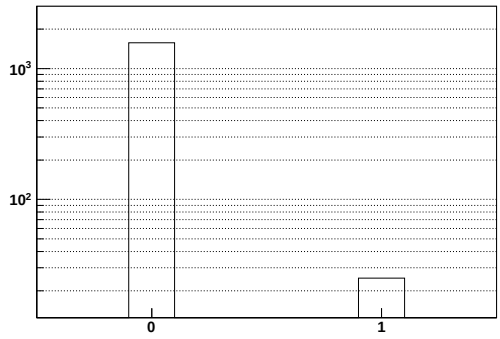

(b) Tight ID

Figure A.7. Electron ID distribution.

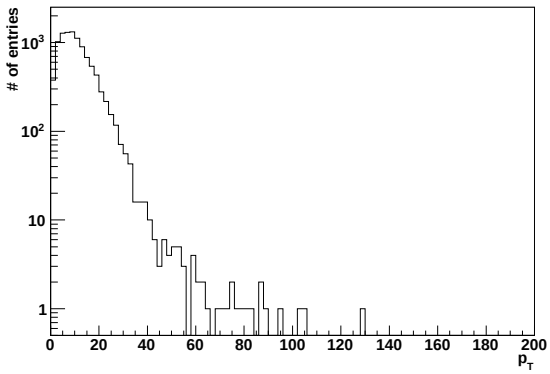

(a) Missing transverse energy

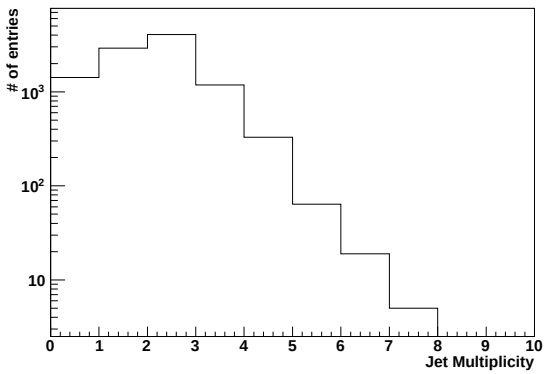

(b) Jet multiplicity

Figure A.8. Missing energy and jet multiplicity before electron selection. Energy unit is in GeV.

REFERENCES

1. CMS collaboration, *"The CMS experiment at the CERN LHC"*, JINST 3 S08004, 2008.

2. CMS collaboration, *"The Compact Muon Solenoid technical proposal"*, CERN-LHCC 94-38, 1995.

3. CMS Collaboration, *"The Tracker Project, Technical Design Report"*, CERN/LHCC 98-6, CMS TDR 5, 1998.

4. CMS Collaboration, *"CMS ECAL Technical Design Report"*, CERN/LHCC 97-033, 1997.

5. CMS Collaboration, *"CMS The hadron calorimeter project: technical design report"*, CERN/LHCC 97-031, 1997.

6. CMS collaboration, *"The CMS muon project, technical design report"*, CERN-LHCC-97-032, 1997.

7. CMS collaboration, *"The CMS muon system"*, Eur. Phys J. C 33, s01, s993-s995, 2004.

8. CMS collaboration, *"The TriDAS project, technical design report. Volume 1: The level-1 trigger"*, CERN-LHCC-2000-038, 2000.

9. Baffioni, S., C. Charlot, et al, *"Electron Reconstruction in CMS"*, CMS NOTE 2006/040, 2006.

10. Meschi, E., T. Monteiro, C. Seez, and P. Vikas, *"Electron Reconstruction in the CMS Electromagnetic Calorimeter"*, CMS NOTE 2001/034, 2001.

11. Speer T., R. Fruhwirth, *"A Gaussian-sum Filter for Vertex Reconstruction"*, CMS

NOTE 2005/005, 2005.

12. Branson, J., M. Gallinaro, et al, *"A cut based method for electron identification in CMS"*, CMS AN-2008/082, 2008.

13. Abbiendi, G., N. Adam, et al, *"Muon Reconstruction in the CMS Detector"*, CMS AN-2008/097, 2008.

14. Chetluru, V., F. Pandolfi, P. Schieferdecker, M. Zielinski, *"Jet Reconstruction Performance at CMS"*, CMS AN-2009/067, 2009.

15. CMS collaboration, *"CMS physics: Technical design report."*, CERN-LHCC-2006-001, 2006.

16. Landsberg, G., F. Moortgat, *"MET Reconstruction, Performance, and Validation"*, CMS AN-2008/-89, 2008.

17. Mehmet, D., E. Gulmez, et al. *"HPD Noise Spectrum in CRAFT08"*, CMS DN 2009/017, 2009.

18. Anzivino, G., A. Heering, et al. *"Review of the Hybrid photo diode tube (HPD) an advanced light detector for physics"*, Nucl. Instr Meth vol. A 365, pp. 76-82, 1995..

19. Cushman, P., and A. Heering, *"CMS HCAL Hybrid Photodiode Design and Quality Assurance Stations"*, SLAC-J-ICFA-025, 2002.

20. Cushman, P., A. Heering, and A. Ronzhin, *"Custom HPD readout for the CMS HCAL"*, Nucl. Instr. Meth. vol. A411, pp. 304-312, 1998.

21. Cushman, P., A. Heering, et al, *"Multi-pixel hybrid photodiode tubes for the CMS hadron calorimeter"*, Nucl. Instr. Meth. vol. A457, pp. 75-100, 1997.

22. CMS HCAL Collaborations, *"Design, performance, and calibration of CMS hadron-barrel calorimeter wedges"*, Eur. Phys. J. C (2008) 57: 653663, 2008.

23. Daskalakis, G.,et al, *"Measuring Electron Efficiencies at CMS with Early Data"* CMS AN 2007/019, 2007.

24. Adam, N., et al, *"Generic Tag and Probe Tool for Measuring Efficiency at CMS with early Data"* CMS AN 2009/111, 2009.

25. *https://twiki.cern.ch/twiki/bin/viewauth/CMS/ElectronTagAndProbe.*

26. S. Martin, *"A Supersymmetry Primer"*, hep-ph/9709356, 2008.

27. Mehmet, D., E. Gulmez, et al. *"SUSY SEARCH WITH Z($\rightarrow e^+e^-$) + JETS + MET IN FINAL STATE"*, CMS AN 2010/217, 2010.

28. Djouadi, A, S. Rosier-Lees, et al, *"The Minimal Supersymmetric Standard Model: Group Summary Report"*, hep-ph/9901246, 1998.

29. Beenakker, W., R. Hopker, M. Spira, and P. M. Zerwas, *"Squark and Gluino Production at Hadron Colliders"*, hep-ph/9610490v1, 1996.

30. CMS collaboration, *"CMS Technical Design Report, Volume II: Physics Performance"*, J. Phys. G: Nucl. Part. Phys. 34, 2007.

31. CMS AN-2008/044, D.Bandurin et al, *"Study of backgrounds to high-mass di-electron(Drell-Yan) final states"*.

32. *https://twiki.cern.ch/twiki/bin/view/CMS/SusyRA6OSEEProjectTable.*

33. physics/0702156v4, R. Cousins, J. Linnemann, J. Tucker *"Evaluation of three methods for calculating statistical significance when incorporating a systematic uncertainty into a test of the background-only hypothesis for a Poisson process"*.

34. CMS AN-2008/098, M. Mulders et al, *"Muon Identification in CMS"*.